Grid Power Quality Improvement and Active Power Injection Methods Through Solar Interface Active Filters in Presence of Nonlinear Loads

A Thesis Submitted

in Partial Fulfilment of the Requirements

for the Degree of

DOCTOR OF PHILOSOPHY

by

MAHESH REDDY PUNDRU

(2018eez0008)

DEPARTMENT OF ELECTRICAL ENGINEERING

INDIAN INSTITUTE OF TECHNOLOGY ROPAR

October, 2024

To My Parents

Declaration of Originality

I hereby declare that the work which is being presented in the thesis entitled **"Grid Power Quality Improvement and Active Power Injection Methods through Solar Interface Active Filters in Presence of Nonlinear Loads"** has been solely authored by me. It presents the result of my own independent investigation/research conducted during the time period from 31^{st} July 2018 to 15^{th} May 2024 under the supervision of **Dr. K. Ramachandra Sekhar, Assistant professor, Indian Institute of Technology Ropar**. To the best of my knowledge, it is an original work, both in terms of research content and narrative, and has not been submitted or accepted elsewhere, in part or in full, for the award of any degree, diploma, fellowship, associateship, or similar title of any university or institution. I also declare that any idea/data/fact/source stated in my thesis has not been fabricated/ falsified/ misrepresented. All the principles of academic honesty and integrity have been followed. I fully understand that if the thesis is found to be unoriginal, fabricated, or plagiarized, the Institute reserves the right to withdraw the thesis from its archive and revoke the associated Degree conferred. The Institute also reserves the right to appraise all concerned sections of society of the matter for their information and necessary action (if any). If accepted, I hereby consent for my thesis to be available online in the Institute's Open Access repository, inter-library loan, and the title & abstract to be made available to outside organizations.

Signature

Name: Mahesh Reddy Pundru
Entry Number: 2018EEZ0008
Program: PhD
Department: Electrical Engineering
Indian Institute of Technology Ropar
Rupnagar, Punjab 140001

Date: 11^{th}October,2024

Acknowledgement

I take this opportunity to acknowledge my heartfelt gratitude to all those people who directly or indirectly helped me to carry out this research work successfully. I am heartily thankful to my supervisor, Dr. K. Ramachandra Sekhar, whose encouragement, guidance, and support throughout my research work enabled me to develop an understanding of the subject. I appreciate his sincere help in terms of contributions of time and ideas to make my Ph.D. experience stimulating and productive. His joy and enthusiasm for his research were contagious and motivational for me, even during tough times in the Ph.D. pursuit. I express my gratitude for his willingness to help and timely advice on issues beyond the scope of doctoral studies.

I would like to acknowledge the financial, academic, and technical support of the Indian Institute of Technology Ropar for this research. I am sincerely grateful to Dr. A. V Raviteja, Dr. Saifulla Payami, and Dr. Asad H. Sahir for assessing the work and giving invaluable suggestions as members of the Doctoral committee.

The members of the Power Group have contributed immensely to my personal and professional time during my stay at the institute. The group has been a source of friendships, good advice, and collaboration. I especially thank Dr. Baibhav Kumar Gupta, Dr. Amol Ishwarrao Gedam, Mr. Aashish Kumar, Mr. Nikhil Kumar, Mr. A. Suryakiran, Mr. Ankan, Mr. Digamber Kumar, Dr. Mahetab Alam, Dr. Samarjeet Singh for their valuable advice during my course of research and personal life. I would like to express gratitude for the services being offered by Mr. Dilbag Singh, Mr.Devendra Kumar, and Mr.Jaspreet Singh, staff of the power electronics and Machine laboratory of the Electrical Engineering department. Last but not least, I would like to thank my family and my parents, who educated me, for always believing in my capabilities and for encouraging me to pursue my dreams. Especially my father, for unconditional support and encouragement, for listening patiently to all my problems and frustrations, and for always being there for me during good and bad times.

Certificate

This is to certify that the thesis entitled **"Grid Power Quality Improvement and Active Power Injection Methods through Solar Interface Active Filters in Presence of Nonlinear Loads"**, submitted by **Mahesh Reddy Pundru (2018EEZ0008)** for the award of the degree of **Doctor of Philosophy** of Indian Institute of Technology Ropar, is a record of bonafide research work carried out under my guidance and supervision. To the best of my knowledge and belief, the work presented in this thesis is original and has not been submitted, either in part or full, for the award of any other degree, diploma, fellowship, associateship or similar title of any university or institution.

In my opinion, the thesis has reached the standard of fulfilling the requirements of the regulations relating to the Degree.

K R ch sekhar

Signature of the Supervisor

Name: Dr. K. Ramachandra Sekhar

Department: Electrical Engineering

Indian Institute of Technology Ropar

Rupnagar, Punjab 140001

Date: 11^{th}October,2024

Abstract

This work proposes an efficient integration method of solar energy with industrial nonlinear loads, accounting for dynamic variations in solar power and load harmonic profiles. The involved dynamics necessitate that the solar interface front-end inverters be equipped to simultaneously handle both harmonic distortions and active power injection characteristics. In this work, an instantaneous load and source characteristic mapping is proposed for the solar-interfaced front-end inverter operated as a shunt active power filter cum active power injector in order to accommodate the dynamic variations of the source and load. As per requirement, to separate the load-demanded and switching harmonics, a new load network time constant-based passive filter design diverging from traditional passive filter design methods is demonstrated. Further, a comprehensive explanation of the current controller modeling methodology is elaborated, considering the essential bandwidth required for proficiently managing load-demanded harmonics in both grid injection and drawing modes of operation. Later, in grid injection mode, the influence of grid and system impedance interactions on the power quality is analyzed for weak grid scenarios to derive the requisite bandwidth conditions to ensure resilient power transfer. Subsequently, the experimental validation of the solar interfaced shunt active power filter (SISAPF) with active power injection capability is carried out in both grid power drawing and injection modes, demonstrating the effectiveness of the enhanced bandwidth in handling load-demanded harmonics and solar power dynamic variations. Under random solar and nonlinear load variations, this work demonstrates an adaptive controller bandwidth realization for a PV-interfaced front-end inverter (PIFI) delivering the power to the EV charging station. For an instantaneous adaptive bandwidth realization, a novel approach to model source intermittency and load nonlinearity in terms of angular frequencies is presented. In particular, the load nonlinearities are modeled in a synchronous reference frame, and it identified that the captured nonlinearity in the reactive component is sufficient to model the load dynamic variations. With the dynamic source and load modeling, a method of rolling gain adjustment for the controller is demonstrated for adaptive accommodation of source and load characteristics. Thus, with the adaptive controller rolling gain adjustment, the PIFI can handle multiple functionalities of harmonic compensation, maximum power point tracking, and simultaneous active power injection. The harmonic correction eliminates the need for a power factor correction circuit in the charging station. The simultaneous active power injection with adaptive bandwidth realization supports efficient solar integration with the load/grid network across all source/load power variations. The efficacy of the proposed sources and load dynamic modeling in realizing the adaptive controller gain for achieving multi-functionalities are demonstrated experimentally on the lab prototype. Apart from this, a new series solar inverter configuration is proposed to share the power in terms of voltage, unlike parallel inverter configurations. Elevated DC potential and circulating current due to common-mode voltage (CMV) would degrade the solar inverter's life in a single-stage parallel inverter. The proposed topology eases the stress on the DC bus and protects the

solar inverter from the issues associated with elevated DC potential (Potential-induced degradation effect, switch operating voltage stress, etc.). Therefore, this work proposes a solar-based series inverter configuration to demonstrate the superior power quality shaping with the active power injection capability in grid-interfaced nonlinear load applications. The proposed configuration realizes the AC network in series. It ensures the reduced AC filter size and DC voltage compared to the conventional inverter topologies. The series inverter configuration mimics the double switching frequency across the load, making the system's overall bandwidth higher than the conventional inverter. The improved bandwidth ensures reduced attenuation towards lower-order load-demanded harmonics. In addition, as the filter size plays a role in harmonic processing capability, in this work, an optimum filter size is derived by analyzing the nonlinear load current rise time signatures at different load resistances and filter inductances. With the appropriate filter sizing, the dynamic solar power and harmonic injection are accomplished by developing a dedicated closed-loop control mechanism for series inverters. The developed control methodology instantaneously derives combined references to individual inverters through instantaneous AC load harmonic segregation and DC solar power computation. With the derived control mechanism, the superiority of the proposed series inverter over a parallel isolated inverter in terms of enhanced harmonic compensation and dynamic solar power injection is demonstrated through experimental results.

Keywords: Active filters, Bandwidth, Characteristic impedance, Circulating current, Closed loop controller modeling, Common DC Bus, Common mode voltage, Controller gains, Current THD, dynamic control, EV charging infrastructure, Grid connected solar inverter, Grid impedance, Harmonic compensation, load time constant, non-linear loads, Parallel inverters, Passive filters, passive filter design, Power Quality, Pulse width modulation, Reactive power compensation, series inverters, shunt active filter, solar inverter, system bandwidth, switching Frequency, Three-phase inverter, Weak grid.

List of Publications

Patents

1. K. Ramachandra Sekhar, Mahesh Reddy Pundru and Baibhav Kumar Gupta **"system for optimizing dc voltages of inverter modules and a method thereof"** Application number- 202211021950.

Journals

1. P. M. Reddy, B. K. Gupta, and K. R. Sekhar, "Design and Implementation of Load Network Time Constant Computation Based Solar Active Power Filters cum Injector for Industrial loads/Grids," in IEEE Access,doi: 10.1109/ACCESS.2024.3361309

2. P. M. Reddy, A. I. Gedam and K. R. Sekhar, "A Solar Series Grid Following Harmonic Compensator With Enhanced Grid Current Shaping and Active Power Injection Capability," IEEE Transactions on Power Delivery, doi: 10.1109/TPWRD.2024.3369098

3. P. Mahesh Reddy, Aashish Kumar, Baibhav Kumar Gupta, and K. Ramachandra Sekhar, "A Front End Multi-Functional Solar Interface with Adaptive Controller Bandwidth Realization Through Source and Load Equivalent Impedance Estimation." IEEE Transactions on Power Delivery. (**Under review**)

4. P. Mahesh Reddy, and K. Ramachandra Sekhar, "Instantaneous Induced Braking Energy Modeling and Disperse Inverter Voltage Vector Synthesis for Maximum Energy Recovery in IM-based Drives." IEEE Transactions on Industrial Applications. (**Under review**)

Conferences

1. P. M. Reddy and K. R. Sekhar, "The Effect of Disperse voltage on Dynamic Braking Energy Recovery in Induction Motor Based EV Drives," 2022 IEEE International Conference on Power Electronics, Drives and Energy Systems (PEDES), Jaipur, India, 2022, pp. 1-6, doi: 10.1109/PEDES56012.2022.10080372

2. P. M. Reddy, K. Manjunath, K. R. Sekhar and B. K. Gupta, "Nonlinear Load Time-Constant Based Filter Inductance Design for PV-Driven Grid-Connected SAF/PFC in EV Charging Infrastructure," IECON 2023- 49th Annual Conference of the IEEE Industrial Electronics Society, Singapore, Singapore, 2023, pp. 1-6, doi: 10.1109/IECON51785.2023.10312368

Contents

Declaration iv

Acknowledgement v

Certificate vi

Abstract vii

List of Publications ix

List of Figures xv

List of Tables xxi

1 Introduction 1

1.1 Overview . . . 1
1.2 Power Quality . . . 2
1.2.1 Voltage Quality . . . 2
1.2.2 Current Quality . . . 2
1.3 Causes of Power Quality Problems . . . 2
1.3.1 Power Quality Problems . . . 3
1.4 Harmonics as a power quality problem . . . 4
1.5 Causes of Harmonics . . . 5
1.5.1 Harmonic distortion indices . . . 7
1.5.2 Standards of power quality . . . 7
1.6 Harmonic compensation Methods . . . 12
1.6.1 Passive compensation method . . . 12
1.6.2 Active compensation method . . . 14
1.7 Literature review . . . 16
1.7.1 Power quality issues and harmonic and reactive power compensation methods with advanced control methods. . . . 16
1.7.2 Elevated DC bus voltage and circulating current issues of parallel and single inverter topologies. . . . 18
1.8 Motivation . . . 20
1.8.1 Government Initiatives to Promote Clean Energy Generation . . . 20
1.9 Organization of Thesis . . . 24

2 Design and Implementation of Load Network Time Constant Computation Based Solar Active Power Filters Cum Injector for Industrial Loads/Grids 27

2.1 The Solar interfaced shunt active power filter 27

2.2 The proposed load network time constant computation based passive inductance design method 27

2.2.1 Minimum filter inductance design 28

2.2.2 Maximum filter inductance design 30

2.3 The SiSAPF's closed-loop controller modeling 33

2.3.1 Mode-1 operation 35

2.3.2 The selection of controller gains based on load network time constant 38

2.3.3 Mode-2 operation 41

2.3.4 The selection of controller gains based on the mode of operation . . 44

2.4 Results and Discussion 45

2.5 Conclusion 54

3 A Front End Multi-Functional Solar Converter with Adaptive Controller Bandwidth Realization Through Source and Load Equivalent Impedance Estimation 57

3.1 The proposed offboard PV interfaced charging circuit with front end inverter 57

3.2 Estimation of nonlinear load angular frequency dynamics 60

3.2.1 The requirement of canceling the source power angular frequency for realizing the nonlinear load demanded bandwidth 62

3.2.2 The proposed PIFI's closed-loop controller design with rolling gain adjustment mechanism 64

3.2.3 The proposed rolling controller gain adjustment in digital domain . 66

3.3 Results and Discussion 68

3.3.1 The rolling gain adjustment adaptive to load power variations at constant PV power 69

3.3.2 The rolling gain adjustment adaptive to PV power variations at constant load power 72

3.4 Conclusion 76

4 A Solar Series Grid Following Harmonic Compensator with Enhanced Grid Current Shaping and Active Power Injection Capability 79

4.1 The Solar Active Power Cum Harmonic Injector(SAPCHI) 79

4.1.1 The series inverter switching sequence for virtual load frequency doubling 80

4.2 Passive filter inductance design based on the load network time constant . . 82

4.3 Input port DC chopper design specifications and corresponding solar power reference generation for the series inverter 84

4.4 Closed loop controller modeling for the proposed series inverter harmonic and active power injector 85
4.4.1 Modes of operation of harmonic compensator 86
4.4.2 System impedance modeling for the controller design 87
4.4.3 Designing of the PI controller 90
4.5 Results and Discussion 91
4.5.1 Hardware validation for harmonic compensation 92
4.5.2 The experimental validation of proposed series configuration operational capability of simultaneous active power and harmonic injection 93
4.6 Conclusion 98

5 Conclusion **101**
5.1 Summary 101
5.2 Scope of Future Research 103

References **105**

List of Figures

1.1 a) Single-tuned filter b) double-tuned filter c) second-order high-pass filter d) Third-order high-pass filter e) Third-tuned passive filter. 13
1.2 Configuration of Shunt active filter 15
1.3 Configuration of Series active filter 15
1.4 Configuration of hybrid active filter(Unified power quality compensator(UPQC)) 16
1.5 Energy consumption by sources 21
1.6 Renewable electricity production share in different countries. 22
1.7 Cumulative installed capacity of grid interactive renewable power by type (in MW) (X-axis: Renewable sources; Y-axis: Energy generation in MW) . 23

2.1 The solar interfaced shunt active power filter schematic with control diagram. 28
2.2 The SiSAPF's network single line diagram with the realization of filter inductance as a decomposed harmonic back-EMFs. 29
2.3 The variation of the current harmonics along with the offered resistance and corresponding back emf offered by the filter inductor (L_f) at two frequencies f_{sw1} and f_{sw2}. 30
2.4 The non-linear load current profile with change in network inductance L_{NL}. 31
2.5 comparison of filter design methods at different powers. 32
2.6 comparison of grid currents for the load currents at different filter design methods. 33
2.7 The variation of three phase nonlinear load currents and corresponding real and reactive component (I_{dref} and I_{qref}) profiles in SRF at different filter inductance and network power. 34
2.8 The single line diagram of the power network demonstrates the power interaction between SiSAPF, grid, and nonlinear load. 35
2.9 The signal flow diagram consolidated the plant model and controller. 36
2.10 The Bode diagram and Root locus of SiSAPF's open-loop transfer function with the variation of the filter inductance. 38
2.11 Step response SiSAPF's closed-loop transfer function with varying K_p. . . . 39
2.12 Root locus of SiSAPF's open-loop transfer function with varying K_p. 39
2.13 THD comparison of proposed and different filter inductances in grid drawing and injection modes under proposed controller gain design methods. 40
2.14 The phasor diagram representing the PCC voltage oscillations in the weak grid due to coupling angle γ in grid power injection mode. 42

2.15 a) Allowable controller range for the SiSAPF from minimum to maximum controller gain with respect to when the system changes from grid drawing mode to grid injection mode. b) The zoomed portion of the grid-injected mode region to ensure the limit for the grid-injected power. 44
2.16 The SiSAPF hardware prototype developed in the lab. 45
2.17 The a-phase non linear load current (X-limit: 2A/div, Y-limit: 10ms/div) along with equivalent current correspond to real (i_{dl}) and reactive power (i_{ql}) (X-axis: 50mA/div, Y-axis: 10ms/div). 46
2.18 The 3-phase inverter currents (top trace), load currents (Middle trace), and grid currents (bottom trace) with no compensation from the SiSAF (Left) and corresponding grid current harmonic spectrum (Right) 47
2.19 The experimental comparison when SiSAPF operates in harmonic compensation mode with Filter inductance $L_f = 0.6mH$ computed through the proposed method (left figure) and $L_f = 10mH$ computed using ripple-based filter design (Right figure). 48
2.20 The effect of different filter inductances on SiSAPF circuit and grid current THD. The SiSAPF current (top trace X=10ms/div, Y=5A/div), nonlinear load current(middle trace X=10ms/div, Y=5A/div), and grid current(bottom trace X=10ms/div, Y=5A/div)and their corresponding grid current THD (right figures). 50
2.21 The effect of different system time constant over network time constant for SiSAPF circuit on grid current THD. In the left figures, SiSAPF current (top trace X=10ms/div, Y=5A/div), nonlinear load current(middle trace Y=5A/div), and grid current(bottom trace Y=5A/div) for one designed filter inductance and their corresponding grid current THD (right figures). . 51
2.22 The effect of different system time constant over network time constant for SiSAPF circuit on grid current THD. In the left figures, SiSAPF current (top trace X=10ms/div, Y=5A/div), nonlinear load current(middle trace Y=5A/div), and grid current(bottom trace Y=5A/div) for one designed filter inductance and their corresponding grid current THD (right figures). . 52
2.23 The SiSAPF current(top trace X=2sec/div, Y=10A/div), three-phase non-linear load current(middle trace Y=5A/div), and grid current(bottom trace Y=5A/div). The zoomed portions correspond to the dynamic variation of SASAF power from 10 W to 790 W(left figure X=10msec) and 790 W to 1400 W(right figure). 53
2.24 The SiSAPF current(top trace X=10ms/div, Y=10A/div), three-phase load current(middle trace Y=5A/div), and grid current(bottom trace Y=5A/div) and corresponding grid injected current %THD with mimicked weak grid condition. 54

3.1 The proposed PV interfaced front-end inverter-based offboard charger. . . . 58

3.2 The Nonlinear profile of the PIFI filter inductance requirement with varying active power injection and switching frequency. 58

3.3 The estimation of system angular frequency (ω_{sys}) at different solar irradiance computed using maximum power tracking algorithm. 59

3.4 The PIFI angular frequency ($\omega_{sys} = \frac{R_{ac}}{L_f}$ realization with injected powers at different filter inductance. 59

3.5 Separation of active and reactive components from the nonlinear load current (a) Three-phase grid voltages (top), and corresponding nonlinear load currents (bottom) (b) The space plot formation of the load current in stationary reference frame α-β plane (c) And corresponding reflection on α-axis (top trace) β-axis (bottom) (d) The load current realization in the synchronous reference frame with the grid voltage angle θ on d-axis (top) and q-axis (bottom). 60

3.6 The i_{lq} variations (encapsulated load current) with change in load power(left trace) and network inductance(Right trace). 61

3.7 The adaptive estimation of R_{nl} and L_g for a dynamic non linear load frequency (ω_{nl}) generation. 62

3.8 The recommended region of non linear load angular frequency (ω_{nl}) map without cancellation PIFI angular frequency (ω_{sys}) influence. 63

3.9 The PIFIs angular frequency trajectory with the arbitrary placement of controller root (left) and root placement precisely at the system angular frequency (right) with varying filter inductance values. 63

3.10 The PIFIs angular frequency trajectory with the arbitrary placement of controller root (left) and root placement precisely at the system angular frequency (right) at various injected solar power. 64

3.11 The signal flow diagram consolidated plant model along with the controller. 65

3.12 The dynamic system pole cancellation technique for an adaptive rolling system bandwidth adjustment in synchronous with the nonlinear load variations. 66

3.13 The signal flow diagram of PIFI switching pulses synthesis with adaptive controller gain adjustment mechanism. 67

3.14 The magnitude and phase plots of the closed loop transfer function derived in s-domain (3.19) (3.23) and Z-domain (3.26),(3.27). 68

3.15 The load current rise time reference sampling at the rate of $T_s = 1e^{-5}$ and $1e^{-6}$ along with switching frequency (left trace), The closed loop response load current (i_q) tracking in Z-domain with $T_s = 1e^{-5}$ and $1e^{-6}$ (right trace). 68

3.16 The experimental setup for validating the proposed rolling gain adjustment mechanism. 69

3.17 The adaptive estimation of load equivalent resistance (R_{nl}) (bottom trace (x-axis:1sec/div, Y-axis:0.5V/div)) with the change in load current (top trace x-axis:25msec/div Y-axis:10A/div). The zoomed portion of the R_{nl} with the power variation from 550W to 760W (bottom left figure x-axis:25msec) and 760W to 1500 W (bottom right figure X:25msec). 70

3.18 The three-phase load current (top trace x:1sec/div Y:20A/div), dynamic variations of ω_{nl}, K_P, and K_I (middle traces Y:1V/div) and corresponding three-phase grid currents (bottom trace Y:20A/div) for the load power variations from 550W to 760W (The zoomed portion bottom left x:10msec/div) and from 760W to 1500W (The zoomed portion bottom right figure). 70

3.19 The nonlinear load and PIFI's i_d (top two traces x:1sec/div Y:0.5A/div) i_q profiles (bottom overlapping traces x-axis:1sec/div Y-axis:0.5A/div). The corresponding zoomed portion depicting load power changes from 550W to 760W (bottom left figure x:10msec) and 760W to 1500W (bottom right figure). 71

3.20 The three-phase inverter currents (top trace), three-phase load current (middle trace), and three-phase grid currents (bottom trace) along with the harmonic spectrum without harmonic compensation (left figure) and with harmonic compensation (right figure). 71

3.21 The solar PV maximum power tracking and its variations (top figure) and corresponding PIFI's three-phase current (second trace x:1sec/div Y:20A/div), the three-phase load current (Third trace Y:20A/div) and grid current (bottom trace Y:20A/div). The corresponding zoomed portion shows the load power variation from 550W to 760W (bottom left figure x:10msec) and 760W to 1500W (bottom right figure). 72

3.22 The three-phase inverter current (top trace x:1sec/div Y:20A/div), dynamic variations of ω_{sys}, and K_I (middle traces Y-axis:1V/div) and corresponding three-phase grid currents (bottom trace Y:20A/div) for the PIFI power variations from 75W to 300W (The zoomed portion bottom left x:10msec/div) and from 300W to 750W (The zoomed portion bottom right figure). 73

3.23 The nonlinear load and PIFI's i_d (top two traces x:1sec/div Y:0.5A/div) i_q profiles (bottom overlapping traces x-axis:1sec/div Y-axis:0.5A/div). The corresponding zoomed portion depicts PIFI power changes from 75W to 300W (bottom left figure x:10msec) and 300W to 750W (bottom right figure). 73

3.24 The PIFI's three-phase inverter current (top trace x:1sec/div Y:20A/div), the three-phase load current (middle trace Y:20A/div) and grid current (bottom trace Y:20A/div). The corresponding zoomed portion shows the PIFI power variation from 75W to 300W (bottom left figure x:10msec) and 300W to 750W (bottom right figure). 74

3.25 The PIFI's three-phase inverter current (top trace x:1sec/div Y:20A/div), the three-phase load current (middle trace Y:20A/div) and grid current (bottom trace Y:20A/div). The corresponding zoomed portion shows the PIFI power variation from 75W to 750W (bottom left figure x-axis:10msec) and 750W to 1500W (bottom right figure). 75
3.26 The dynamic three-phase grid current behavior with the changeover from the fixed controller to proposed adaptive gain adjustment (X:10msec/div Y:10A/div). 75
3.27 %THD comparison with fixed controller gains and the proposed rolling gain adjustment. 76

4.1 The circuit diagram of proposed solar series active power cum harmonic injector with closed-loop control 79
4.2 Switching hexagon of individual inverters in series inverter topology. 80
4.3 Realizing the series inverter topology pulse pattern in two sampling time intervals. 81
4.4 The non-linear load current variation with change in inductance L_g (left trace) and loading conditions R_L (Right trace). 82
4.5 The variation of back emf and harmonic current magnitude corresponds to the harmonic component. 84
4.6 The input ports maximum power point tracking and corresponding reference generation for series inverter 85
4.7 The single line diagram of a series inverter harmonic compensator with a different mode of operations. 87
4.8 The equivalent circuit representation with transformer and transforming all parameters to a primary side of the isolating transformer. 88
4.9 The block diagram of the consolidated plant model along with the controller. 89
4.10 Open loop plant transfer function bode plot for series and parallel inverter harmonic cum active power injector. 89
4.11 Open-loop transfer function bode plot for a series inverter with different controller proportional gains. 90
4.12 Step response of closed-loop transfer function for series and parallel harmonic cum active power injector. 91
4.13 Closed-loop transfer function step response for a series inverter with different controller proportional gains (K_p). 91
4.14 The experimental lab prototype for demonstrating series and parallel configuration. 92
4.15 Inverter currents (top trace), load currents (Middle trace), and grid currents (bottom trace) along with grid current THD for parallel (Fig. 4.15b) and series (Fig. 4.15c) harmonic compensator. 93
4.16 The series configuration behavioral studies at different solar irradiance. . . . 94

4.17 The input (DC) and output (AC) current and voltage signatures of proposed series configuration with asymmetrical solar irradiance variations. 96
4.18 The series SAPCHI experimental results with dynamic load variation. . . . 97

List of Tables

1.1 Power quality standards 8
1.2 IEEE-519 Voltage Distortion limits 11
1.3 IEEE-519 Current Distortions limits for General Distribution Systems (120V through 69 KV) 11

2.1 Specifications of Filter Design. 46
2.2 The Nonlinear load network parameters along with SiSAPF system parameters at different SiSAPF's operating modes. 49
2.3 Considered parameters for weak grid condition experimentation. 53

3.1 Experimental operating parameter of solar synchro active power filter . . . 69

4.1 Comparison of different inverter topologies for AC filter design. 83
4.2 Experimental operating parameter of series and parallel harmonic compensator. 92
4.3 Different modes of operation of the series harmonic compensator. 95

5.1 PIFI with available modes of operation 102

Chapter 1

Introduction

1.1 Overview

Recent advances in power electronics have transformed the landscape of electrical engineering, introducing solid-state controllers with widespread applications across industrial, commercial, and residential sectors. Although these semiconductor-based devices offer notable advantages in efficiency and control, exhibit nonlinear operational characteristics. Consequently, they introduce waveform distortions in voltage and current at the point of common coupling (PCC) for industrial loads. With the integration of thousands of these devices into modern power systems, they have emerged as primary sources of pollution and distortion, compromising power quality. This degradation is evidenced by waveform distortions and other voltage-related issues. Regulatory measures have been implemented to address these challenges to mitigate the adverse effects on power quality and ensure a consistent and reliable electricity supply.

Several methods are employed to address power quality issues and adhere to standards. Passive filters are commonly deployed to curtail harmonic current flow in distribution systems. However, their effectiveness is limited to specific harmonics and may induce resonance within the power network. Power capacitors are utilized to enhance the power factor by supplying reactive vars. Yet, conventional power factor correction approaches and harmonic passive filters struggle to adapt to varying load conditions, rendering them impractical at the distribution level where specific load conditions or system states prevail. Consequently, power electronic solutions have garnered attention due to power system dynamics and the stochastic nature of harmonics over short durations. Custom power electronic devices are engineered to rectify distortions at the distribution level, encompassing issues like voltage sags, surges, transients, reactive power, and harmonics. Examples include Dynamic Voltage Regulators (DVRs), Static Synchronous Compensators (STATCOMs), and Active Power Filters (APFs), offering tailored solutions for distribution systems [1],[2].

This chapter provides adequate background on power quality problems, standards, also the integration of renewable energy sources into active filters, and available methods for control.

1.2 Power Quality

The term ”power quality” encompasses the voltage, current, and frequency variation within an electrical system. It refers to any deviation from the ideal sinusoidal waveform at the rated frequency, with amplitudes corresponding to the rated rms values for all three phases. Power quality issues can manifest in voltage, current, and frequency deviations, potentially leading to the failure or misoperation of customer equipment. The IEEE dictionary, referencing IEEE Std 1100, defines power quality as ”the concept of powering and grounding sensitive equipment in a manner that is suitable for the operation of the equipment” [3].
From the perspective of electric power customers, the primary concern regarding power quality lies in achieving an ideal voltage waveform. Therefore, customer interest in power quality is predominantly centered on voltage quality. Conversely, utility companies have a broader focus, considering both voltage and current quality as crucial aspects. This classification underscores the importance of understanding definitions for both voltage and current quality [4].

1.2.1 Voltage Quality

Voltage quality pertains to the standard of the electricity supplied by utility providers to consumers. It primarily deals with deviations of the voltage waveform from the ideal sinusoidal waveform.

1.2.2 Current Quality

Current quality is a complementary concept to voltage quality, focusing on deviations of the current waveform from the ideal sinusoidal waveform. In addition to aligning with the demanded current waveform outlined by utility providers, the current sinusoidal wave ideally synchronizes with the supplied voltage to minimize transmitted apparent power. This synchronization optimizes power system ratings and reduces harmonic content in the waveform. Given the close relationship between voltage and current, deviations from ideal conditions in either parameter often result in corresponding deviations in the other, with a high probability.

1.3 Causes of Power Quality Problems

Causes of power quality deterioration are classified into two main categories, i.e., natural and man-made.

1. Natural causes
    - Fault or lighting stroke on power system lines
    - Equipment failure

2. Man made causes

    - Transformer excitation, capacitor or feeder switching
    - Switching of Power electronics load such as UPS, ASD, Micro-controllers, Solid-state switching devices
    - Use of arc furnaces, induction-heating systems
    - Sudden or frequent switching of large loads

1.3.1 Power Quality Problems

A wide range of disturbances has been documented, spanning from sub-cycle duration to long-term steady-state problems in electrical systems. These disturbances include short interruptions, voltage sags, voltage swells, voltage, and current transients, harmonics/waveform distortions, voltage fluctuations, voltage flicker, voltage and current unbalance, phase angle jumps, over-voltage, under-voltage, and power frequency variations[5],[6]. Among these disturbances, waveform distortion, voltage flicker, and voltage imbalance at the distribution system are deemed particularly serious. Consequently, a growing focus is on regulating voltage imbalance[7] and compensating for harmonics in distribution systems [8],[9].

Waveform Distortion

Waveform distortion refers to the periodic deviation of voltage or current from the ideal sinusoidal waveform. It encompasses five main types of distortions: DC offset, harmonics, interharmonics, notching, and noise.

1. **DC offset:** DC offset occurs when DC voltage or current is present in an AC power system. This phenomenon can arise from various sources, including geomagnetic disturbances or the ground return operating mode in monopolar HVDC links. If uncontrolled, DC offset can lead to adverse effects such as magnetic saturation, increased heating, and reduced transformer lifespan. Therefore, effective measures to mitigate DC offset are essential to maintain the integrity and reliability of the power system.

2. **Harmonics:** Harmonics refers to additional frequencies present alongside the normal sinusoidal voltage and current waveforms. Typically, these frequencies are integer multiples of the fundamental frequency. When the frequencies of these voltages or currents are not integer multiples of the fundamental, they are termed interharmonics. The primary harmonic and interharmonic distortion sources are non-linear loads, such as power electronic converters and controllers. As harmonic currents flow through the system impedance, they cause a voltage drop for each harmonic, resulting in voltage harmonics appearing at the load and leading to power quality issues. The Total Harmonic Distortion (THD) is the most common measure of distortion, applicable to both current and voltage waveforms, and is given by:

$$THD = \frac{\sqrt{\sum_{h=2}^{h_{max}} X_h^2}}{X_1} \tag{1.1}$$

where X_h is the rms value of the harmonic(h) component of X(current or voltage). The main disadvantages of harmonic distortion are[8]:

- Extra losses and heating in rotating machine and capacitors
- Over voltages due to resonance
- Interference with ripple control systems used in demand side management
- Telephonic interference caused by noise on telephone lines

3. **Notching:** Notching is a periodic disturbance in the voltage waveform introduced by power converters during the commutation of current from one phasor to another. This phenomenon can lead to multiple zero voltage crossings, which may cause digital clocks to run fast, as their design relies on the number of crossings per cycle. Notching is considered a steady-state phenomenon and can be analyzed using the Fourier series, which provides a harmonic spectrum of the affected voltage waveform.

Voltage Unbalence

Voltage imbalance in three-phase systems refers to differences in the magnitudes of phase voltages or phase-to-phase voltages. This imbalance is assessed using symmetrical components, which provide an index known as the voltage utilization factor to describe the system's unbalance.

Unbalanced voltages pose significant risks to induction machines, decreasing machine efficiency and potentially leading to motor failure. Additionally, power electronics converters are negatively impacted by voltage unbalance. In the case of diode rectifiers, unbalanced voltages influence the input current harmonics, resulting in the appearance of uncharacteristic triplen harmonics like the 3rd and 9th harmonics. Furthermore, voltage imbalance may induce excessive currents in specific phases, triggering overload protection circuits in adjustable speed drives. These increased currents can lead to overheating diodes and reduce DC link capacitors' lifespan [7].

1.4 Harmonics as a power quality problem

Electric power systems are deemed to provide excellent quality when they deliver sinusoidal voltage and current waveforms at a single, consistent frequency. However, harmonic distortion challenges this ideal. Harmonics in power quality denote the presence of distorted periodic voltage and current waveforms, which can be mathematically described through Fourier analysis as a summation of an infinite series of frequencies. This series

includes the fundamental frequency and its multiples, known as higher-order harmonics.

$$v(t) = \sum_{n=1}^{\infty} v_n \sqrt{2} sin(n.\omega t + \theta_{v,n}) \tag{1.2}$$

$$i(t) = \sum_{n=1}^{\infty} i_n \sqrt{2} sin(n.\omega t + \theta_{i,n}) \tag{1.3}$$

Unlike other power quality issues, harmonic distortion is a steady-state phenomenon that persists continuously. This constant presence means that the stresses induced, although not immediately evident, can eventually lead to accumulative effects that are often straightforward to explain. Potential problems attributed to harmonics include [10]:

- Malfunction of sensitive equipment
- Random tripping of circuit breakers
- Flickering lights
- Very high neutral currents
- Overheated phase conductors, panels, and transformers
- Reduced Power factor
- Reduced system capacity
- Excitation of resonance phenomena resulting in significant overvoltages and/or overcurrents
- Electromagnetic Interference(EMI) problems with sensitive electronic equipment
- Incorrect reading meters

The injection of harmonics into the network presents significant challenges, including heightened losses in the transmission and distribution systems, oversized equipment in the AC system caused by higher current draw relative to real power demand, and diminished efficiency due to increased losses and inadequate voltage regulation.

1.5 Causes of Harmonics

Advancements in power electronic devices have significantly simplified human life and reduced workload. These devices are predominantly employed as load-side equipment to modify power and voltage levels, drawing power from either the grid or renewable sources. Their prevalence has recently surged with the widespread adoption of semiconductor devices. Traditionally, harmonic generation in electric power systems was attributed to saturated iron in transformers, induction machines, electric arc furnaces, welding equipment, etc.,[11],[12],[13]. However, with the evolution of semiconductor technology,

power electronic devices have emerged as additional sources of harmonics. Consequently, the modern classification of harmonic sources is as follows:

- saturable devices
- Arcing devices
- Power electronic devices

Saturable devices encompass transformers and rotating machines such as AC motors and generators. Under typical operating conditions, modern transformers and rotating machines do not introduce significant distortion into the network. However, their harmonic contribution can become considerable during transient disturbances or when operating beyond their normal range. Within power utility equipment, harmonics primarily originate from transformer core saturation during energization. Additionally, the growing implementation of Flexible AC Transmission Systems (FACTS) is expected to further contribute to harmonic distortion in utility equipment.

Arcing devices include ARC furnaces, arc welders, and discharge-type lighting fixtures such as fluorescent, sodium vapor, and mercury vapor lamps equipped with magnetic ballasts. Nonetheless, the impedance of the ballast or furnace leads functions as a buffer, resulting in only moderate supply voltage distortion. The presence of both arc ignition delays and the highly nonlinear voltage-current characteristics of the arc introduces harmonics of the fundamental frequency.

Power electronic devices employed for power conversion in industries are the primary contributors to harmonics in the grid. These devices include large power converters in metal industries and high-voltage DC transmission, medium-sized converters in manufacturing industries for motor control and railway applications, and low-power rectifiers in single-phase supplies such as television sets and battery chargers. AC-DC power conversion has predominantly relied on diode or phase-controlled rectifiers in industrial settings. These rectifiers operate as nonlinear loads on power systems, drawing input currents rich in harmonics and exhibiting poor supply power factor. Consequently, they create power quality issues for the power distribution network and other nearby electrical systems [11],[14],[15]. AC/DC power converters find extensive application in various fields, including power supplies, DC motor drives, adjustable-speed AC drives, HVDC transmission, switch-mode power supplies (SMPS), utility interface with non-conventional energy sources, welding technology, power supplies for telecommunications systems, aerospace, and more.

Battery chargers are widely used in the domestic sector to charge various devices such as mobile phones, computers, TV receivers, and electric vehicle (EV) chargers. However, these battery chargers often generate high levels of zero-sequence triplen harmonic content. This harmonic content can overload the neutral circuit, posing challenges for the electrical system. The current harmonics produced by nonlinear loads propagate throughout the power network. As these harmonic currents traverse the system impedance, they induce

a voltage drop for each harmonic. Consequently, voltage harmonics manifest at the load bus, giving rise to power quality issues.

1.5.1 Harmonic distortion indices

Harmonic distortion levels are characterized by the complete harmonic spectrum, which includes the magnitude and phase angle of each harmonic component. In assessing the level of distortion, various indices are considered. In addition to individual voltage and current harmonics (V_n and I_n), Total Harmonic Distortion (THD) is widely regarded as a comprehensive measure. THD quantifies the portion of higher-order harmonics relative to the fundamental, concisely representing the overall distortion level.

$$THD_V = \frac{\sqrt{\sum_{n=2}^{\infty} {V_n}^2}}{V_1} \tag{1.4}$$

$$THD_I = \frac{\sqrt{\sum_{n=2}^{\infty} {I_n}^2}}{I_1} \tag{1.5}$$

It is important to emphasize that measurements of both the fundamental component and higher-order harmonics should be conducted simultaneously according to the THD definition. This aspect is crucial for quantifying current levels in the distribution system or voltage levels at the PCC, where the utility can supply power to other customers. Typically, distortion is expressed as a percentage of the load value rather than the fundamental value. This metric is known as Total Demand Distortion (TDD) and is calculated as follows:

$$TDD_V = \frac{\sqrt{\sum_{n=2}^{\infty} {V_n}^2}}{V_L} \tag{1.6}$$

$$TDD_I = \frac{\sqrt{\sum_{n=2}^{\infty} {I_n}^2}}{I_L} \tag{1.7}$$

Another significant distortion index is the individual harmonic distortion factor (HF) for specific harmonics h. HF is defined as the ratio of the RMS harmonic to the fundamental RMS value of the waveform, expressed as $HF = \frac{V_h}{V_1} \times 100\%$.

1.5.2 Standards of power quality

The establishment of power quality standards is crucial for power quality analysis, providing guidelines for testing, measuring, and evaluating power quality. Both the IEEE and IEC standards extensively cover power quality and its associated issues, offering potential solutions. Table 1.1 presents a selection of power quality standards along with their suggested guidelines.

Various standards are established to regulate harmonics resulting from nonlinear loads. The IEEE standard was initially introduced in 1991, offering preliminary guidelines for system harmonics limitations, which were subsequently revised in 1992. IEEE 519-1992

Table 1.1: Power quality standards

S.No	Type of PQ standard	Description of standard	Guidelines
1	IEEE Std. 141-1993[16]	Planning of electric power distribution for industrial plants	This IEEE standard addresses various aspects concerning electric power in industrial distribution systems. It provides comprehensive guidelines for electrical design, covering topics such as voltage limits, grounding, harmonics, protection, and short circuit calculations. The standard aims to ensure the safety of life, reliability, maintenance, and preservation of property in industrial settings.
2	IEEE Std. 142-2007[17]	Related to Industrial and Commercial Power Systems Grounding.	This standard addresses the operation of sensitive electrical devices in both grounded and ungrounded conditions, particularly concerning static electricity and lightning protection. It covers various grounding issues, including neutral grounding, delta corner grounding, and mid-tap grounding, and provides potential counter solutions for commercial and industrial power systems. Discussions include the type of grounding, location, and selection of equipment for grounding the neutral circuit, as well as the interconnection between equipment and ground rods.
3	IEEE Std. 519-2014[18]	Significance of Harmonic Control in Electrical Power Systems	This IEEE standard delves into the impact of different power electronic converters and both linear and nonlinear loads on voltage and current waveform distortion, addressing the perspectives of both customers and system designers. It also establishes targets for power quality at the point of common coupling (PCC), defining PCC as the source and load intersection point. This standard aims to establish steady-state limitations on harmonics, considering worst-case conditions.
4	IEC 61000 - 3 - 2:2018[19]	Electro Magnetic Compatibility (EMC) - harmonic current emissions limits	This standard addresses the limitations of harmonic current injection from equipment with a rating of less than 16 A per phase in low-voltage distribution systems.

5	IEEE Std. 1250-2018[20]	Issues related to Voltage Quality in Power Systems	This IEEE standard focuses on the impact of voltage quality issues, such as surges, distortion, and faults, on the operation of sensitive equipment including computers, power electronic converters, and electronic household appliances. It covers steady-state voltage limits, flicker, factors contributing to the degradation of power system performance, and potential solutions to enhance voltage quality. Additionally, the standard examines the effects of momentary voltage disturbances on sensitive end-user equipment and discusses waveform distortion limits in detail.
6	IEEE Std. 1159-2009[21]	Monitoring of Electric Power Quality	This IEEE standard provides essential guidelines for monitoring power quality (PQ), including discussions on conducted electromagnetic interference in both single-phase and three-phase AC power systems. It covers methods for quantifying PQ disturbances and offers insights into the applications and interpretation of data obtained from PQ monitoring devices within power systems.
7	IEEE Std. 1668-2017[22]	Voltage Sag and Short Interruption Ride-Through Testing for End-Use Electrical Equipment Rated Less than 1000 V	This IEEE standard addresses issues related to voltage sag and voltage ride-through performance, focusing on suitable testing methods for low-voltage power systems (less than 1 kV). It provides a detailed analysis of the probability of equipment malfunction or shutdown due to various types of voltage sags lasting less than 1 minute. Additionally, the standard discusses minimum voltage sag immunity guidelines based on available data, aiming to mitigate power quality issues concerning sensitive electrical and electronic equipment. It establishes procedural steps for testing methods and performance criteria to assess the influence of voltage sags in proximity to the end user's electrical environment.

8	IEEE Std. 493-2007[23]	Design of Reliable Industrial and Commercial Power Systems	This standard outlines the planning and design criteria for commercial and industrial distribution systems, emphasizing fundamental reliability analysis. It encompasses various aspects such as probability methods, reliability evaluation, economic assessment, etc., to ensure continuous power supply, analyze voltage sags, and address emergency and standby power systems, among other related topics.
9	IEEE Std. 1564-2014[24]	Guide for Voltage Sag Indices	This IEEE standard outlines the development of necessary voltage sag indices along with the method of calculation. Applicable to both transmission and distribution levels, the standard quantifies the severity of various types of voltage sags on the entire system and at specific locations within the power system.
10	IEEE Std. 1547-2018[25]	Interconnection and Interoperability of DERs with Associated Electric Power Systems Interfaces	This IEEE standard addresses various aspects concerning the interconnection and interoperability of Distributed Generations (DGs) with the existing utility grid. It covers safety, security, and maintenance requirements, including the evaluation of performance, operation, and testing for the interconnection of different types of DGs to the power system. Additionally, the standard provides detailed discussions on testing procedures for 60 Hz power systems, regardless of location or production. It outlines general requirements such as power quality, adaptability to abnormal conditions, islanding, and specifications for testing, design, installation, and commissioning for all types of DGs. Consequently, this standard enhances the flexibility of interconnecting various DG technologies into the utility grid during interconnection and throughout the Distributed Energy Resource's (DER) service life.

11	IEEE Std. 1453-2015 [26], and IEC 61000-4-15[27]	Analysis of Fluctuating Installations on Power Systems	This standard addresses the impact of variable loads on voltage fluctuations and background flicker, detailing the measurement method for flicker using a flicker meter. It establishes flicker limits by considering both short-term and long-term indices and outlines the process for evaluating each load's contribution to flicker, as well as assessing flicker against emission limits.

delineates recommended practices and requirements for harmonic control in electrical power systems, providing guidelines for determining acceptable limits. The IEC 61000 series comprises internationally accepted standards. IEEE 519:2014 outlines harmonic standards, specifying limits on voltage and current harmonic distortion for low voltage, primary and secondary distribution, sub-transmission, and high voltage transmission systems. The table below presents recommendations for harmonic voltage distortion limits across different system voltage levels.

Table 1.2: IEEE-519 Voltage Distortion limits

Bus voltage V at PCC	Individual harmonic distortion (%)	Total harmonic distortion THD(%)
V $\leq$ 1 KV	5.0	8.0
1 KV $<$ V $\leq$ 69 KV	3.0	5.0
69 KV $<$ V $\leq$ 161 KV	1.5	2.5
161 KV $<$ V	1.0	1.5

The harmonic limits for current depend on the ratio of Short Circuit Current(SCC) at the PCC to the average load current of maximum demand over one year, as illustrated in the table below:

Table 1.3: IEEE-519 Current Distortions limits for General Distribution Systems (120V through 69 KV)

I_{sc}/I_L	3$\leq$ h $<$ 11	11 $\leq$ h $<$ 17	17 $\leq$ h $<$ 23	23 $\leq$ h $<$ 35	35 $\leq$ h $\leq$ 50	TDD
$<20^c$	4.0	2.0	1.5	0.6	0.3	5.0
20 $<$ 50	7.0	3.5	2.5	1.0	0.5	8.0
50 $<$ 100	10.0	4.5	4.0	1.5	0.7	12.0
100 $<$ 1000	12.0	5.5	5.0	2.0	1.0	15.0
$>$ 1000	15.0	7.0	6.0	2.5	1.4	20.0
Even harmonics are limited to 25% of the odd harmonics limits above						
I_{sc}= maximum short-circuit current at the PCC. I_L= maximum demanded load current at the PCC.						

1.6 Harmonic compensation Methods

Nonlinear loads generate harmonic currents that can propagate through electrical systems and ultimately return to the source. These harmonic currents can induce detrimental effects on the power system, as elaborated in section 1.4. Concurrently, the reactive power demand of nonlinear loads increases losses in transmission and distribution lines, resulting in the underutilization of source capacity. This decrease in system efficiency stems from the higher current drawn for a given real power demand, thereby leading to overrated equipment within the AC system. Consequently, suitable methods are necessary to compensate for nonlinear loads' harmonic and reactive power requirements, aligning with harmonics standards outlined by various international regulations. Several methods exist for compensating harmonics and reactive power, with conventional approaches beginning with harmonic filters, which are further classified into passive and active filters.

1.6.1 Passive compensation method

Passive filters utilize passive components like resistors, inductors, and capacitors, configured in a combination tuned to the frequency of the harmonic to be filtered. They can be categorized as tuned filters or high-pass filters. Typically connected in parallel with nonlinear loads such as diode/thyristor rectifiers and AC electric furnaces, passive harmonic filters effectively filter harmonic currents from the line [28]. Shunt passive filters also enhance power factor by compensating reactive power, besides harmonic compensation [29]-[30]. However, while this feature offers advantages in many scenarios, it may not be universally beneficial. The circuit configuration of a per-phase passive filter is illustrated in Fig. 1.1. Installing such filters near nonlinear loads establishes low impedance paths for specific harmonic frequencies, effectively absorbing dominant harmonic currents emitted by the load. As the filter's impedance is lower than the source's, harmonic frequency currents circulate between the load and the filter, diverting the desired harmonic current away from the source and other loads in the power system. Additional tuned filters may be deployed parallel to filter out other harmonic frequencies if necessary. The effectiveness of each single-tuned filter's low-impedance path is influenced by the filter inductor's quality factor (Q), which dictates the sharpness of tuning. While a second-order high-pass filter offers robust filtering performance across a broad frequency range, it typically incurs greater fundamental frequency loss than a single-tuned filter.

When applying a passive filter, meticulous attention is necessary. The series passive filter is integrated into the system in series with the load. The parallel inductance and capacitance are precisely tuned to establish high impedance at specific frequencies, thereby obstructing the flow of harmonic currents of the tuned frequency exclusively. The benefits and drawbacks of a passive filter can be briefly outlined as follows [31],[29],[28]:

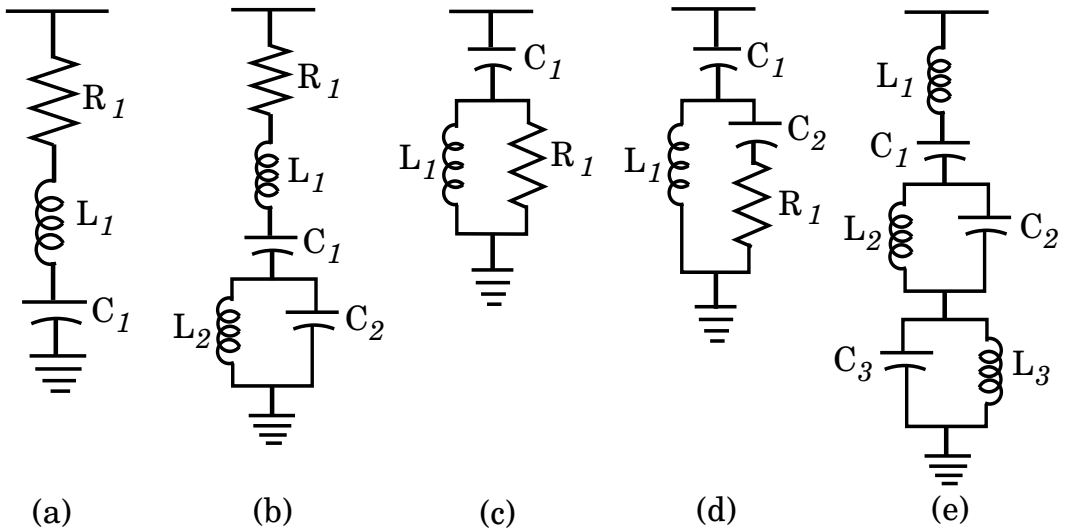

Figure 1.1: a) Single-tuned filter b) double-tuned filter c) second-order high-pass filter d) Third-order high-pass filter e) Third-tuned passive filter.

Advantages of Passive filter

- Effectively designed passive filters can be deployed in large Mvar ratings, offering nearly maintenance-free operation.
- They are more cost-effective to deploy compared to synchronous condensers.
- They can achieve a rapid response time of one cycle or less, crucial for swiftly correcting flickering voltage dips caused by arc furnace loads.
- In contrast to synchronous condensers, power capacitors do not contribute to the generation of short-circuit currents.
- A single installation can fulfill multiple functions, including reactive power compensation and power factor enhancement, thereby reducing TDD to acceptable levels.
- When choice is available between active and passive filters, the passive filters are more economical.

Limitations of Passive filter

- Passive filters are ill-suited for dynamic load system conditions, as they are fixed once installed. Adjusting the tuned frequency or size of the filter is not easily achievable. Moreover, the passive elements within the filter are precision components with close tolerances[31].
- Changes in system operating conditions may lead to some detuning, although filter designs should account for operation under varying loads and the utility's source impedance.

- System impedance significantly influences filter design. For the filter to be effective, its impedance must be lower than the system impedance, posing challenges in design, particularly for stiff systems.

- The outage of parallel branches can modify the resonant frequency, potentially leading to excessive stress on filter components and heightened harmonic distortion.

- Parallel resonance between the system and filter in single-tuned and double-tuned filters can amplify current at both characteristic and non-characteristic harmonics. Designers face constraints in selecting tuned frequencies and ensuring sufficient bandwidth between shifted frequencies and even and odd harmonics.

- Aging, deterioration, and temperature variations may lead to increased tolerances in the designed filters, potentially causing detuning. However, these effects can be accounted for during the design stage.

- special protective and monitoring devices are required.

- Design adjustments may necessitate enlarging the filters to manage Total Demand Distortion (TDD). However, this could lead to overvoltages when the banks are switched in and undervoltage when they are switched out.

- Detuning may occur when consumers connected to the same utility service integrate power capacitors or filters into their distribution systems.

1.6.2 Active compensation method

In contemporary contexts, harmonics and reactive power compensation have evolved into a new area of research. Given the limitations of passive filters and the escalating pollution of power systems, researchers have focused on the analysis, design, and advancement of active power filters (APF). These filters offer a dynamic and adaptable solution for harmonics elimination and reactive power compensation in three-phase, three-wire, and four-wire electrical distribution systems. Additionally, APFs can address power quality issues by selecting compensating power components. APFs, also known as Active Power Line Condensers (APLCs), Instantaneous Reactive Power Compensators (IRPCs), and Active Power Quality Conditioners (APQCs)[32], serve multiple functions beyond harmonics and reactive power compensation. They are adept at eliminating voltage harmonics, regulating terminal voltage to mitigate voltage flicker, and enhancing voltage balance in three-phase systems. Moreover, they excel in load balancing and neutral current compensation in three-phase, four-wire electrical distribution setups [33],[34],[35],[36],[37],[38]. With proper control algorithms, APFs have effectively addressed various power quality issues from consumer and utility-generated harmonics. Equipped with pulse width modulated (PWM) converters and capacitors or inductors on their DC side, APFs offer versatile solutions for active power injection and harmonic compensation.

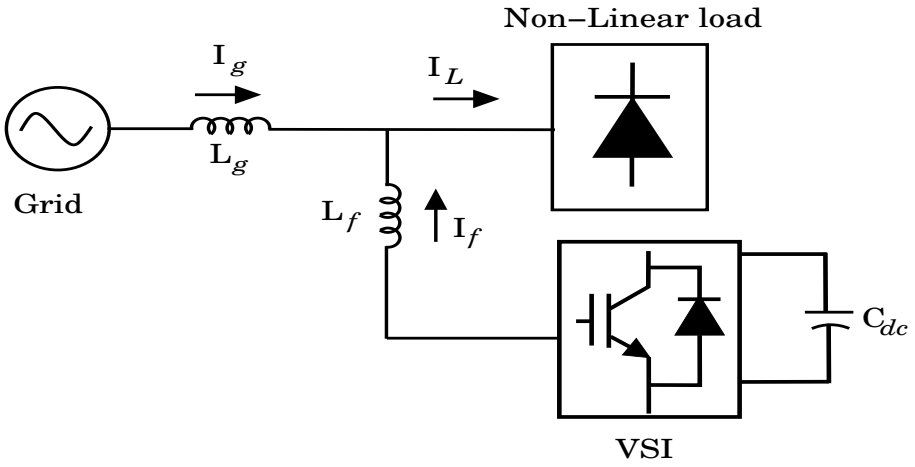

Figure 1.2: Configuration of Shunt active filter

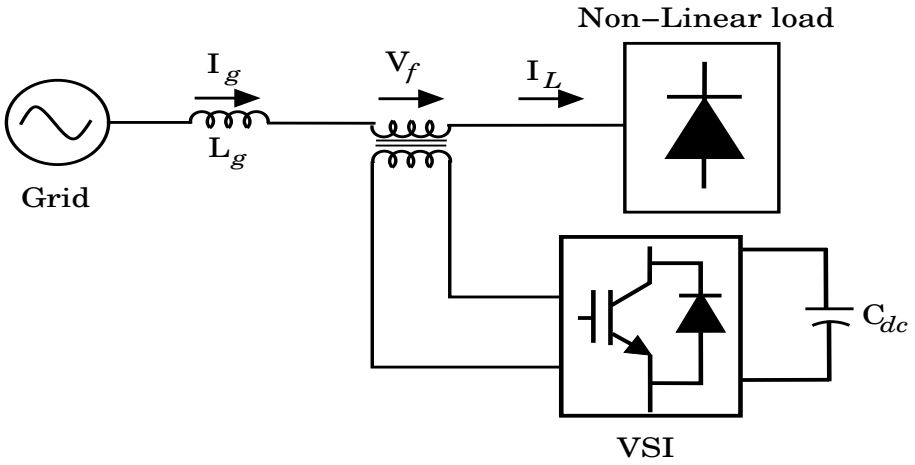

Figure 1.3: Configuration of Series active filter

The declining costs of power electronics components, significant advancements in capacity and switching speed, and the implementation of sophisticated control algorithms facilitated by fast digital signal processors (DSPs) have spurred new avenues of exploration in active filters. Furthermore, enhancements in sensor technology have played a pivotal role in augmenting the performance of APFs. Active filtering offers distinct advantages in both steady-state and dynamic load conditions. APFs effectively mitigate voltage and current harmonics and other power quality issues through meticulous control of PWM converter switches, ensuring a clean and stable supply system.

Various topologies have been developed so far based on compensation requirements, converter type, number of phases, etc. The APFs are broadly categorized as shunt, series, or a combination of shunt and series (Hybrid) based on circuit configurations [39], [40], [28], [41]. The appropriate topology can be selected based on the compensation requirement. In this thesis, investigations are confined to improving the power quality by compensating the nonlinear loads' current harmonics and reactive power requirements by shunt active power filter (SAPF).

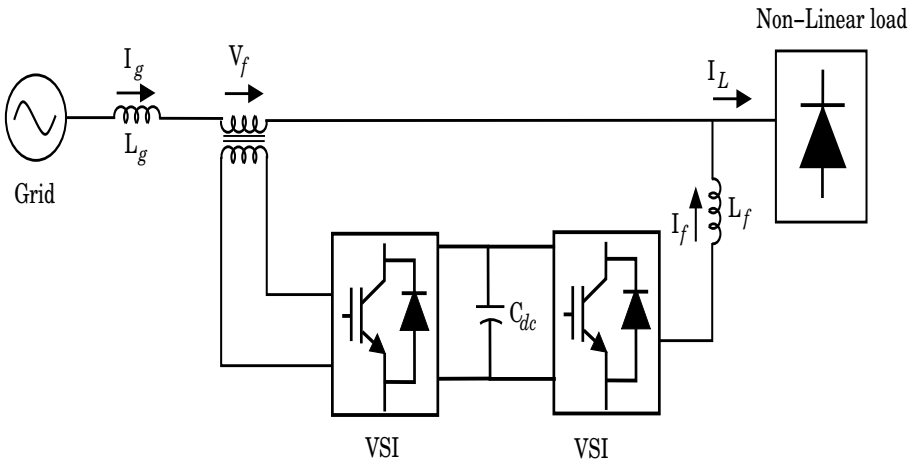

Figure 1.4: Configuration of hybrid active filter(Unified power quality compensator(UPQC))

1.7 Literature review

1.7.1 Power quality issues and harmonic and reactive power compensation methods with advanced control methods.

With the growing awareness of the implications of global warming, countries worldwide are actively pursuing strategic measures to curtail their greenhouse gas emissions[42]. A highly effective strategy involves integrating renewable energy sources like solar power into their energy grids [43], [44], [45], [46], [47]. However, the integration process faces significant technical challenges, including the intermittent nature of solar energy and fluctuations in industrial loads like drives and electric arcs. Additionally, it's essential to recognize that industrial loads can introduce disruptions into the power grid, such as injecting harmonics and oscillations, leading to issues like power quality and voltage instability [48], [49]. To overcome these challenges, it is crucial to develop power converters capable of efficiently injecting power into the grid, effectively managing disturbances, and ensuring compliance with IEEE standards[18] to maintain a specific level of grid quality Total Harmonic Distortion (%THD). Hence, past researchers [50], [51], [39], [35], [52], [53] have introduced passive and active power filters to regulate current harmonics and maintain them within acceptable limits. This approach significantly elevates the overall power supply quality. In the domain of passive filters, [50], [51], [39] have discussed the usage of traditional LC and LCL filters to address harmonic currents. These passive filters have a straightforward design and are cost-effective but bulky, heavy, and usually calibrated to address specific predominant harmonics[39]. Furthermore, their compensatory capacity is fixed and heavily dependent on the impedance of the connected electrical network, which may result in undesirable resonance problems[50]. On the other hand, within the active filter domain, shunt active filters (SAFs) are a well-established solution that has been extensively studied for mitigating predominant harmonics [39], [35], [52],[53],[54], [38]. However, designing SAFs necessitates a thorough evaluation of factors, including source

availability, converter topology, control methods, and output filters, to tackle harmonic issues efficiently [55]. These active filters are directly linked to the load or at the Point of Common Coupling (PCC). The design principles for SAFs focus on attaining a sinusoidal current pattern in the power grid by extracting information about load current harmonics to synthesize a reference signal for the controller [53]. These harmonics can be extracted in SAFs through various methods, including stationary reference frame techniques [56], [57], synchronous reference frame methods [58], [59], [60], or Fourier transform methods [61]. The effectiveness of SAF design through these extraction methods is optimized when the controller possesses sufficient bandwidth[62]. Inadequate controller bandwidth in SAFs can result in the undesirable introduction of notches in the injected grid current, further compromising the overall power quality of the grid, as highlighted in [63], [64]. Consequently, various controller models with diverse harmonic compensation capabilities have been investigated, as evidenced in references [65], [66], [67], [68], [69], [70], [71], [72], [73], [74], [75], [76], [77],[78].

However, existing control methods have overlooked the impact of the load's passive impedance and current gradients when formulating the passive filter and determining the controller's bandwidth [62] & [79]. Previous researchers have designed the passive filter with consideration for the current ripple in the output of the SAF, ensuring the provision of necessary load harmonics while simultaneously mitigating switching harmonics, as indicated in references [80], [81], [82]. To ensure the development of an accurate controller, it is imperative to take into account the load's passive impedance and the fluctuations in load current. In [63], the passive filter is specifically designed to efficiently eliminate switching harmonics while ensuring no impedance is added to the load-demanded harmonics. The given literature introduces a design approach that notably boosts the overall system bandwidth in comparison to conventional ripple-based filter designs. This thoughtful consideration allows for the choice of minimum inductor values, equipping the active filter to reduce harmonics and enhance the quality of the grid current. In addition to precise controller modeling, the controller's bandwidth is also influenced by the converter filter design of the SAF [80]. To enhance controller accuracy and broaden bandwidth, researchers also explored a range of nonlinear controller models with harmonic compensation capabilities [69], [70], [77], [79], [83], & [84]. However, the cross-coupling between active and reactive power with nonlinear wave shapes requires a comprehensive analysis to derive a suitable nonlinear tracking mechanism under varying loading conditions and active power injection. In addition, in a nonlinear controller, digital delays demand high bandwidth in digital circuitry, leading to persistent noise vulnerability. For precise controller development, it's essential to account for load and source impedance and instantaneous current variations [79]&[85]. This consideration enables the selection of minimal inductor values and optimal controller bandwidth, reducing harmonics and effectively enhancing grid current quality.

Thus far, the literature has predominantly focused on supplying load harmonics using SAF, with limited attention given to the simultaneous injection of active power alongside

harmonics supply[62]. As energy demands continue to rise, the need for solar interface active filters in nonlinear load infrastructures is growing[69]. These filters are expected to support active power injection into the grid while managing load-demanded harmonics. However, a notable challenge arises during active power injection due to the interaction between passive filter inductance and grid inductance. This interaction diminishes the short circuit ratio, leading to a weaker grid scenario [86]. This underscores the importance of designing the right passive filter and achieving the corresponding controller bandwidth to improve power quality in weak grid conditions. In [87], [88], [89], stability issues pertaining to weak grids are tackled by employing a synchronous reference frame-based model to depict the interactions between the grid and system impedance. The analysis reveals that modifying the bandwidth of the phase lock loop (PLL) notably impacts the system's capability to reject power harmonics[90]. However, it comes at the expense of compromising the dynamic response. Therefore, modifying the PLL bandwidth is not feasible as it restricts some load-demanded harmonics, leading to poor power quality, which contradicts the primary objective of SAF, which is to provide the harmonics demanded by the load[91]. Subsequent researchers have suggested virtual feed-forward loop compensation techniques to adjust the control loop parameters based on network impedance [90]. Nevertheless, these feed-forward loops introduce positive feedback, necessitating additional precautions to maintain system stability[86]. Later, researchers recommended the use of lead-lag compensators and notch filters specifically designed to mitigate power harmonics, ultimately enabling the delivery of high-quality power in weak grid scenarios. These techniques aim to enhance the quality of power supplied to weak grids but have restricted applicability since they primarily address frequency variations at the PCC. Furthermore, these methods frequently require additional sensors and complex algorithms. A recent study outlined in [86] demonstrated that properly tuning the gain of the PI controller could effectively reduce existing harmonics in weak grid scenarios. This reduction was achieved through precise modeling of the weak grid scenario, taking into account the interactions between system and network impedance [86]. However, it's important to note that these studies are solely focused on active power injection into the grid and do not address the supply of harmonics demanded by nonlinear loads.

1.7.2 Elevated DC bus voltage and circulating current issues of parallel and single inverter topologies.

In previous studies, researchers used single inverter topologies to handle the power harmonics of nonlinear load and active solar power injection characteristics. These studies found that the active filter circuits have limited capabilities in compensating for lower-order harmonics due to filtering and switching frequency limitations. Therefore, the modular inverter focuses on filter sizing and a dedicated control mechanism in multilevel, series, and parallel inverter configurations to reduce attenuation on lower-order harmonics and improve bandwidth compared to conventional topologies. Researchers have proposed control methods based on extracted harmonic information to address the neutral current

control [92]& [93], as well as reactive and harmonic power compensation [57],[94]&[95]. These methods are implemented on single-stage three-phase inverters in [58] & [73], multilevel inverters [92] & [53], [96], [97], [98]. In the multilevel inverter segment, flying capacitor SAPF[92], neutral point-clamped SAPFs [52] & [53], and cascaded H-bridge SAPFs [96], [97], [98] are proposed due to their superior output voltage quality and reduced power losses. However, the higher DC bus voltage rating of multilevel inverters can compromise circuit reliability, and the presence of multiple switches necessitates asynchronous switching, making control algorithms more complex. The parallel inverter configurations have been investigated for higher-power applications[99], [100], [101]. However, they are vulnerable to circulating currents and inherent DC-link voltage oscillations, requiring additional hardware circuitry or complex control mechanisms. The above literature mainly focuses on compensating harmonics through the capacitor by drawing active power from the grid in existing SAPFs. However, PV generators can eliminate the active power dependency on the grid. Surplus PV power can be injected into the grid using appropriate DC to AC converters.

In this direction, researchers have studied grid power injection characteristics of single-stage three-phase inverters [82] & [102], parallel inverters [103], [104],[105], and multilevel inverters [106], [107], [108]. Currently, modular inverters dominate the solar interface inverter portfolio, mostly parallel configurations. The modular single-stage parallel inverter is well known for sharing power in terms of current. In a parallel configuration, the DC bus voltage requirement to synthesize the desired AC voltage demanded to connect with the utility grid is high, typically 1000 V [109]. Along with elevated DC bus voltages, the parallel inverters also suffer from the need to operate the DC bus in floating conditions due to CMV in the inverter circuit. In parallel inverter topology, all modular inverters are assumed to have identical characteristic impedances and operate with the same switching instances to connect all inverter modules to the same DC bus. However, it is improbable that the modular inverters operating in parallel configuration have an identical characteristic impedance resulting in circulating current [110] & [111] within the inverter modules due to CMV. The past study shows that the DC bus's potentials affect the performance of the DC capacitors and the semiconductor switches. Researchers have proposed various methods to inject active power into the grid to reduce the DC link voltage requirements and the series inverter configurations demonstrated in work [47] & [112]. This topology can be further explored to deal with simultaneous harmonic support with harmonic suppression in a PV environment.

Apart from inverter topologies, it is necessary to concentrate on the passive filter design as it decides the system's dynamic response and the harmonics attenuation factor. In an ideal scenario, the filter should offer zero attenuation to load-demanded harmonics and infinite impedance to the switching frequency. However, in practice, keeping the switching frequency far from the load-demanded harmonics at minimum filter inductance is recommended to achieve minimal attenuation to the load harmonics. As in the conventional inverter, the limitations in elevating switching frequencies are due to higher

power loss, and device ratings demand a higher filter inductance for suppressing the switching harmonics[63] & [113]. The higher inductance is detrimental to power quality due to lower-order harmonic suppression. On the other hand, the LCL filters in SAPF configurations carry a high risk of oscillation with the load network due to internal resonance [114] & [115]. Thus, it is suggested to have an "L" filter with the minimum inductance value. In this context, the series inverter configuration can double the switching frequency across the load without increasing the actual switching of the inverter. Thus, it minimizes filter size and thereby improves the system bandwidth. In this work, the above-discussed problems are resolved by completing Chapter 2, Chapter 3, and Chapter 4.

1.8 Motivation

In pursuit of energy, requirements have been increasing steeply since 2011 with the increasing population. To meet the energy demand, the generation of power is increased. From Fig. 1.5, it is clearly visible that the primary energy consumption is closely followed by Coal, Oil, Natural gas, etc.[116], But, With the growing awareness of the implications of global warming, countries worldwide are actively pursuing strategic measures to curtail their greenhouse gas emissions[42]. A highly effective strategy involves integrating renewable energy sources, such as solar power, into their energy grids[44],[45],[46],[47]. From Fig. 1.6, it is clear that the renewable share in the electricity production of different countries worldwide. The renewable power share of India is only 20% of total power generation[117]. But, to meet the demand in India, renewable power generation increased from 2011 to 2020, as shown in Fig. 1.7

From Fig.1.7a and Fig.1.7b, it is evident that the nation is moving toward renewable energy generation, and preferably solar, due to its abundance and cleanness. On the other hand, the Government of India has launched many initiatives to promote clean energy generation, as listed in sub-section 1.8.1.

1.8.1 Government Initiatives to Promote Clean Energy Generation

To increase energy generation from renewable sources to meet the demand, India has unveiled its 2030 target. During COP26, India unveiled ambitious targets to decarbonize its energy sector by 50% and attain 500 GW of energy from renewable sources. To facilitate clean energy and promote the adoption of electric vehicles in the transportation sector, the Government of India has rolled out several schemes designed to incentivize and support these initiatives. The government schemes to promote the clean energy generation are listed below:

- **Solar park Scheme:** Intends to construct several solar parks, each with a capacity of nearly 500 MW.
- **Rooftop Solar Scheme:** Aims to harness solar power by installing solar panels on

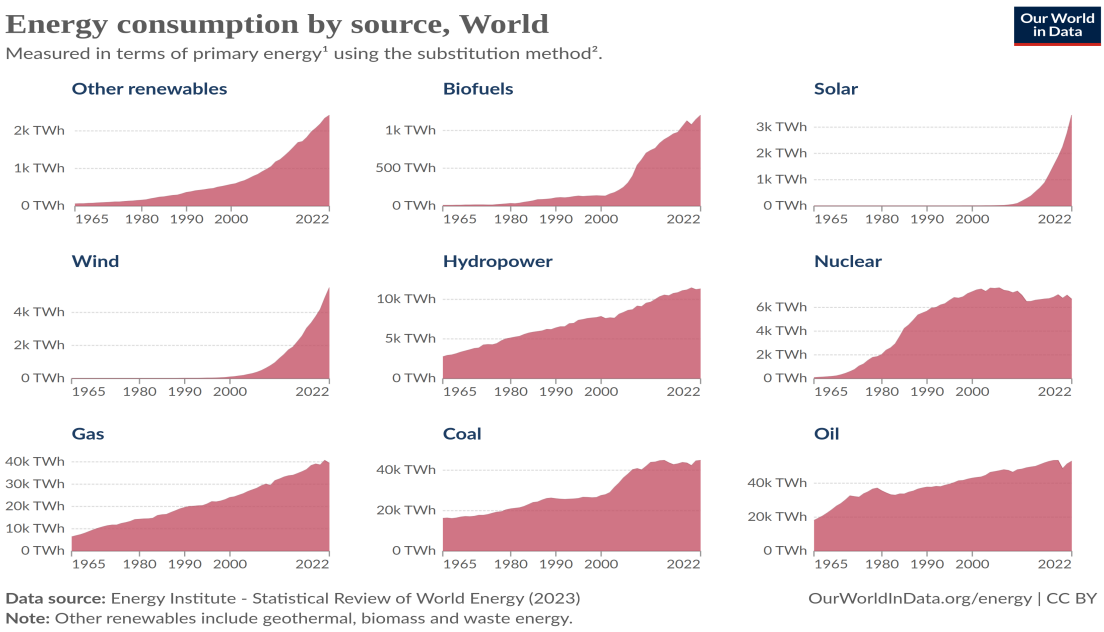

(a) Energy consumption by source in world

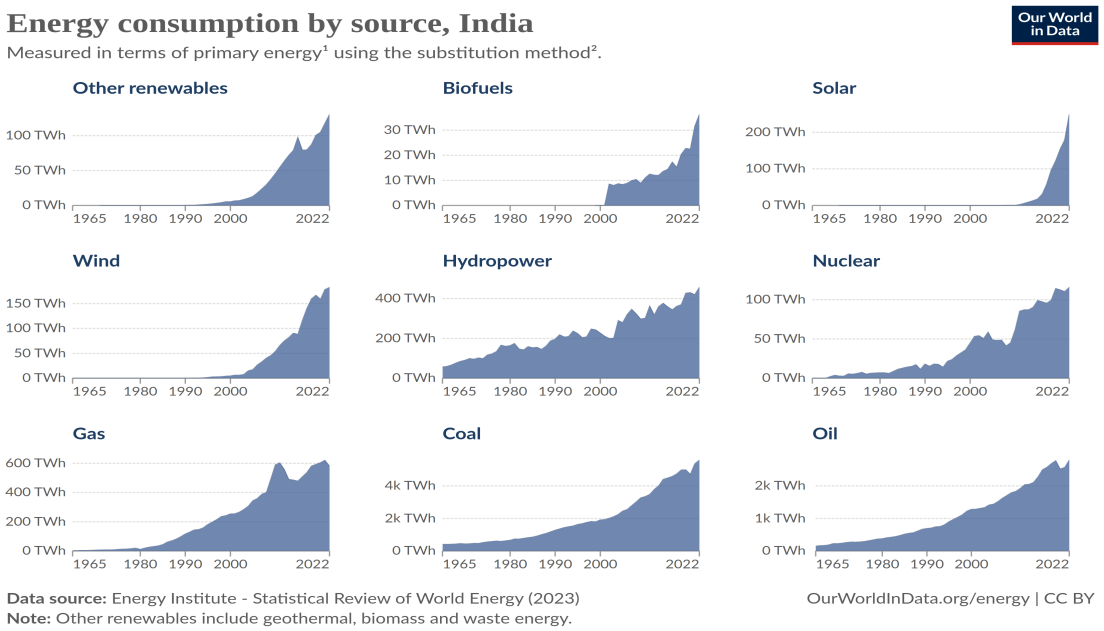

(b) Energy consumption by source in India

Figure 1.5: Energy consumption by sources

the roofs of houses.

- **SRISTI Scheme:** Sustainable Rooftop Implementation of Solar Transfiguration of India (SRISTI) scheme to promote or advance the rooftop solar projects in India.
- **International Solar Alliance:** It is a collaborative platform for increased deployment of solar energy technologies.
- **Kisan Urja Suraksha evam Utthaan Mahabhiyam (PM-KUSUM):**

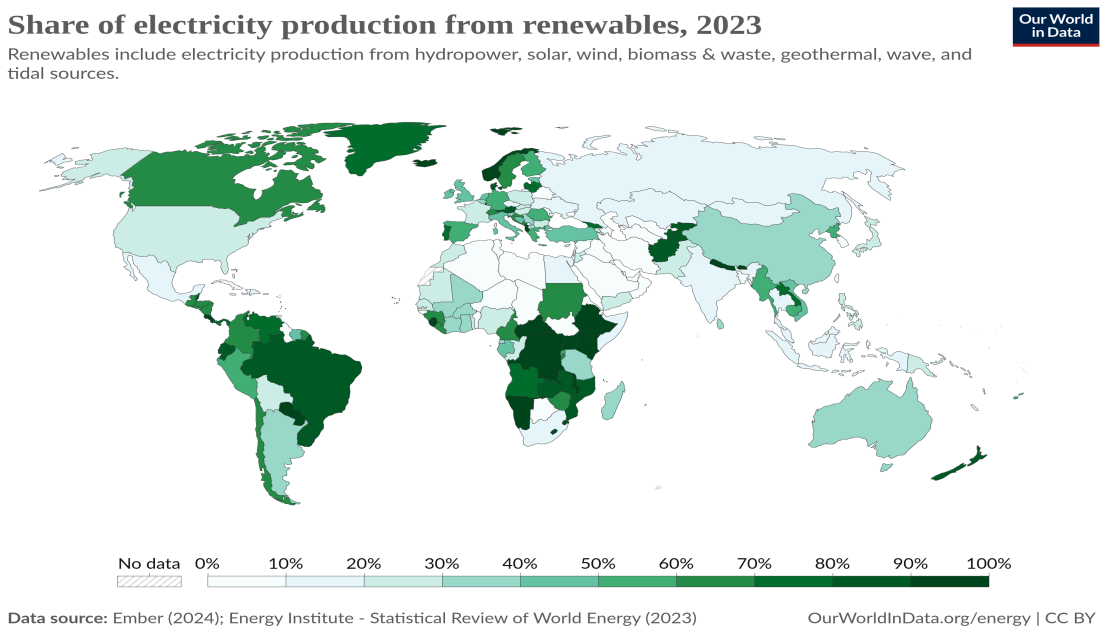

(a) Share of electricity production by renewables in world

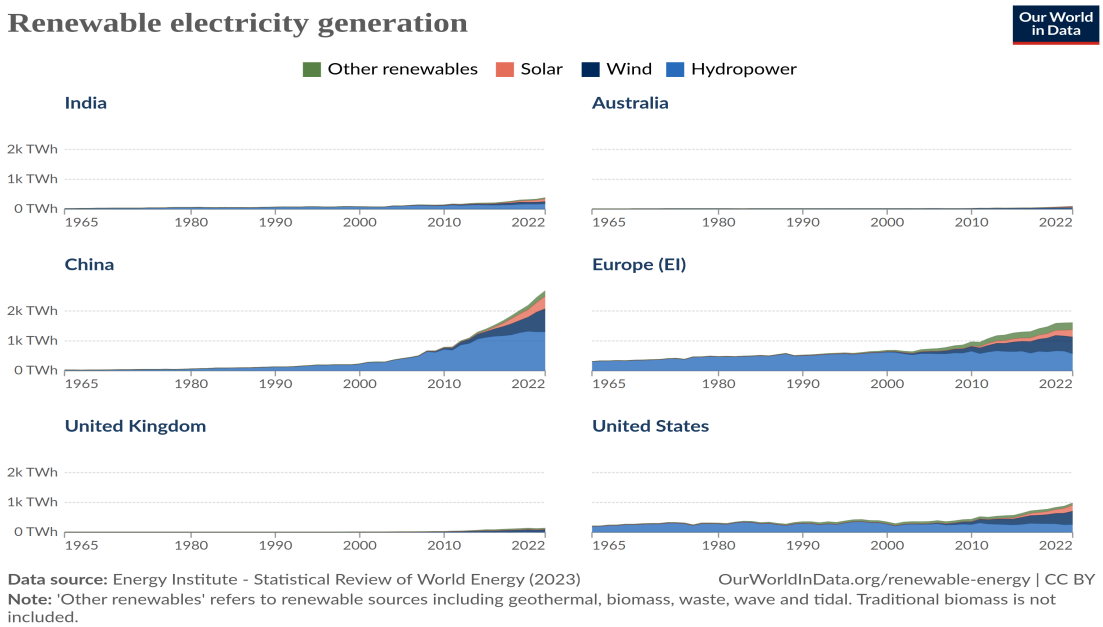

(b) Share of electricity production by with different renewables

Figure 1.6: Renewable electricity production share in different countries.

Launched by the Ministry of New and Renewable Energy (MNRE) to support the installation of off-grid solar pumps in rural areas and reduce dependence on the grid in grid-connected areas.

- **UDAN:** Airport runway lighting system, solar integrated technologies for railways, battery charging station

- **DDUGJY:** Rural electrification, Microgrid solutions

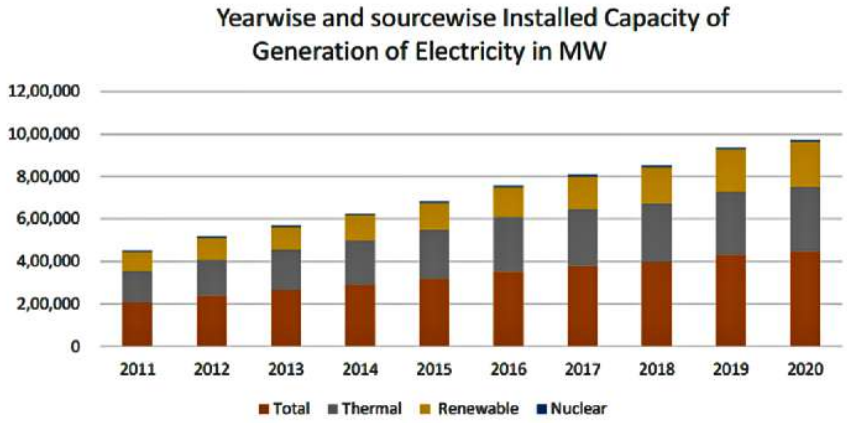

(a) Year-wise and source-wise installed capacity of electricity generation in MW (X-axis: Year; Y-axis: Electricity generation in MW)

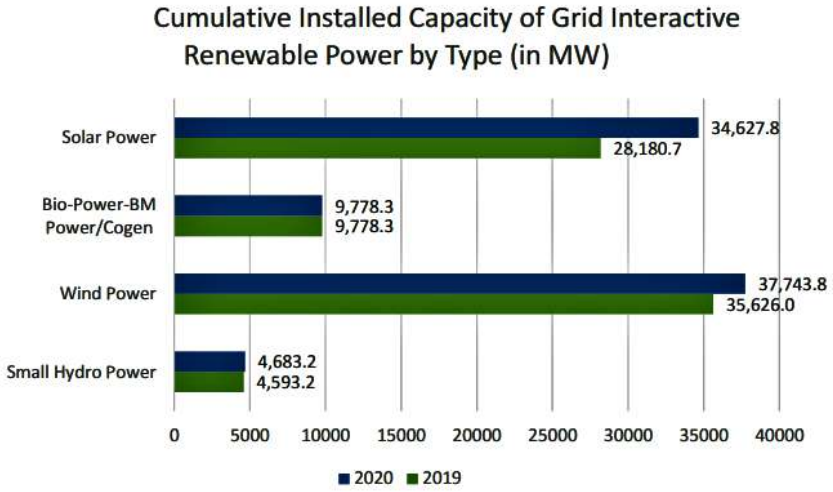

(b) Cumulative installed capacity of grid interactive renewable power by type (in MW) (X-axis: Year; Y-axis: Electricity generation in MW)

Figure 1.7: Cumulative installed capacity of grid interactive renewable power by type (in MW) (X-axis: Renewable sources; Y-axis: Energy generation in MW)

- **FAME:** Faster adoption and manufacturing of electric vehicles.

Moreover, as the population increases, so does the utilization of industries and smart technologies for enhanced convenience. Consequently, advancements in power electronic devices play a crucial role in simplifying human life and alleviating workloads. These devices are predominantly employed as load-side equipment to modulate power and voltage levels, drawing power from either the grid or renewable sources. However, the integration process encounters notable technical hurdles, including the intermittent nature of solar energy and fluctuations in industrial loads such as drives and electric arcs. It is imperative to acknowledge that industrial loads can introduce disturbances into the power grid, such as injecting harmonics and oscillations, thereby giving rise to issues such as power quality degradation and voltage instability. Consequently, an effective integration approach for solar energy with industrial nonlinear loads must account for dynamic variations in solar power and load harmonic profiles. Recent studies have revealed that active filter circuits

have limited capabilities in compensating for lower-order harmonics due to constraints related to filtering and switching frequencies. This gap presents challenges for filter sizing and necessitates a dedicated control mechanism in SAPF configurations to minimize attenuation on lower-order harmonics and enhance bandwidth.
Therefore, the government schemes to accelerate the integration of renewable energy with the grid by utilizing advanced grid-connected inverters and Active filter technologies to reduce the power quality problems in the grid. It enables the seamless transfer of renewable energy to the grid for powering nonlinear loads such as industries and electric vehicle charging systems. Therefore, these nonlinear problems, such as harmonics and reactive power requirements, can be compensated by using solar-interfaced grid-connected inverters, as discussed in the following chapters of the thesis.

1.9 Organization of Thesis

1. **Chapter 1:** includes an overview of the power quality, cause of power quality, and power quality problems. It also emphasizes the different harmonic sources and harmonic standards to maintain the power quality. Also possible solutions to power quality problems are also discussed from passive filters and active filters. This chapter gives a literature review of the recent technologies of active filters to eliminate the disadvantages of passive filters and discusses advanced control topologies for nonlinear control and series inverter topologies for the reduction of filter size, elevated DC bus potential, and circulating current within the inverter modules. Later, the motivation and objectives of the thesis are furnished, along with the organization of the thesis.

2. **Chapter 2:** deals with the involved dynamics necessitate that the solar interface front-end inverters be equipped to handle both harmonic distortions and active power injection characteristics simultaneously. In this chapter, an instantaneous load and source characteristic mapping is proposed for the solar-interfaced front-end inverter operated as a shunt active power filter cum active power injector in order to accommodate the dynamic variations of the source and load. As per requirement, to separate the load-demanded and switching harmonics, a new load network time constant-based passive filter design diverging from traditional passive filter design methods is demonstrated. Further, a comprehensive explanation of the current controller modeling methodology is elaborated, considering the essential bandwidth required for proficiently managing load-demanded harmonics in both grid injection and drawing modes of operation. Later, in grid injection mode, the influence of grid and system impedance interactions on the power quality is analyzed for weak grid scenarios to derive the requisite bandwidth conditions to ensure resilient power transfer.

3. **Chapter 3:** discusses and demonstrates an adaptive controller bandwidth

realization for a PV-interfaced front-end inverter (PIFI) delivering power to the EV charging station under random solar and nonlinear load variations. therefore, For an instantaneous adaptive bandwidth realization, a novel approach to model source intermittency and load nonlinearity in terms of angular frequencies is presented. With the dynamic source and load modeling, a method of rolling gain adjustment for the controller is demonstrated for adaptive accommodation of source and load characteristics. Thus, with the adaptive controller rolling gain adjustment, the PIFI can handle multiple functionalities of harmonic compensation, maximum power point tracking, and simultaneous active power injection.

4. **Chapter 4:** This chapter discusses a solar-based series inverter configuration to demonstrate the superior power quality shaping with the active power injection capability in grid-interfaced nonlinear load applications. The proposed configuration realizes the AC network in series. It ensures the reduced AC filter size and DC voltage compared to the conventional inverter topologies. The series inverter configuration mimics the double switching frequency across the load, making the system's overall bandwidth higher than the conventional inverter. The improved bandwidth ensures reduced attenuation towards lower-order load-demanded harmonics. Later in this chapter, the optimum filter size is derived by analyzing the nonlinear load current rise time signatures at different load resistances and filter inductances. With the appropriate filter sizing, the dynamic solar power and harmonic injection are accomplished by developing a dedicated closed-loop control mechanism for series inverters.

5. **Chapter 5:** presents the conclusion and future scope of the research work.

Chapter 2

Design and Implementation of Load Network Time Constant Computation Based Solar Active Power Filters Cum Injector for Industrial Loads/Grids

2.1 The Solar interfaced shunt active power filter

The schematic featured in Fig. 2.1 illustrates the Solar interfaced Shunt Active Power Filter (SiSAPF), a system thoughtfully designed to serve a dual purpose. It effectively addresses the harmonics demanded by the load while seamlessly integrating solar power into the AC network. The proposed system comprises a three-phase inverter integrated with solar panels, establishing a connection with the AC power network. This three-phase inverter is strategically positioned at the Point of Common Coupling (PCC), where it links the grid and nonlinear loads, as depicted in Fig. 2.1. A passive inductor, denoted as L_f, is connected to the inverter's output terminals. The primary function of this passive inductor is to mitigate switching harmonics while facilitating the passage of harmonics required by the load. The importance of filter inductance design lies in establishing an effective bandgap between these harmonics. This design aspect plays a crucial role in achieving the desired power quality in the grid. Therefore, in the upcoming sections, this paper delves into the meticulous process of designing an efficient passive filter using load network time constant computation, comparing it with conventional ripple-based filter design methods.

2.2 The proposed load network time constant computation based passive inductance design method

The design of passive inductance (L_f) ensures the optimal performance of SiSAPF in delivering load harmonics while attenuating the switching frequency component. The following section thoroughly elucidates a comprehensive method for determining the minimum and maximum inductance values.

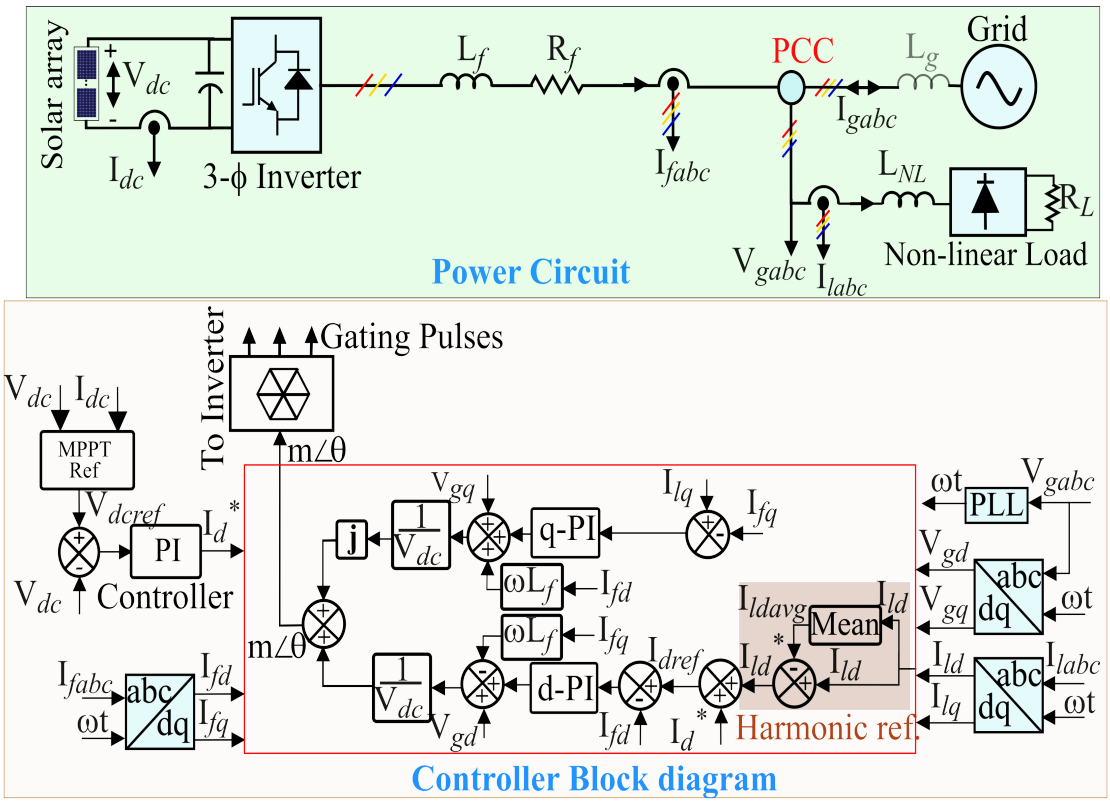

Figure 2.1: The solar interfaced shunt active power filter schematic with control diagram.

2.2.1 Minimum filter inductance design

To establish the minimum inductance value necessary for efficient harmonics management and the suppression of the switching frequency component, configure the three-phase inverter to solely supply active power to the load, which is represented by resistance $\mathbb{R}$ (where $\mathbb{R} = \frac{V_g}{I_g}$). This configuration is illustrated in the single-line diagram as shown in Fig. 2.2, facilitating the calculation of the required back electromotive force (emf) at the switching frequency across the passive inductance and resistance. The voltage across resistor $\mathbb{R}$, due to the switching frequency current, must match the emf produced by the inductor (e_{sw}), as depicted in Fig. 2.2. This relationship is expressed as:

$$e_{f_{sw}} = \mathbb{R} i_{fsw} = 2\pi f_{sw} L_{f_{min}} i_{fsw} \tag{2.1}$$

The information regarding the calculated back emf is pivotal in eliminating the current component generated by the switching frequency. Consequently, the minimum filter inductance can be determined using Equation. 4.7.

$$L_{f_{min}} = \frac{\mathbb{R}}{2\pi f_{sw}} \tag{2.2}$$

$$\mathbb{R} = 2 * \pi * f_{sw} * L_{f_{min}} \tag{2.3}$$

As shown in Fig. 2.2, the inductor produces varying back-emf across a range of

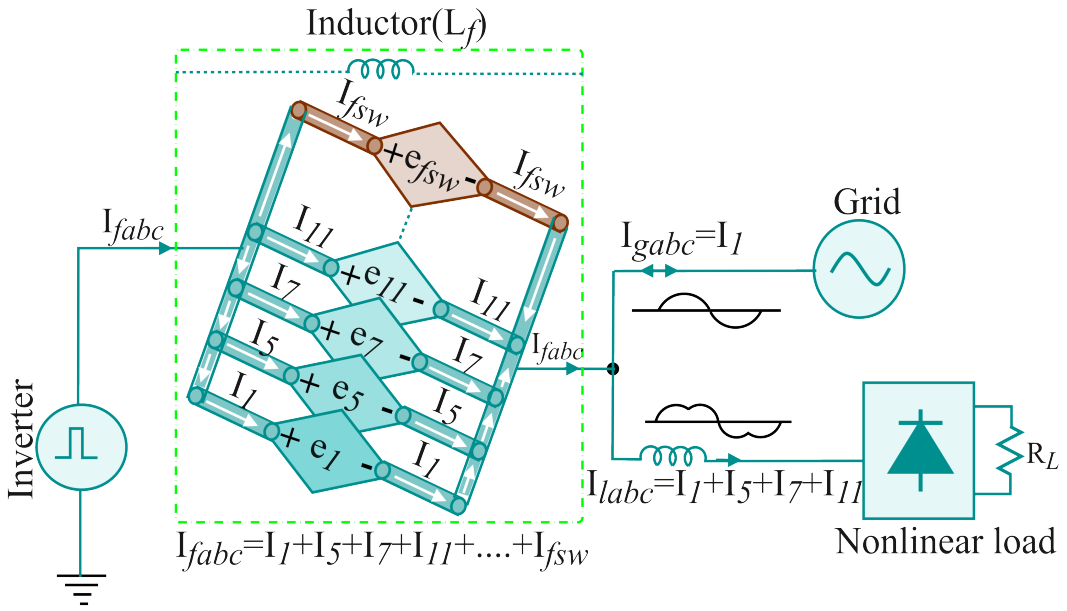

Figure 2.2: The SiSAPF's network single line diagram with the realization of filter inductance as a decomposed harmonic back-EMFs.

frequencies, spanning from the fundamental frequency to the switching frequency. To effectively accommodate the harmonics required by the load, it's crucial that $L_{f_{min}}$ does not contribute any back emf to these harmonics. The amplitude of the back emf imparted to each harmonic depends on the filter inductance and can be expressed as follows:

$$\begin{aligned} EMF_{inductor} &= e_1 + e_5 + e_7 + e_{11} + ... + e_{fsw} \\ &= i_1.\mathscr{R}_1 + i_5.\mathscr{R}_5 + i_7.\mathscr{R}_7 + i_{11}.\mathscr{R}_{11} + ... + i_{fsw}.\mathbb{R} \end{aligned} \tag{2.4}$$

The value of $(\mathscr{R}_1, \mathscr{R}_5, \mathscr{R}_7 ..... \mathbb{R})$ is obtained using Equ.(2.3).

$$\mathscr{R}_1 = 2.\pi f_1 L_{f_{min}};\ \mathscr{R}_5 = 2.\pi f_5 L_{f_{min}} ... \tag{2.5}$$

In this context, the impedance's $\mathscr{R}_1, \mathscr{R}_5, \mathscr{R}_7$, and so on are frequency-dependent, varying in magnitude relative to multiples of the fundamental frequency. This change is visually represented in the top trace of Fig. 2.3, using yellow and green colors to differentiate between two distinct switching frequencies, namely, f_{sw1} and f_{sw2}. As the inverter's operational switching frequency transitions from f_{sw1} to f_{sw2}, the computed impedance values, in accordance with Equation(2.5), diminish. This leads to reduced impedances, depicted in green, for individual current harmonics, indicated in violet, as observed in the top trace of Fig. 2.3. Moreover, the corresponding back emf for individual current harmonics at these two unique operational switching frequencies, f_{sw1} and f_{sw2}, is visualized in the bottom trace of Fig. 2.3. Evidently, the provided back emf consistently registers a slightly lower value, approximately 0.1 to 0.3 per unit (PU), compared to the back emf at the switching frequency. This observation underlines the significance of maintaining minimal back emf for the harmonics required by the load, ensuring that

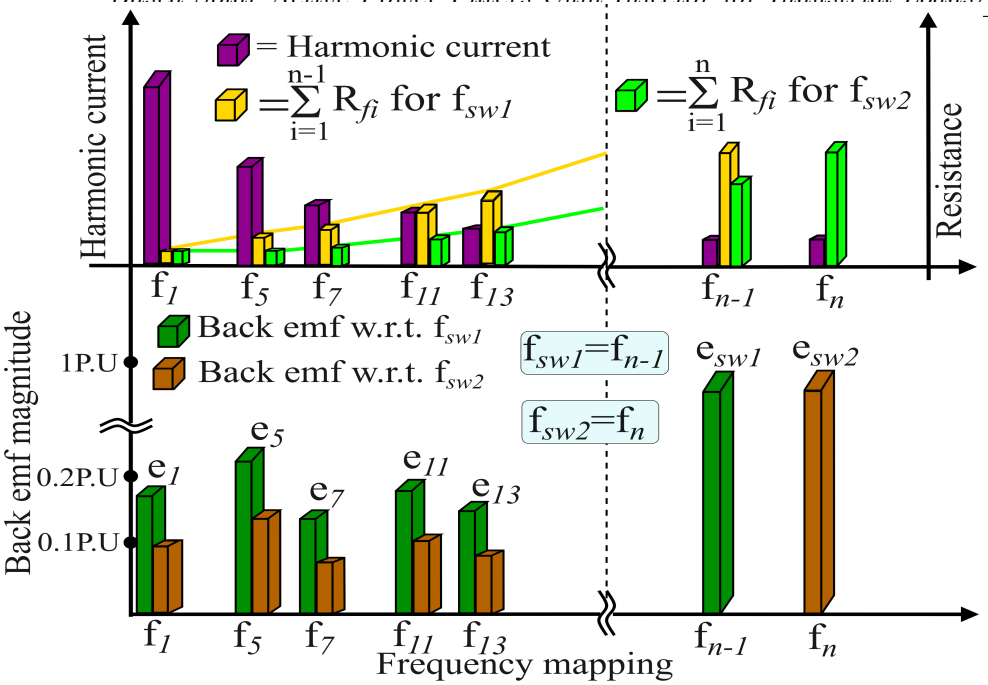

Figure 2.3: The variation of the current harmonics along with the offered resistance and corresponding back emf offered by the filter inductor (L_f) at two frequencies f_{sw1} and f_{sw2}.

the designed minimum passive filter inductance is capable of delivering these harmonics without attenuation. Simultaneously, the calculated inductance value defines the time constant of the SiSAPF system as follows:

$$\tau_{sys} = \frac{L_{f_{min}}}{\mathbb{R}} \tag{2.6}$$

2.2.2 Maximum filter inductance design

To establish the maximum inductance value, it's crucial to evaluate the required bandwidth by taking into account the load network time constant. This time constant is dependent on factors such as the load network's per-phase equivalent resistance (R_{NL}) and inductance (L_{NL}), as visually represented in Fig. 2.4. The load network time constant (τ_n) is defined as follows

$$\tau_n = \frac{L_{NL}}{R_{NL}} \tag{2.7}$$

Where the method for obtaining the R_{NL} value is detailed in the appendix.
The connection between the load network time constant and the rate of load current rise is defined by Equ.(2.8).

$$2\pi f_{BW} = \frac{1}{\tau_r} = \frac{1}{2.197\tau_n} \tag{2.8}$$

This relationship shows that the per-phase load current rise time is approximately 2.197 times the load network time constant (τ_n). Additionally, it is evident from Fig. 2.4 that a reduction in filter inductance results in a shorter rise time for the load current while the load power remains constant. The understanding of a shorter rise time plays a pivotal role in the design of a SiSAPF passive filter, aimed at achieving a broader bandwidth than

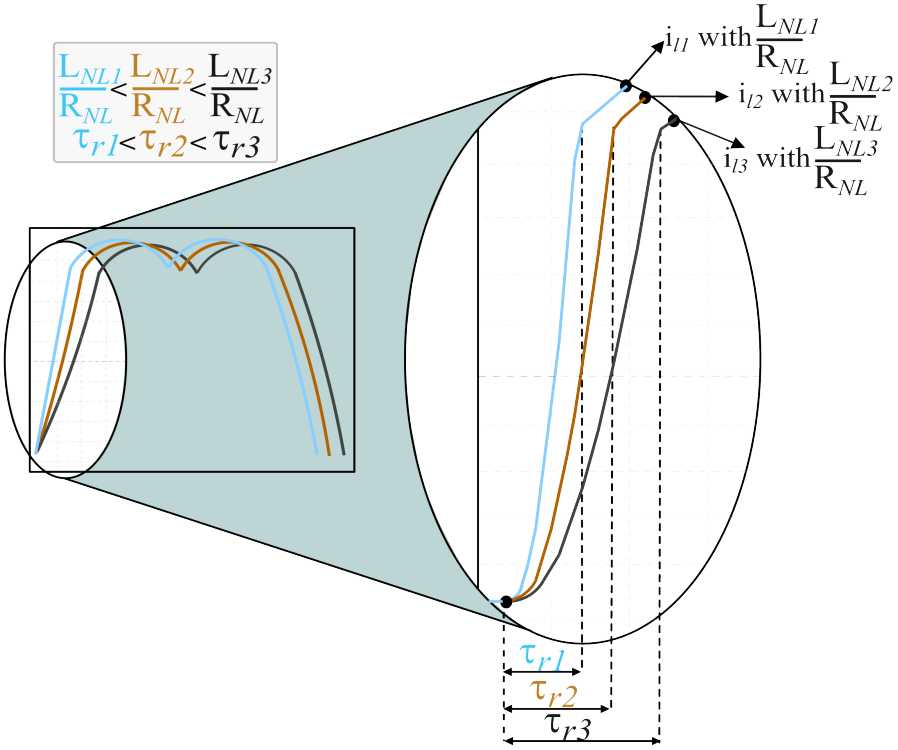

Figure 2.4: The non-linear load current profile with change in network inductance L_{NL}.

the load network. This objective is attained through a systematic design approach for the passive filter, with a particular emphasis on the load network time constant (τ_n) and the SiSAPF system time constant (τ_{sys}) as essential parameters. To effectively manage the complete spectrum of load-demanded harmonics without any reduction, it is crucial to guarantee that the SiSAPF system time constant (τ_{sys}) remains shorter than the load network time constant (τ_n). Consequently, the maximum values for the filter inductance can be determined based on the network time constant, and these values are as follows:

$$L_{f_{max}} = \tau_n.\mathbb{R} \tag{2.9}$$

The filter specifications, determined through Equation(2.9) for different load processing powers, are compared with traditional ripple-based filter design methods [63], as depicted in Fig. 2.5. It becomes evident that the innovative filter design effectively accommodates the load-demanded harmonics, ensuring a flawless sinusoidal grid current, unlike the conventional filter design methods. Conventional filter design methods take into account the inverter switching frequency and the magnitude of current ripple when designing

passive filters for SAFs as depicted in Equation(2.10).

$$
\begin{aligned}
L_f &= \frac{V_{dc}}{6F_{sw}\triangle I_{pp_{max}}} \quad Method-1 \\
L_f &= \frac{V_{dc}}{2\sqrt{6}F_{sw}\triangle I_{pp_{max}}} \quad Method-2 \\
L_f &= \frac{V_{dc}}{8F_{sw}\triangle I_{pp_{max}}} \quad Method-3 \\
L_f &= \frac{m_a V_{dc}}{12F_{sw}\triangle I_{pp_{max}}} \quad Method-4
\end{aligned} \tag{2.10}
$$

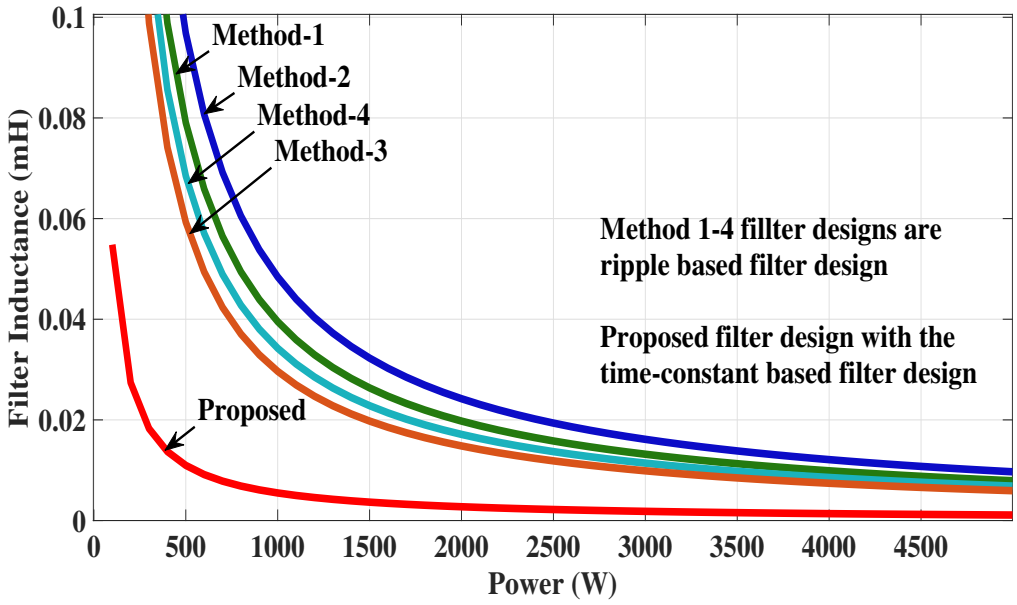

Figure 2.5: comparison of filter design methods at different powers.

It is worth noting that the conventional approach results in larger filter inductance sizes, as shown in Fig. 2.5, and fails to provide adequate bandwidth for the load-demanded harmonics. This leads to the introduction of unwanted notches in the grid current and, consequently, a degradation in the overall power quality of the grid, as displayed in Fig. 2.6. This is because these methods often overlook the impact of load passive impedance and variations in load current gradients when determining the passive filter inductance value.

Finally, taking into account the essential bandwidth and switching frequency attenuation criteria, the permissible range of filter inductance can be determined based on:

$$
\frac{\mathbb{R}}{2\pi f_{sw}} \leq L_f \leq \tau_n \mathbb{R} \tag{2.11}
$$

Following the modeling of filter inductance, it is essential to employ closed-loop modeling to enhance further the performance of the proposed SiSAPF system in delivering active power while managing load-demanded harmonics. This modeling approach aids in determining the appropriate controller gains for achieving the desired dynamic response and optimizing

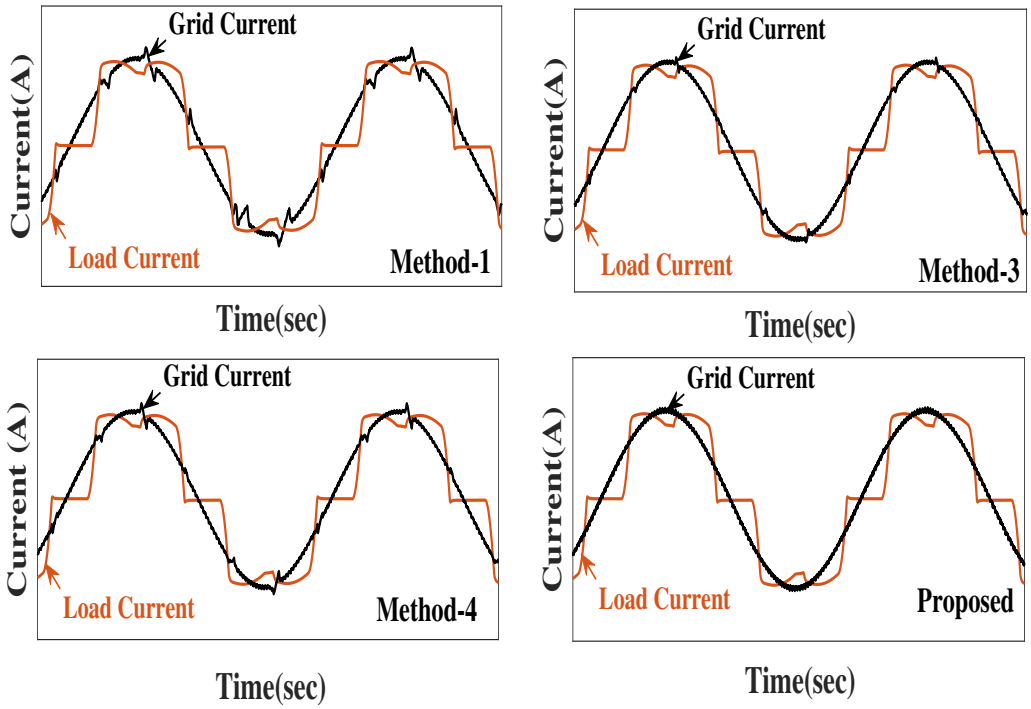

Figure 2.6: comparison of grid currents for the load currents at different filter design methods.

the overall system bandwidth. Further insights on closed-loop modeling are provided in the following section.

2.3 The SiSAPF's closed-loop controller modeling

This section focuses on the closed-loop controller modeling based on the synchronous reference frame (SRF). The objective is to attain the desired dynamic responses while managing load-demanded harmonics. In the SRF approach, the three-phase grid voltages are sensed at the Point of Common Coupling (PCC) to derive the synchronous voltage references (v_{gd} & v_{gq}).

$$v_{gd} = \frac{2}{3}(v_{ga}cos(\omega t) + v_{gb}cos(\omega t - 120^o) + v_{gc}cos(\omega t + 120^o)); \quad (2.12)$$

$$v_{gq} = \frac{-2}{3}(v_{ga}sin(\omega t) + v_{gb}sin(\omega t - 120^o) + v_{gc}sin(\omega t + 120^o)); \quad (2.13)$$

Here, ωt represents the grid voltage angle obtained through a phase-locked loop (PLL). Subsequently, the three-phase nonlinear load currents (I_{la}, I_{lb}, and I_{lc}) are converted into a synchronous reference frame by employing the acquired grid voltage angle (ωt), as outlined below:

$$
\begin{aligned}
I_{ld} &= \frac{2}{3}(I_{la}cos(\omega t) + I_{lb}cos(\omega t - 120^o) \\
&\quad + I_{lc}cos(\omega t + 120^o)); \\
I_{lq} &= \frac{-2}{3}(I_{la}sin(\omega t) + I_{lb}sin(\omega t - 120^o) \\
&\quad + I_{lc}sin(\omega t + 120^o));
\end{aligned} \tag{2.14}
$$

In this context, I_{la}, I_{lb} and I_{lc} represent the three-phase nonlinear load currents sensed before the diode bridge rectifier, as depicted in Fig. 2.1, and are subsequently converted to the synchronous reference frame as I_{ld} and I_{lq}. The load harmonics component information is then extracted by subtracting the fundamental component from the real component of the nonlinear load current, as outlined in Equation(2.15)

$$
\begin{bmatrix} I_{ldh} \\ I_{lqh} \end{bmatrix} = \begin{bmatrix} I_{ld} - Avg(I_{ld}) \\ I_{lq} \end{bmatrix} \tag{2.15}
$$

Subsequently, the reference for the current controller can be determined by combining the extracted load harmonics component with the photovoltaic active power component, as shown below:

$$
\begin{bmatrix} I_{dref} \\ I_{qref} \end{bmatrix} = \begin{bmatrix} I_{ldh} + I_d^* \\ I_{lqh} \end{bmatrix} \tag{2.16}
$$

Where I_d^* represents the active power reference generated by the Maximum Power Point

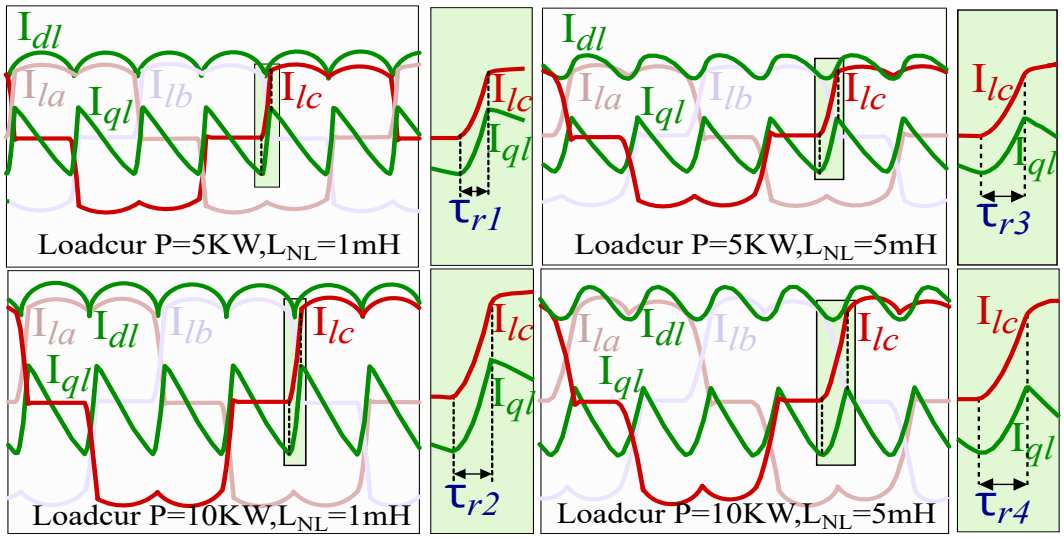

Figure 2.7: The variation of three phase nonlinear load currents and corresponding real and reactive component (I_{dref} and I_{qref}) profiles in SRF at different filter inductance and network power.

Tracking (MPPT) controller, as shown in Fig. 2.1. Moreover, Fig. 2.7 illustrates the typical variations of I_{ld} and I_{lq}. It's noteworthy that the rise time of I_{lq} precisely aligns with the load current rise time (τ_r), indicating that the load network's time constant (τ_n) information is inherently embedded in I_{qref}. Consequently, I_{qref} data alone is sufficient for determining the network time constant required to design the SiSAPF inductance and the

associated closed-loop controller gains. Furthermore, the derived active power reference (I_{dref}) integrates the available photovoltaic active power with the load harmonics demand, allowing the SiSAPF network to operate in two modes based on available solar active power.

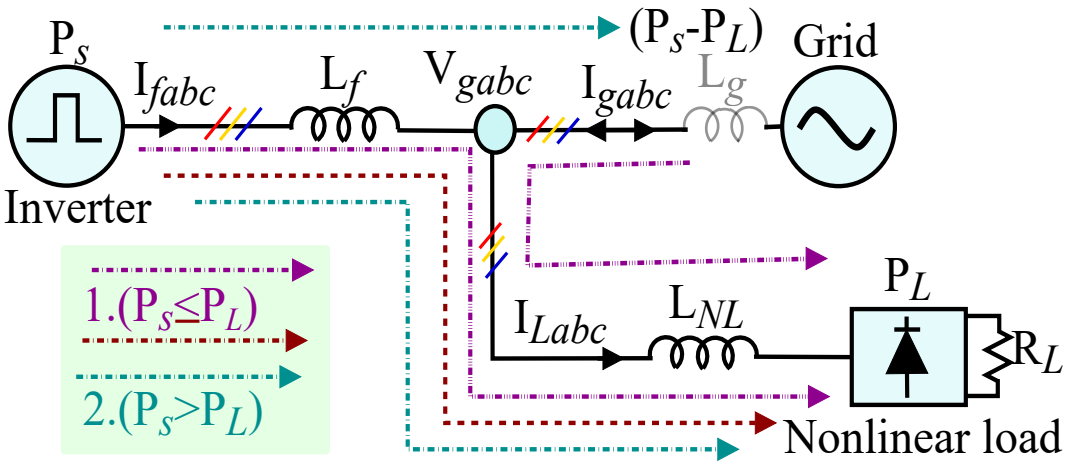

Figure 2.8: The single line diagram of the power network demonstrates the power interaction between SiSAPF, grid, and nonlinear load.

1. Mode-1 (Grid drawing power mode): When the available solar active power (PS) is less than or equal to the load demanded active power (P_L), i.e. ($P_S <= P_L$), the active power drawn from the grid can be calculated as P_{gd}=P_L-P_S.

2. Mode-2 (Grid Injection power mode): $P_S > P_L \implies$, the active power injected to the grid can be calculated as P_{gi} =P_S-P_L;

The controller gain modeling for mode-1 and mode-2 is described in the subsequent subsection by monitoring the power and its associated time constant.

2.3.1 Mode-1 operation

During this mode of operation, the equivalent resistance (R_s) corresponding to the available solar energy processed by SiSAPF can be identified as:

$$R_s = \frac{v_{gd}}{I_{fd}} \tag{2.17}$$

Here, v_{gd} represents the grid voltage, and I_{fd} is the grid-injected current in the d-domain. By utilizing the identified resistance (R_s) and system inductance (L_f), the system's transfer function can be obtained by identifying the rate of change in reference current as

follows:

$$\frac{dI_{dref}}{dt} = \frac{2}{3}((\frac{v_{ga}}{L_f} - \frac{R_s}{L_f}i_{fa})cos(\omega t) + (\frac{v_{gb}}{L_f} - \frac{R_s}{L_f}i_{fb})$$
$$cos(\omega t - 120) + (\frac{v_{gc}}{L_f} - \frac{R_s}{L_f}i_{fc})cos(\omega t + 120)) + \omega I_{qref}$$
$$\frac{dI_{qref}}{dt} = \frac{-2}{3}((\frac{v_{ga}}{L_f} - \frac{R_s}{L_f}i_{fa})sin(\omega t) + (\frac{v_{gb}}{L_f} - \frac{R_s}{L_f}i_{fb})$$
$$sin(\omega t - 120) + (\frac{v_{gc}}{L_f} - \frac{R_s}{L_f}i_{fc})sin(\omega t + 120)) - \omega I_{dref} \quad (2.18)$$

Here, i_{fa}, i_{fb}, and i_{fc} represent the SiSAPF three-phase currents, while v_{ga}, v_{gb}, and v_{gc} denote grid voltages, as illustrated in Figure 1. Substituting (2.12) and (2.13) into Equation (2.18) yields:

$$\frac{dI_{dref}}{dt} = \frac{v_{gd}}{L_f} - \frac{R_s}{L_f}I_{dref} + \omega.I_{qref} \quad (2.19)$$
$$\frac{dI_{qref}}{dt} = \frac{v_{gq}}{L_f} - \frac{R_s}{L_f}I_{qref} - \omega.I_{dref} \quad (2.20)$$

The derived (2.19) and (2.20) can be expressed in the form of state space model as $\dot{x} = Ax + Bu$ and $y = Cx + Du$:

$$\begin{bmatrix} \frac{dI_{dref}}{dt} \\ \frac{dI_{qref}}{dt} \end{bmatrix} = \begin{bmatrix} \frac{-R_S}{L_f} & \omega \\ -\omega & \frac{-R_S}{L_f} \end{bmatrix} \begin{bmatrix} I_{dref} \\ I_{qref} \end{bmatrix} + \begin{bmatrix} \frac{V_{dc}}{L_f} & 0 \\ 0 & \frac{V_{dc}}{L_f} \end{bmatrix} \begin{bmatrix} m_d \\ m_q \end{bmatrix} \quad (2.21)$$

$$\begin{bmatrix} I_{fd} \\ I_{fq} \end{bmatrix} = \begin{bmatrix} 1 & 0 \\ 0 & 1 \end{bmatrix} \begin{bmatrix} I_{dref} \\ I_{qref} \end{bmatrix} \quad (2.22)$$

Where,$V_{gd} = m_d * V_{dc}$ and $V_{gq} = m_q * V_{dc}$.
Furthermore, the transfer function can be derived from the state-space equation in the following form:$[Y(s) = (C(SI - A)^{-1}B + D)$

$$\begin{bmatrix} I_{fd} \\ I_{fq} \end{bmatrix} = \begin{bmatrix} G_{11} & G_{12} \\ G_{21} & G_{22} \end{bmatrix} \begin{bmatrix} m_d \\ m_q \end{bmatrix} \quad (2.23)$$

The derived G_{11} and G_{22} represents the $d-$ loop and $q-$ loop plant transfer functions as shown in Fig.2.9.

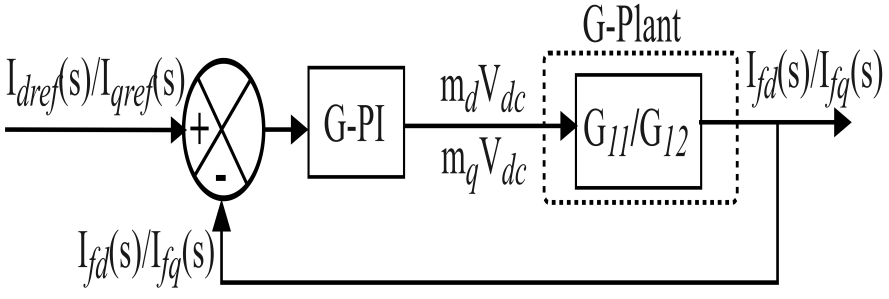

Figure 2.9: The signal flow diagram consolidated the plant model and controller.

The plant transfer function is described as

$$G_{11} = G_{22} = \frac{(sL_f + R_S)}{s^2L_f^2 + 2L_fR_Ss + R_S^2 + \underbrace{(\omega L_f)^2}_{\approx 0}} \tag{2.24}$$

Here, ωL_f represents the cross-coupling term. As this coupling term is compensated in the feed-forward loop, as shown in Figure 2.1, the plant's transfer function can be simplified as:

$$G_{11} = G_{22} = \frac{1}{(sL_f + R_S)} \tag{2.25}$$

As demonstrated in Equation (2.25), the value of L_f determines the open-loop response of the plant. The Bode plot of the plant, with L_f calculated using both the conventional ripple-based method and the proposed time constant-based method, is shown in Fig. 2.10. From the Bode plot and root locus plot in Fig. 2.10, it is evident that the inductance computed using the method described in this work provides a wider bandwidth compared to the ripple-based filter design method.

Later, in order to analyze the system's dynamic response effectively, it is essential to determine the closed-loop transfer function. Initially, the open-loop transfer function of the plant is established by combining the transfer functions of the PI controller and the plant, as shown below:

$$G_{PI} = K_P + \frac{K_I}{s}; \quad G_{open} = G_{PI} * G_{plant} \tag{2.26}$$

$$G_{open} = \frac{K_P}{sL_f}.(s + \frac{K_I}{K_P}).(\frac{1}{s + \frac{R_S}{L_f}}) \tag{2.27}$$

Furthermore, the closed-loop transfer function can be expressed as follows:

$$G_{closed} = \frac{G_{open}}{1 + G_{open}} \tag{2.28}$$

Using the closed-loop transfer function, the controller gains can be determined as follows:

$$K_P = \frac{L_f}{\tau_s}; K_I = \frac{R_S}{L_f}.K_P; \tau_s = \frac{L_f}{K_P} \tag{2.29}$$

As per Equation (2.29), it is evident that the value of K_P at a given L_f determines the system's dynamic response. The step response of the closed-loop system at different K_P values is depicted in Fig. 2.11. It is clear from Fig. 2.11 that an increase in K_P leads to an improved dynamic response as the system time constant (τ_s) decreases. Therefore, selecting a suitable K_P value that satisfies $\tau_s \leq \tau_n$ is essential to smoothly process the load-demanded harmonics along with active power injection into the power network. However, increasing gain values cause the controller's zeros to shift towards the right-hand side of the complex plane, as shown in Fig. 2.12. Fig. 2.12 makes it evident that the

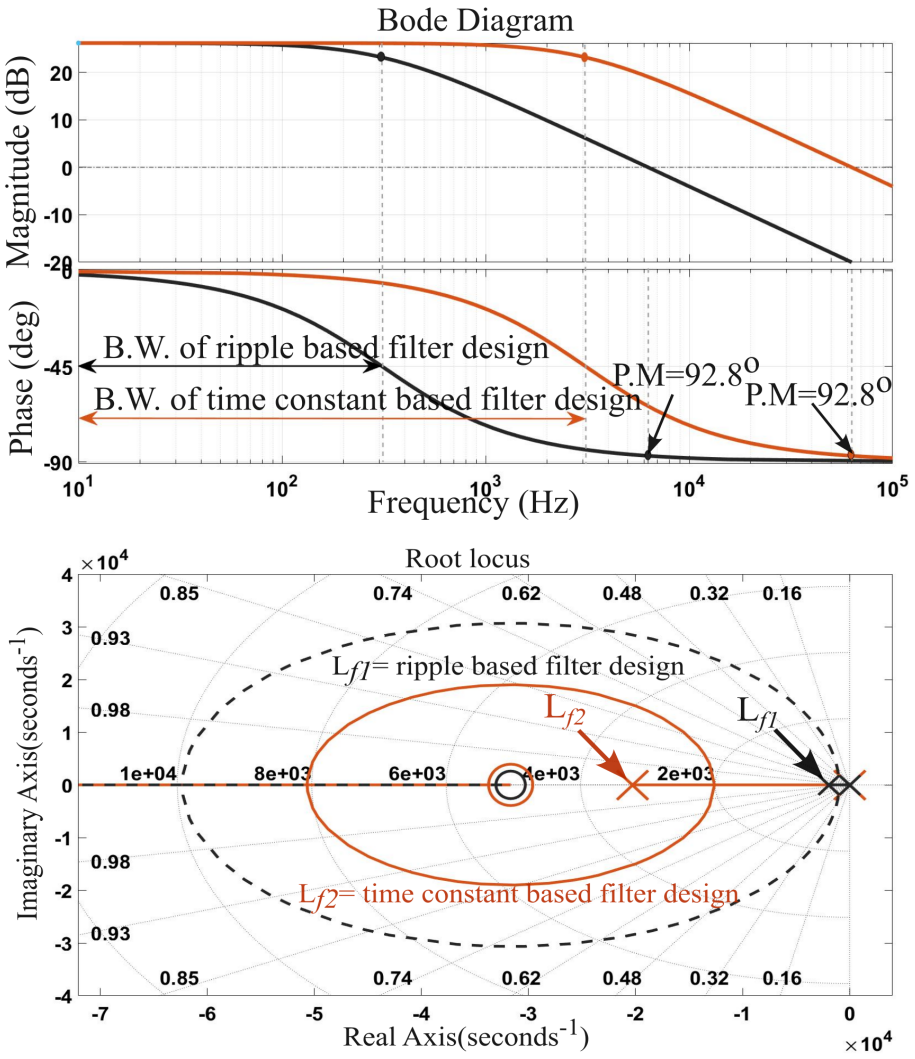

Figure 2.10: The Bode diagram and Root locus of SiSAPF's open-loop transfer function with the variation of the filter inductance.

controller zeros are moving towards an unstable region. Hence, choosing controller gains within acceptable limits is crucial to ensure stable system operation. The effect of the controller gains on grid current in terms of % THD for processing the inverter power into the grid and load is discussed in the following section.

2.3.2 The selection of controller gains based on load network time constant

Further, in this subsection, the controller gains selection based on the determined load network time constant for accomplishing the maximum possible closed-loop bandwidth is demonstrated. Here, the boundary of controller gains and outlines selection criteria based on the network time constant is elaborated. The controller system time constant is strategically chosen relative to load power and network impedance, ensuring it remains lower than the load network time constant ($\tau_s \leq \tau_n$). Under these conditions, a comparative analysis of the proposed and ripple-based filter designs is conducted across

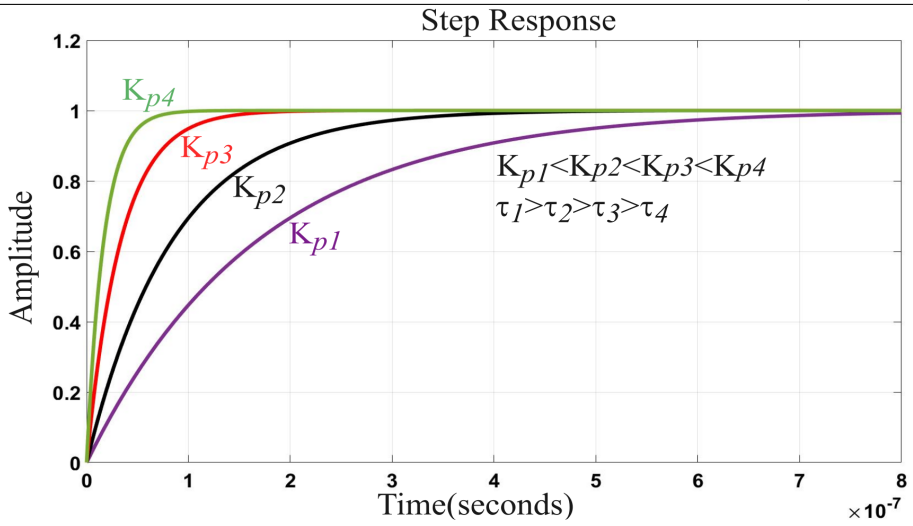

Figure 2.11: Step response SiSAPF's closed-loop transfer function with varying K_p.

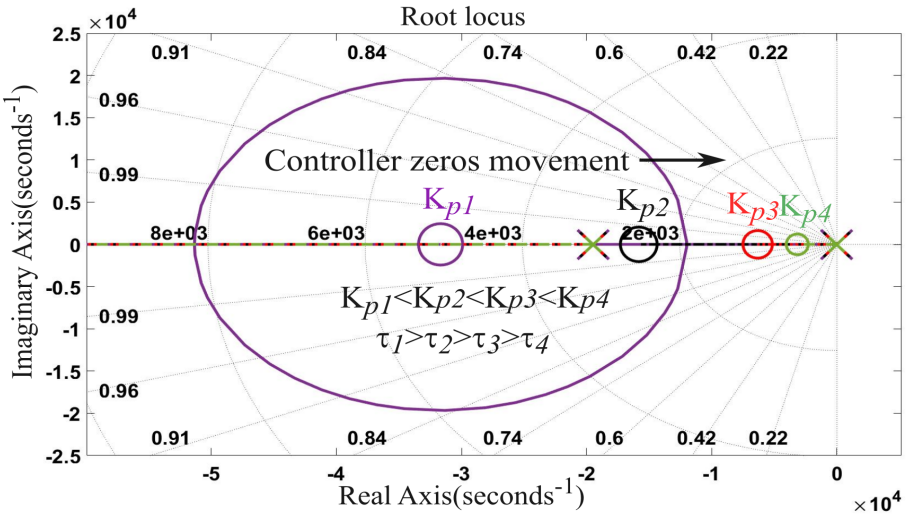

Figure 2.12: Root locus of SiSAPF's open-loop transfer function with varying K_p.

varying power levels, with %THD comparisons presented in Fig. 2.13. The validity of this condition is confirmed in both grid drawing and injected modes, particularly under stiff grid conditions. Fig. 2.13a illustrates the efficacy of harmonic compensation with the proposed filter inductance compared to diverse ripple-based filter inductance methods in grid drawing (left) and grid injected (right) modes. Additionally, Fig. 2.13b compares the proposed method under different controller system time constants. This reveals that a time constant lower than the network time constant yields superior harmonic compensation and lower grid current %THD. However, in grid injection mode, depending upon the injected power, the uncompensated grid inductance contributes to grid current oscillations, diminishing the grid's power quality. Strategies for enhancing grid power quality are discussed in the subsequent sections.

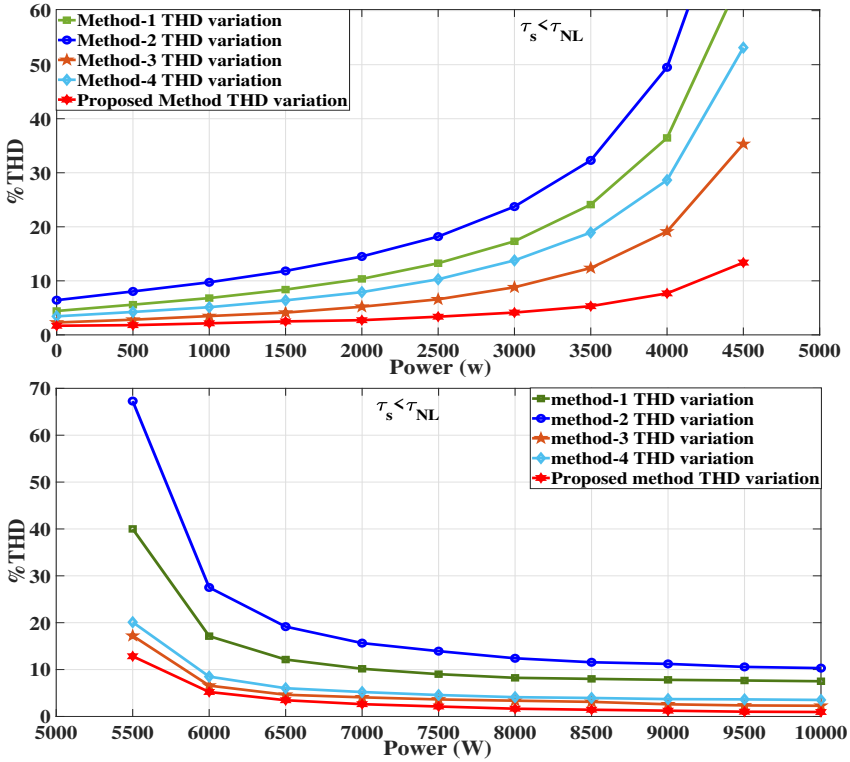

(a) THD Comparison of proposed and different filter inductances methods a) Grid drawing mode(top figure) b) Grid injection mode (bottom figure).

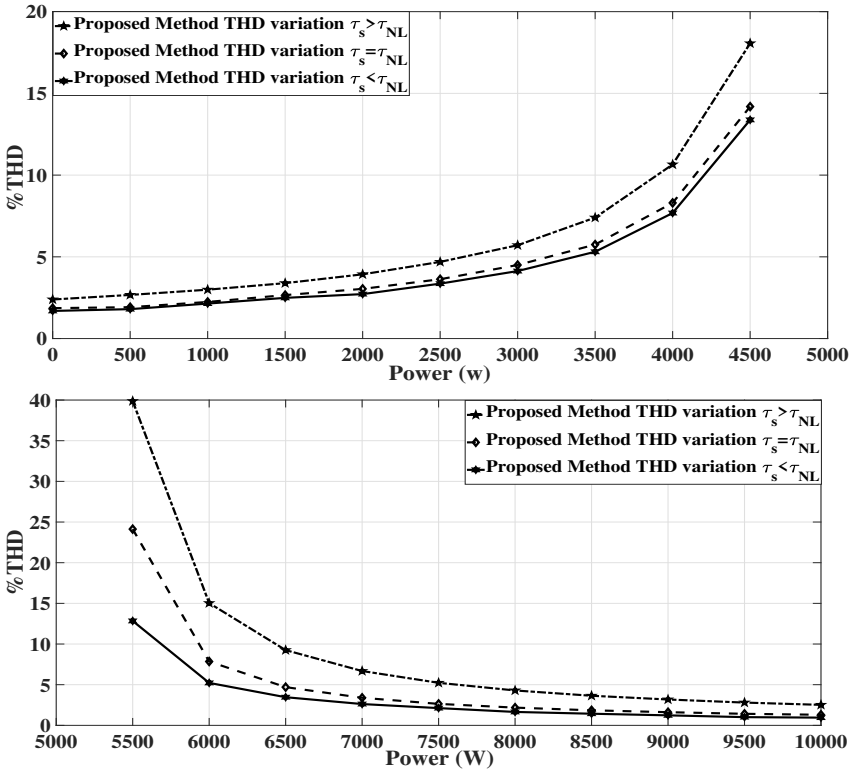

(b) THD Comparison of proposed filter inductance under different time constants with respect to load network time constant a) Grid drawing mode(left figure) b) Grid injection mode(right figure).

Figure 2.13: THD comparison of proposed and different filter inductances in grid drawing and injection modes under proposed controller gain design methods.

2.3.3 Mode-2 operation

In this mode, the available PV power (P_S) surpasses the load power (P_L). Therefore, the excess power ($P_{gi} = P_S - P_L$) is fed into the grid after meeting the load demand. The injection into the grid is limited to the fundamental current, as the nonlinear load absorbs the harmonic currents along with the fundamental load current. Concerning the grid-injected power, the equivalent resistance can be calculated as follows:

$$R_{gi} = \frac{v_{gd}}{Avg(I_{fd} - I_{dl})} \tag{2.30}$$

When real power is injected into the grid, the line impedance (L_g) after the Point of Common Coupling (PCC) can induce power oscillations due to interactions between line (L_g) and filter (L_f) impedance, as illustrated in Fig. 2.14. These oscillations are characterized by a coupling angle (γ). Owing to the coupling angle (γ), the actual currents $I_{dact} = (I_g cos(\gamma))$ and $I_{qact} = (I_g sin(\gamma))$ never perfectly align with the reference currents (I_{dref}) and (I_{qref})), respectively . In this scenario, the power oscillations in the d-domain and q-domain for generating the reference wave can be modeled as (2.32) and (2.33), respectively.

$$V_{inv} = V_d^* + jV_q^* \tag{2.31}$$

$$V_d^* = V_{d(PCC)} + (I_{dref} - I_g cos(\gamma))(K_p + \frac{K_i}{s}) \tag{2.32}$$

$$V_q^* = (-I_g sin(\gamma))(K_p + \frac{K_i}{s}) \tag{2.33}$$

Therefore, it is essential to understand the dynamics of the SiSAPF when injecting active power into the grid. This subsection aims to mitigate power oscillations in a weak grid scenario by compensating the natural deviation angle (γ) induced by grid inductance (L_g).To achieve this, the transfer function of the SiSAPF in grid injection mode is modeled as shown in Equation(2.34), taking into account the network impedance (L_g) and the grid power injected resistance(R_{gi}).

$$G(s) = \frac{R_{gi}.e^{-st}}{(L_g.L_f + L_g^2)(s^2 + \frac{R_{gi}.L_f.s}{L_g.L_f + L_g^2} + \frac{R_{gi}^2}{L_g.L_f + L_g^2})} \tag{2.34}$$

Subsequently, the characteristic equation of the closed-loop system in grid injection mode can be written as :

$$\lambda(s) = 1 + (K_P + \frac{K_i}{s}).(\frac{K.e^{-st}}{s^2 + k.L_f.s + k.R_{gi}}) \tag{2.35}$$

$$\lambda(s) = k(K_i + K_P.s)e^{-st} + s(s^2 + k.L_f.s + k.R_{gi}) \tag{2.36}$$

$$\lambda^*(s) = e^{st}.\lambda(s) \quad Where\ k = \frac{R_{gi}}{L_g^2 + L_g.L_f} \tag{2.37}$$

$$\lambda^*(s) = k(K_i + K_P.s) + s(s^2 + k.L_f.s + k.R_{gi})e^{st} \tag{2.38}$$

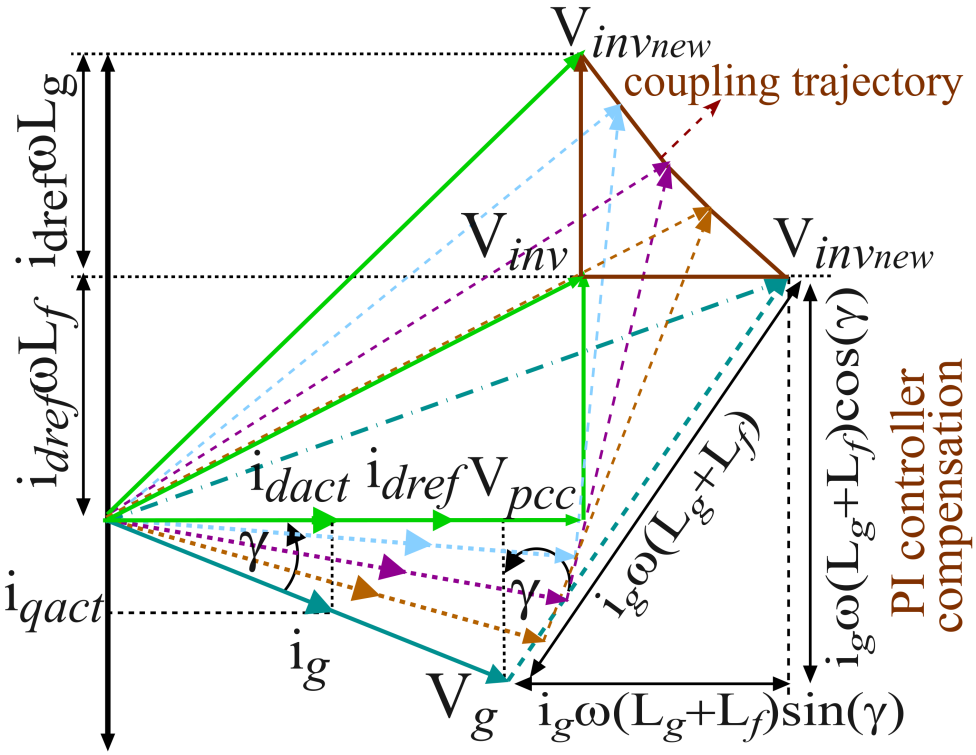

Figure 2.14: The phasor diagram representing the PCC voltage oscillations in the weak grid due to coupling angle γ in grid power injection mode.

Later, the characteristic equation can be decomposed into real and reactive components :

$$\lambda^*(j.\omega) = \lambda_r(\omega) + j\lambda_i(\omega) \tag{2.39}$$

$$\lambda_r(\omega) = kK_i + (\omega^3 - kR_{gi}\omega)sin(\omega t) - \omega^2 kL_f cos(\omega t) \tag{2.40}$$

$$\lambda_i(\omega) = \omega(kK_P + (kR_{gi} - \omega^2)cos(\omega t) - \omega kL_f sin(\omega t)) \tag{2.41}$$

By substituting $\omega = \gamma/t$, Equations (2.40) and (2.41) can be rewritten as:

$$\begin{aligned} \lambda_r(\gamma) &= kK_i + sin(\gamma)(\frac{\gamma^3}{t^3} - \frac{a_0\gamma}{t}) - \frac{a_1\gamma^2 cos(\gamma)}{t^2} \\ \lambda_i(\gamma) &= \frac{\gamma}{t}(kK_P + [cos(\gamma)(a_0 - \frac{\gamma^2}{t^2})] - \frac{a_1\gamma sin(\gamma)}{t}) \end{aligned} \tag{2.42}$$

Here a_o=kR_{gi} and a_1=kL_f .

For any value of coupling angle (γ_0) varies from [-90°,90°], the $\lambda^*(s)$ is stable only when [118]

(1) Condition-1: $\lambda_r(\gamma_0)$ and $\lambda_i(\gamma_0)$ have only simple and real roots and these interlace[86]

(2) Condition-2:$\dot{\lambda_i}(\gamma_0).\lambda_r(\gamma_0) - \lambda_i(\gamma_0).\dot{\lambda_r}(\gamma_0) > 0$

When establishing the lower limit of K_P through condition-2 with the evident root at γ_0=0, the condition-2 simplifies to:

$$\dot{\lambda_i}(\gamma_0).\lambda_r(\gamma_0) = (\frac{kK_P + a_0}{t})kK_i \geq 0 \tag{2.43}$$

Equation (2.43) establishes that K_P must satisfy the condition $K_P \geq \frac{-a_0}{k}$, given that both k and K_i are greater than 0.

Following that, the upper limit of K_P can be established by meeting the interlacing of roots condition as outlined in condition-1, which is only fulfilled when $\lambda_i(\gamma_0) = 0$. As a result, Equation (2.42) can be restructured to determine the potential roots of λ.

$$\gamma = 0 \tag{2.44}$$

$$kK_P + cos(\gamma)(a_0 - \omega^2) - a_1\omega sin(\gamma) = 0 \tag{2.45}$$

In a closed-loop controller, the parameter K_P functions as a virtual RC time constant, effectively dampening the inherent oscillations of the plant. Therefore, it is essential to initially determine the plant's natural oscillations (ω). This determination can be made using Equation (2.45) under the conditions $\gamma = 0$ and $K_P = 0$, as shown below:

$$\omega = \frac{R_{gi}}{\sqrt{L_g.(L_g + L_f)}}; \tag{2.46}$$

Alternatively, the natural oscillations can be deduced from the coupling trajectory depicted in Fig. 2.14. This coupling trajectory, resulting from the cross-coupling terms in the d-axis and q-axis directions, can be recognized as:

$$\frac{v_d}{i_q} = \omega(L_g + L_f) \qquad \frac{v_q}{i_d} = \omega(L_g) \tag{2.47}$$

The system inertial time constant corresponding to the natural oscillations can be derived as:

$$\frac{v_d}{i_q}.\frac{v_q}{i_d} = \omega^2.L_g.(L_g + L_f) \implies R_{gi}^2 = \omega^2.L_g.(L_g + L_f) \tag{2.48}$$

$$\omega = \frac{R_{gi}}{\sqrt{L_g.(L_g + L_f)}}; \implies \tau_g = \frac{1}{\zeta\omega} = \frac{2(L_g.(L_g + L_f))}{R_{gi}L_f} \tag{2.49}$$

where, $\zeta = \frac{L_f}{2\sqrt{L_g.(L_g+L_f)}}$. Here, ζ represents the damping ratio of the system, and it can be determined using Equation (2.34). Additionally, τ_g denotes the time constant of the derived second-order system. Furthermore, when we substitute values of ω and γ for less than 90^o into Equation (2.45), we obtain:

$$K_p < L_f.\frac{R_{gi}Sin(\gamma)}{\sqrt{L_g(L_g + L_f)}} \tag{2.50}$$

To ensure the injection of a perfectly sinusoidal current into the grid after satisfying load demands for harmonics and active power, it's crucial to satisfy the condition $\tau_g > \tau_n$. To meet this condition, it's essential to establish a relationship between the determined value of K_P and τ_g.

$$K_P < \frac{2\sqrt{L_g(L_g + L_f)}}{\tau_g} sin(\gamma) \tag{2.51}$$

From Equation(2.51),It is clear that the value of K_P is notably influenced by τ_g, and τ_g

is, in turn, dependent on τ_n.Therefore, to achieve a perfectly sinusoidal current injection into the grid, the right value for K_P is identified, ensuring that the system's time constant (τ_g) is greater than the network's time constant (τ_n). Furthermore the range of K_P value in relation to τ_g by employing Equations (2.43) and (2.51) as follows:

$$-R_{gi} \leq K_P < \frac{2\sqrt{L_g(L_g + L_f)}}{\tau_g} sin(\gamma) \tag{2.52}$$

2.3.4 The selection of controller gains based on the mode of operation

This subsection emphasizes the critical role of the controller gain range in determining the closed-loop system bandwidth. This dynamic range boundary depends on the solar-injected power, illustrated in Fig. 2.15. In grid drawing mode, the controller gain

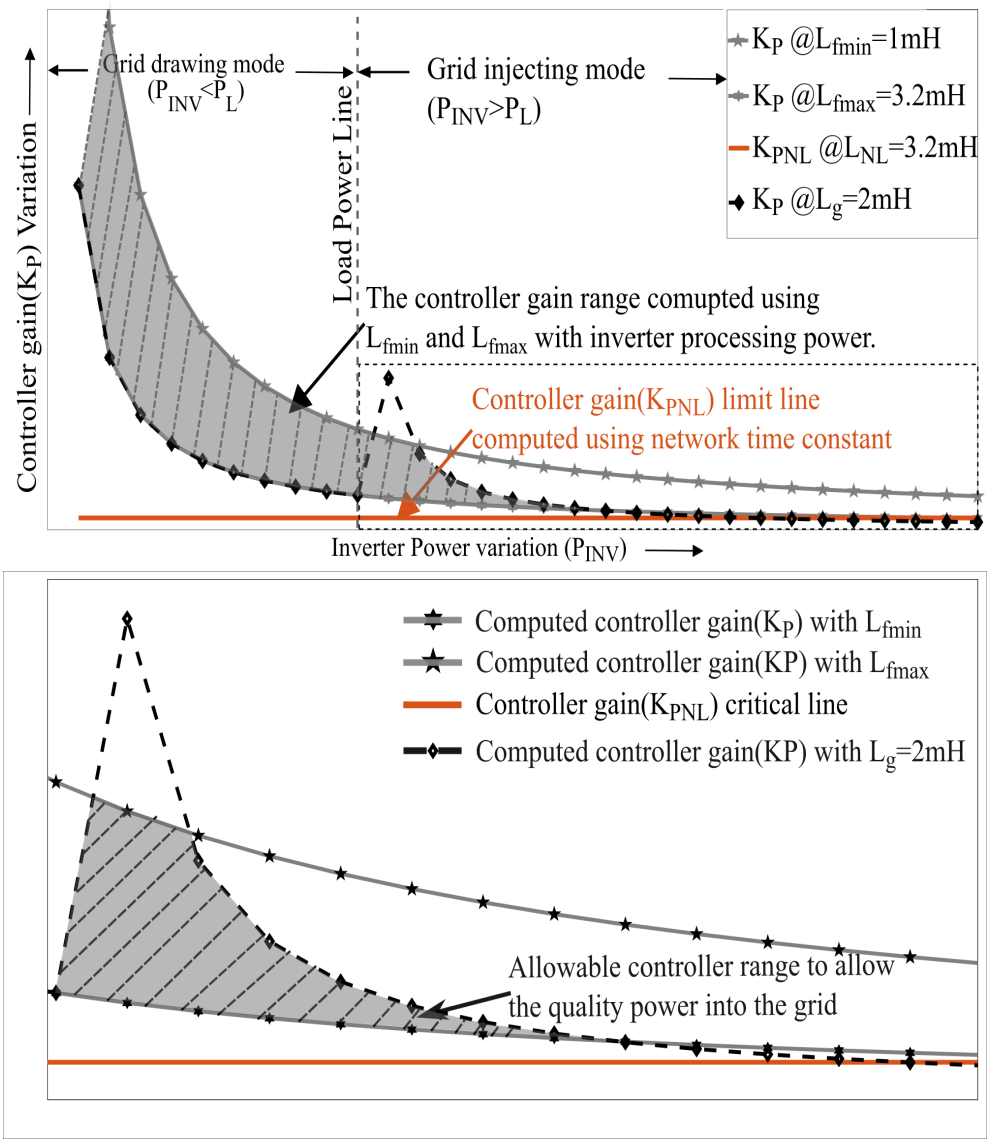

Figure 2.15: a) Allowable controller range for the SiSAPF from minimum to maximum controller gain with respect to when the system changes from grid drawing mode to grid injection mode. b) The zoomed portion of the grid-injected mode region to ensure the limit for the grid-injected power.

variations are calculated within the shaded region, considering the permissible inductance value range (minimum and maximum) outlined in Section 2.1. The pattern reveals that the gain should decrease with an increase in power, as depicted in the top trace of Fig. 2.15. Additionally, computed controller gains must be higher than the proportional gain corresponding to the network time constant. In grid injection mode, where the inverter processing power exceeds the load demanded power, the proportional gain limit, computed in Section 2.3.3, must be considered, as shown in the zoomed portion of Fig. 2.15. The intersection area between the upper and lower inductance values determines the total SiSAPF processing power, constrained by the grid-injected power limit. In this mode as well, it is crucial to ensure that the resultant computed gain exceeds the gain corresponding to the network time constant, as illustrated in the zoomed portion of Fig. 2.15. The efficacy of the SiSAPF design and closed loop controller modeling in both grid drawing and injected mode of operation is verified experimentally, and the obtained results are discussed in the following section.

2.4 Results and Discussion

This analysis is confirmed by developing the SISAPF lab prototype, illustrated in Fig. 2.16. Design parameters for harmonic compensation and active power injection in the SISAPF prototype are provided in Table-2.1. Furthermore, the experimental section discusses the effect of controller gains on the computed inductance range during harmonic compensation and active power injection in both grid drawing and injection modes, as previously mentioned.

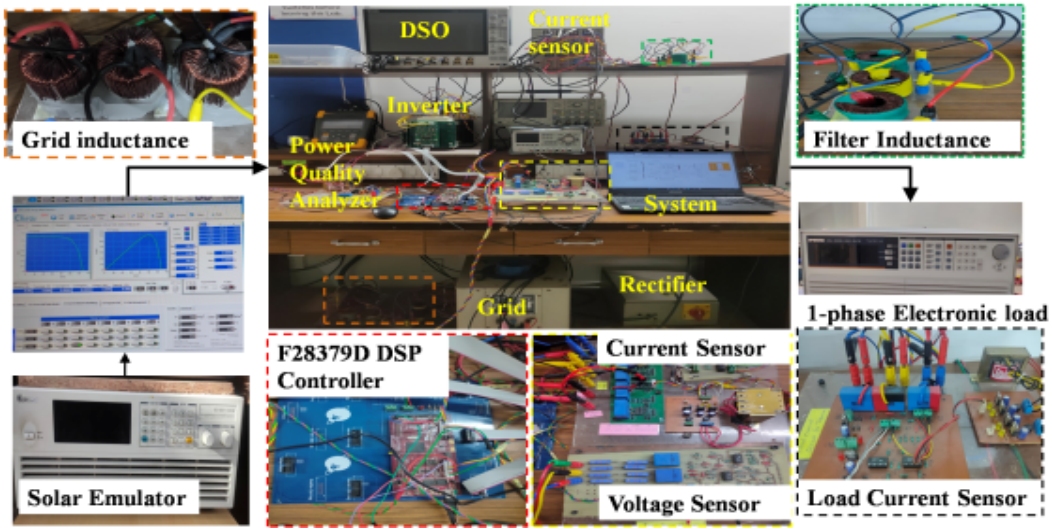

Figure 2.16: The SiSAPF hardware prototype developed in the lab.

In this work, a nonlinear load represented by an AC/DC rectifier is demonstrated using a DC load resistance of $R_L = (18.67(\mathbb{R}) \times 1.823)\Omega$. Initially, this load is powered by the utility grid supply. The rise time of the load current is observed and compared in both stationary (a-phase current) and synchronous reference frame (I_{ld} and I_{lq}), as depicted in Fig.2.17, to calculate the network time constant (τ_n).

Table 2.1: Specifications of Filter Design.

PCC voltage = 121 V (L-L RMS), load output voltage = 163.74 V Load Power(P_L)=787.39 W, Load input Current (I_L)=3.75 A, Inverter Power(P_S)= 1500 W, Inverter current (I_f)= 7.143 A, load equivalent resistance($\mathbb{R} = R_{NL}$) = 18.67.

	General filter	Proposed filter
filter design (L_f)	$L_f = \frac{V_{dc}}{8F_{sw}\triangle I_{pp}}$	$L_f = \frac{\mathbb{R}}{2\pi f_{sw}}$
DC-link voltage (V_{dc})	300 V	300 V
modulation index (M_a)	1	1
Switching Frequency (F_{sw})	5KHz	5KHz
current ripple ($\triangle I_{pp}$)	10%	-
Filter inductance (L_f)	10.49 mH	0.594 mH $\approx$ 0.6mH

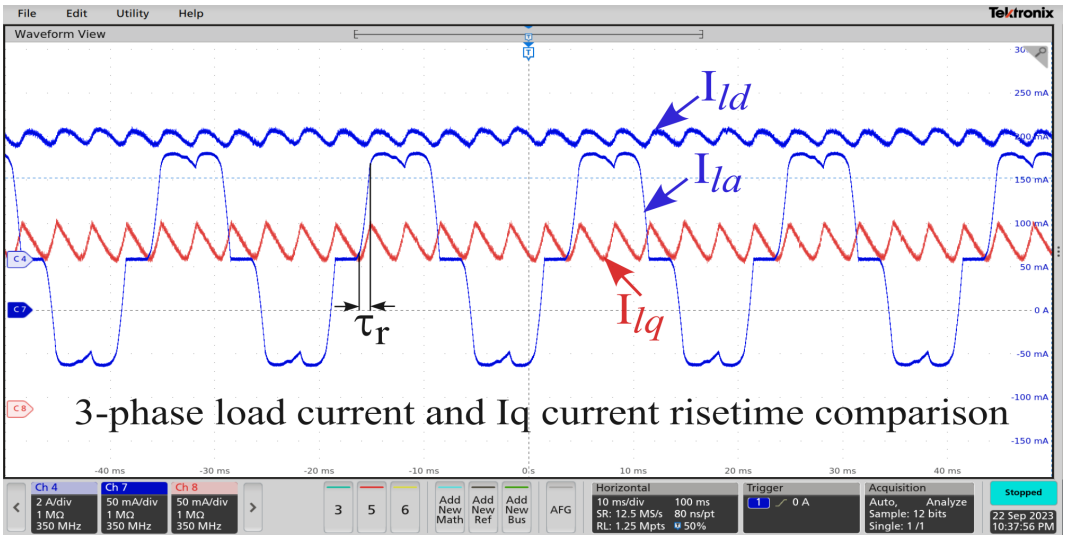

Figure 2.17: The a-phase non linear load current (X-limit: 2A/div, Y-limit: 10ms/div) along with equivalent current correspond to real (i_{dl}) and reactive power (i_{ql}) (X-axis: 50mA/div, Y-axis: 10ms/div).

From Fig. 2.17, it's clear that the rise time of the nonlinear load diode current during the off-to-on transition precisely matches that of the load current's reactive component, I_{lq}, which is 0.416ms (τ_r). Using this derived rise time, the network time constant can be computed as $\frac{\tau_r}{2.197}$, resulting in 0.1896ms. Notably, this computed load network time constant, based on the rise time at a load inductance of $L_{NL} = 3.2$mH and resistance of $\mathbb{R} = 18.675\Omega$, aligns with the calculated network time constant (τ_n). This confirms the accuracy of the measurement-based network time constant computation and its independence from specific parameters. With the specified load inductance and resistance, the grid current % THD is measured at 22.6% (without compensation), as seen in Fig. 2.18. Using the computed network time constant and network equivalent resistance, the filter inductance for SiSAPF is determined to be 0.6mH.

Based on the network time constant, the computed passive filter design for SISAPF harmonic compensation is compared with the conventional ripple-based filter and detailed in Table-2.1. With the calculated filter parameters, the SISAPF was tested experimentally,

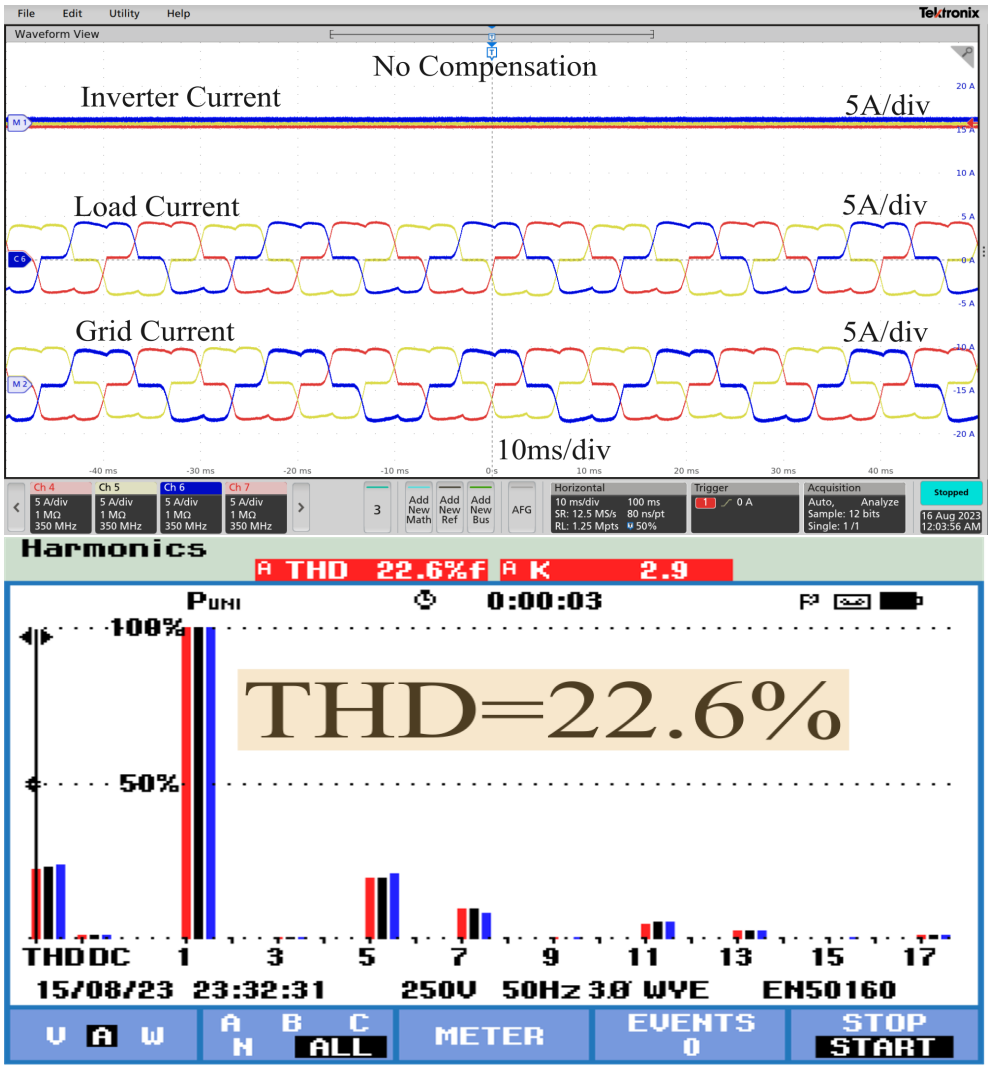

Figure 2.18: The 3-phase inverter currents (top trace), load currents (Middle trace), and grid currents (bottom trace) with no compensation from the SiSAF (Left) and corresponding grid current harmonic spectrum (Right)

and the current waveforms of the SISAPF, load, and grid are shown in Fig. 2.19a. In Fig. 2.19a, the conventional method exhibits visible notches in the grid current, reducing grid current THD to 12.4%. In contrast, the proposed method effectively compensates for these notches in the grid current, reducing the grid current THD to 4.4% as illustrated in Fig. 2.19b. This improvement is attributed to the smaller filter inductance in the proposed design, providing a wider bandwidth for accommodating load-demanded harmonics compared to the ripple-based design with higher inductance. Additionally, the computed system time constant is lower than the network time constant, allowing the passive filter design to increase the filter value to align with the network time constant. The effectiveness of the minimum and maximum boundaries specified in the proposed filter inductance design methodology (Section-2.2) is validated for simultaneous harmonic compensation and power injection in both grid drawing and injection modes, utilizing the network parameters detailed in Table-2.2.

The influence of the computed passive filter inductance range on the grid current's %THD

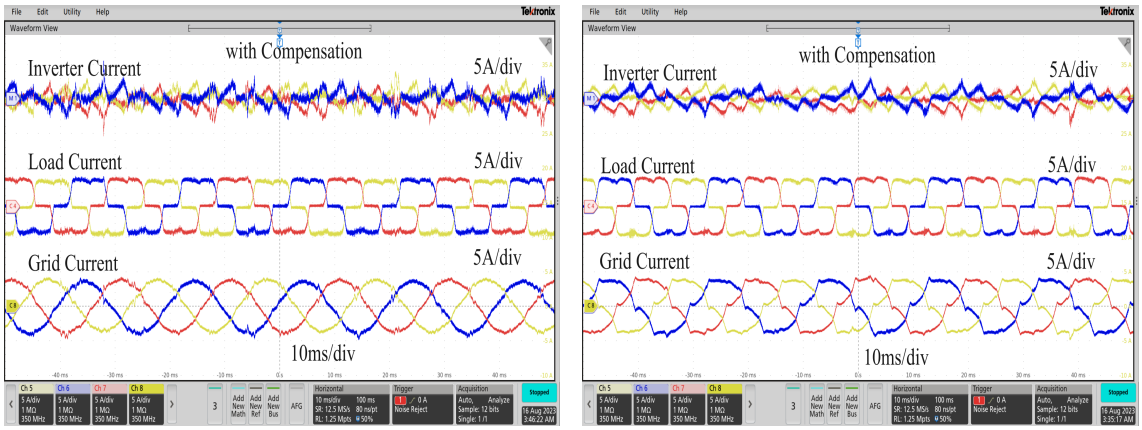

(a) The three-phase Inverter currents (top trace), load currents (Middle trace), and grid currents (bottom trace) (X-limit: 5A/div, Y-limit: 10ms/div).

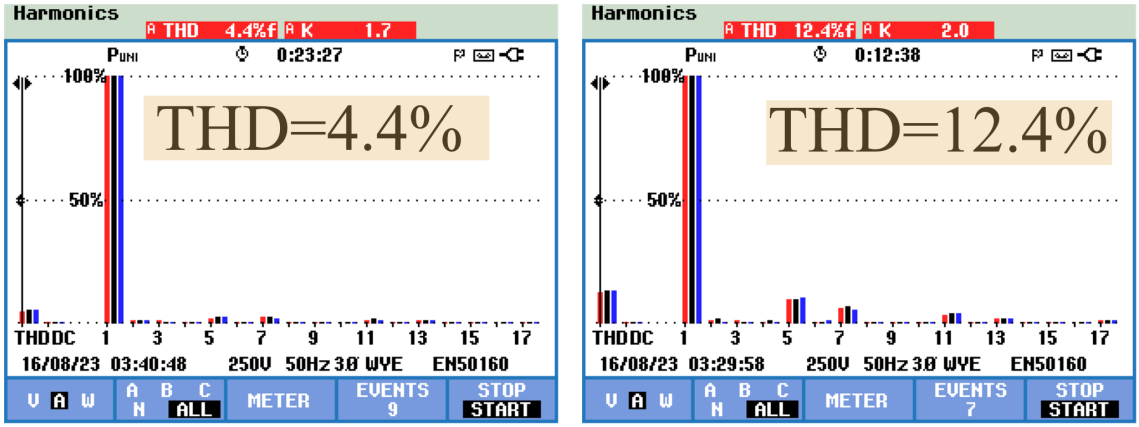

(b) The Grid current harmonic spectrum with %THD.

Figure 2.19: The experimental comparison when SiSAPF operates in harmonic compensation mode with Filter inductance $L_f = 0.6mH$ computed through the proposed method (left figure) and $L_f = 10mH$ computed using ripple-based filter design (Right figure).

is experimentally shown in Fig. 2.20. In the left figure of Fig. 2.20, the minimum filter inductance maintains %THD at 4.4%, while the maximum filter inductance keeps it at 4.8%. However, when the filter inductance surpasses this range, notches appear in the grid current, resulting in a higher %THD of 6.9%. This indicates that the SiSAPF cannot provide the necessary high-frequency components through the inverter circuit to meet load demands.

To design the controller gains, the consideration of the system time constant(τ_s) is crucial, and the system time constant should be less than the network time constant(τ_n). For practical experimentation, the SiSAPF is validated with the various time constants, as depicted in Fig. 2.21. The system constant is lesser than the network time constant ($\tau_s = 0.05msec < \tau_n$), as shown in Fig. 2.21a, which effectively compensates the harmonics and reduces the grid current %THD to 4.6%. Incase, at system time constant is equal to network time constant ($\tau_s = 0.1713msec = \tau_n$)as shown in Fig. 2.21b, The bandwidth for the load demanded harmonics is reduced, which starts degrading the grid current quality, and increase the %THD to 5.1%. Conversely, at a higher time constant ($\tau_s = 0.2msec >$

Table 2.2: The Nonlinear load network parameters along with SiSAPF system parameters at different SiSAPF's operating modes.

Network Parameters		Grid drawing mode		grid injected mode	
		$P_S < P_L$		$P_S > P_L$	
grid side inductance(L_{NL})	3.2mH	Inverter power (P_S)	790 w	Inverter power (P_S)	1500 w
load resistance(R_L)	18.68Ω	Equivalent resistance ($\mathbb{R}_2$)	18.68Ω	Grid power(P_{gi})	712 w
time constant (τ_n)	0.1713 msec	switching frequency (f_{sw})	5kHz	Switching frequency (f_{sw})	5kHz
load Power (P_L)	790 W	minimum filter inductance ($L_{f_{min}}$)	0.594mH	grid side inductance(L_g)	3.2mH
fundamental Frequency(F_n)	50Hz	$\tau_{min} = L_{f_{min}}/R_2$ & $\tau_{max} = L_{f_{max}}/R_2$	0.03183 msec & 0.1713 msec	filter inductance ($L_{f_{min}}$)	0.594mH
		Maximum filter inductance($L_{f_{max}}$)	3.2mH	filter inductance ($L_{f_{max}}$)	3.2mH
		Kp at $L_{f_{min}}$ (K_P for controller @ Z_{base} = 18.68Ω) & Kp with$L_{f_{max}}$ (K_P for controller @ Z_{base} = 18.68Ω)	3.46 (0.2)& 18.68 (1.0)	Kp with L_{fmin}	3.46 (0.2)

τ_n), as shown in Fig. 2.21c, the controller bandwidth is not sufficient to compensate for the grid current, resulting in an increase of grid current %THD to 8.4%. Considering the different time constants for computing the controller gains for the effective harmonic compensation, the system constant should vary between (τ_{min} *to* τ_n). Furthermore, the effect controller gains on harmonic compensation is discussed in the following paragraph.

The controller gains for SiSAPF at the computed minimum and maximum filter inductance are assessed, and the results are presented in Table-2.2. The practical effectiveness of these evaluated gains is experimentally validated across various controller gain settings using the computed passive filter for SiSAPF, as demonstrated in Fig. 2.22. A controller gain lower than the computed K_p (0.1PU), as seen in Fig. 2.22a, causes notches in the grid current due to insufficient controller bandwidth, causing an increase in % THD to 8.9%. At the computed K_p, as shown in Fig. 2.22b, the controller provides sufficient bandwidth to mitigate load-demanded harmonics, reducing grid current % THD to 4.5%. Conversely, higher K_p results in a grid current % THD of 9.1%, as seen in Fig. 2.22c. While higher

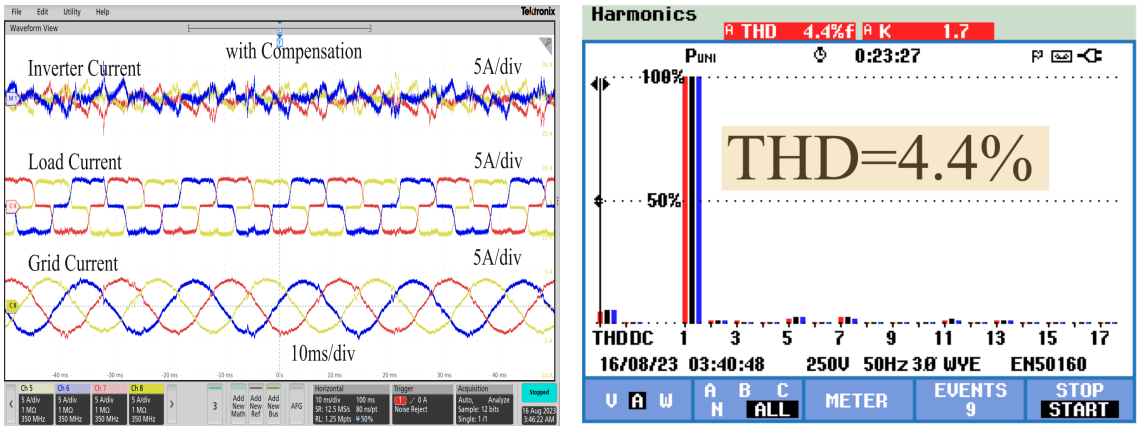

(a) $L_f = L_{fmin} = 0.6mH.$

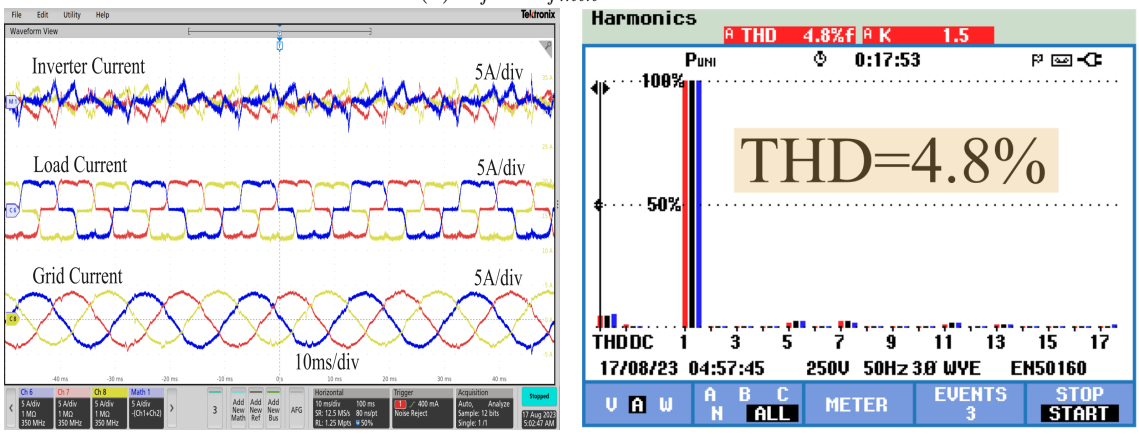

(b) $L_f = L_{fmax} = 3mH.$

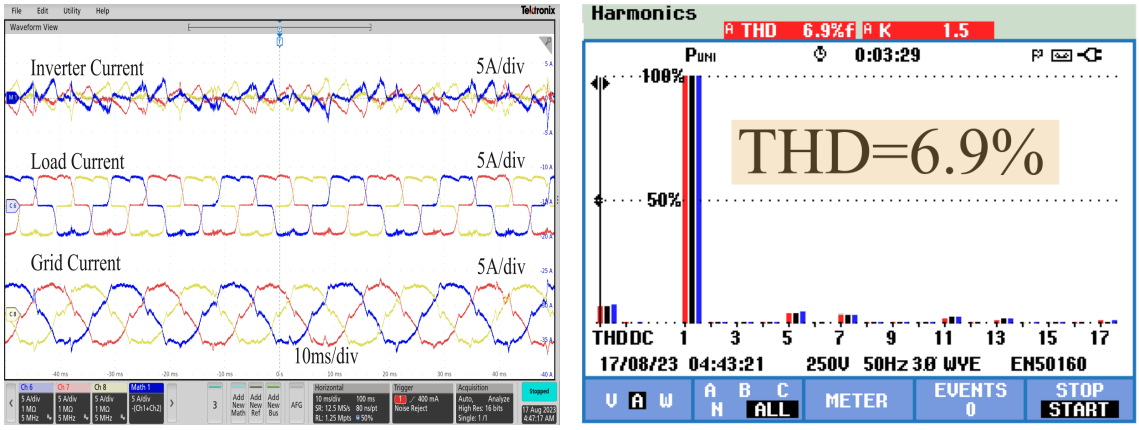

(c) $L_f > L_{fmax} = 6mH.$

Figure 2.20: The effect of different filter inductances on SiSAPF circuit and grid current THD. The SiSAPF current (top trace X=10ms/div, Y=5A/div), nonlinear load current(middle trace X=10ms/div, Y=5A/div), and grid current(bottom trace X=10ms/div, Y=5A/div)and their corresponding grid current THD (right figures).

controller gains improve the system's dynamic response, they lead to peak overshoots and negatively impact current quality, considering the load network time constants. Further, the computed controller gain and passive filter observe the dynamic change in the source power.

The effectiveness of SiSAPF in handling dynamic changes in source power is demonstrated in Fig. 2.23. The system's dynamic response is showcased as the source power varies from

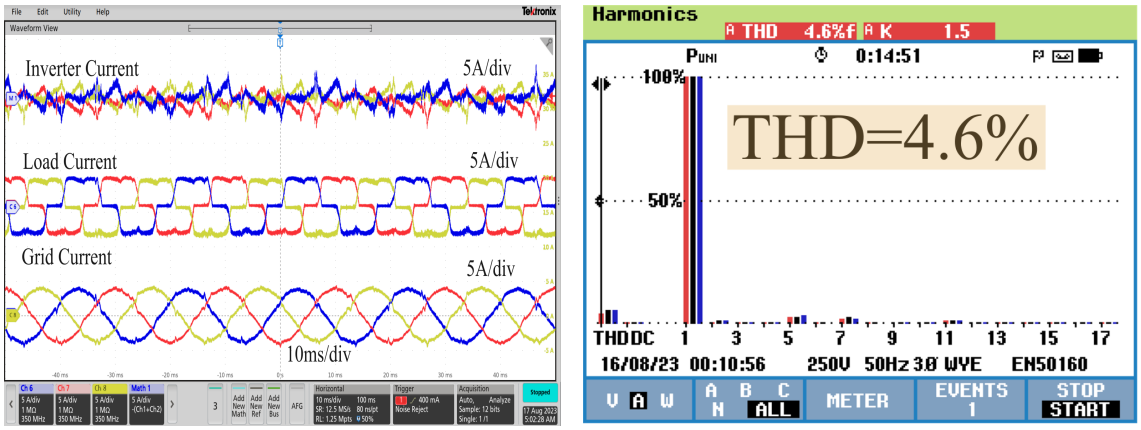

(a) $\tau_s(0.05msec) < \tau_n(0.1713msec)$.

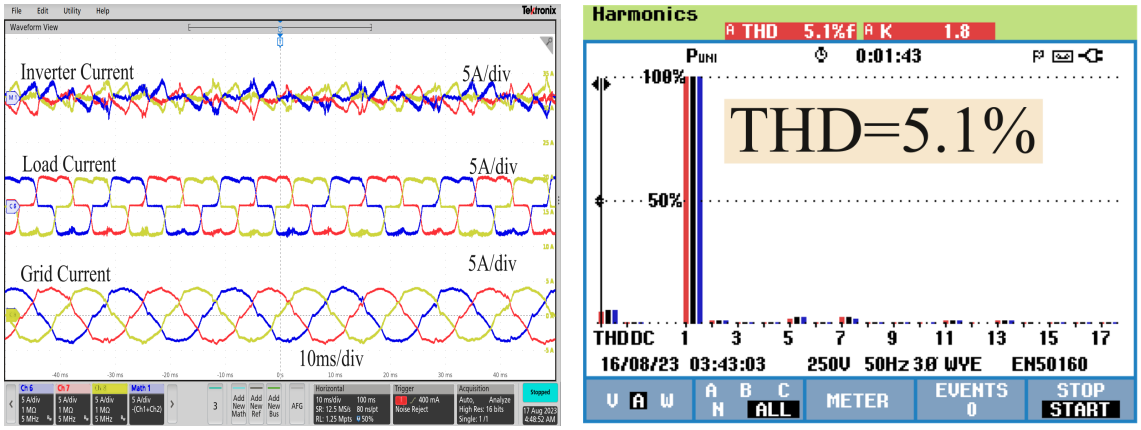

(b) $\tau_s(0.1713msec) = \tau_n(0.1713msec)$.

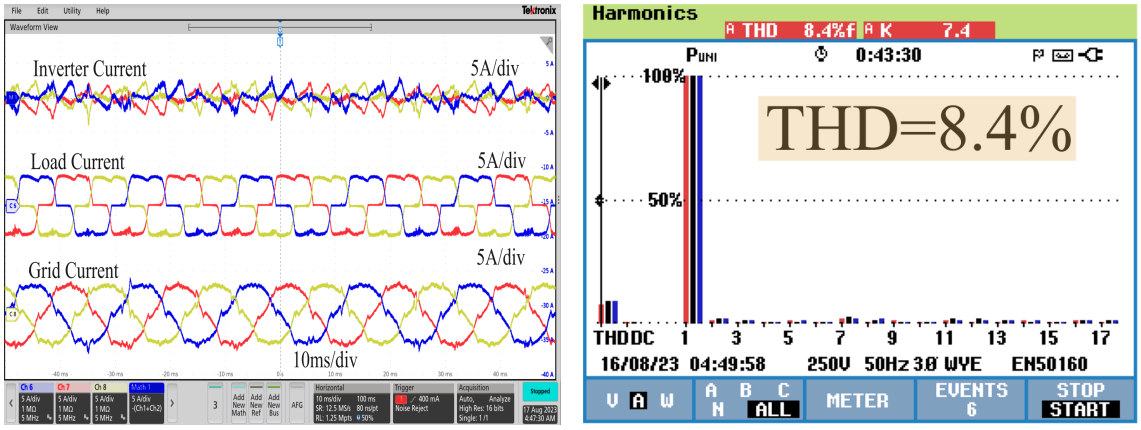

(c) $\tau_s(0.2msec) > \tau_n(0.1713msec)$.

Figure 2.21: The effect of different system time constant over network time constant for SiSAPF circuit on grid current THD. In the left figures, SiSAPF current (top trace X=10ms/div, Y=5A/div), nonlinear load current(middle trace Y=5A/div), and grid current(bottom trace Y=5A/div) for one designed filter inductance and their corresponding grid current THD (right figures).

10W to 790W and then from 790W to 1500W. In the dynamic characteristics, both grid drawing ($P_s < P_L$) and grid injection modes are displayed while maintaining the load at 790W, as shown in the zoomed left and right traces of Fig. 2.23. In both cases, the grid currents remain sinusoidal, affirming the efficacy of the SiSAPF filter design across different power ranges. Additionally, the power injection limit concerning controller gains

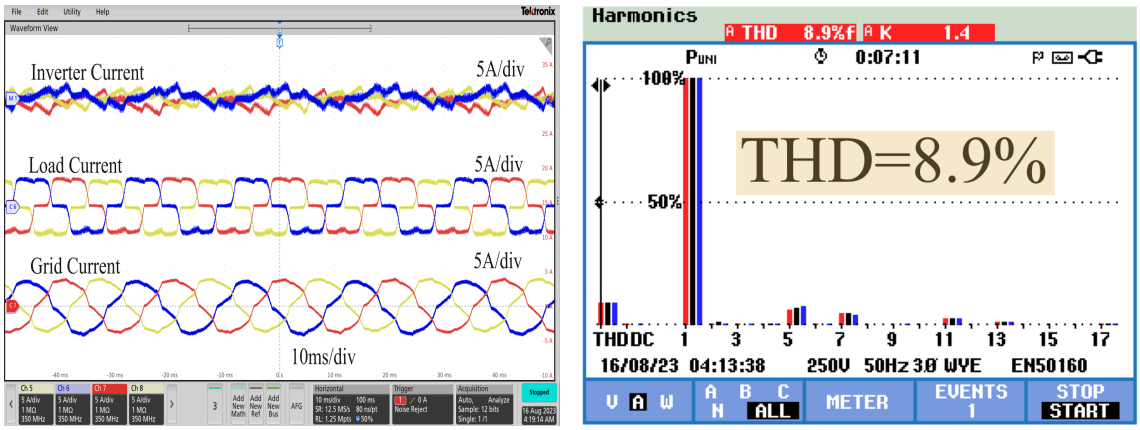

(a) $\tau_s(0.05msec) < \tau_n(0.1713msec)$.

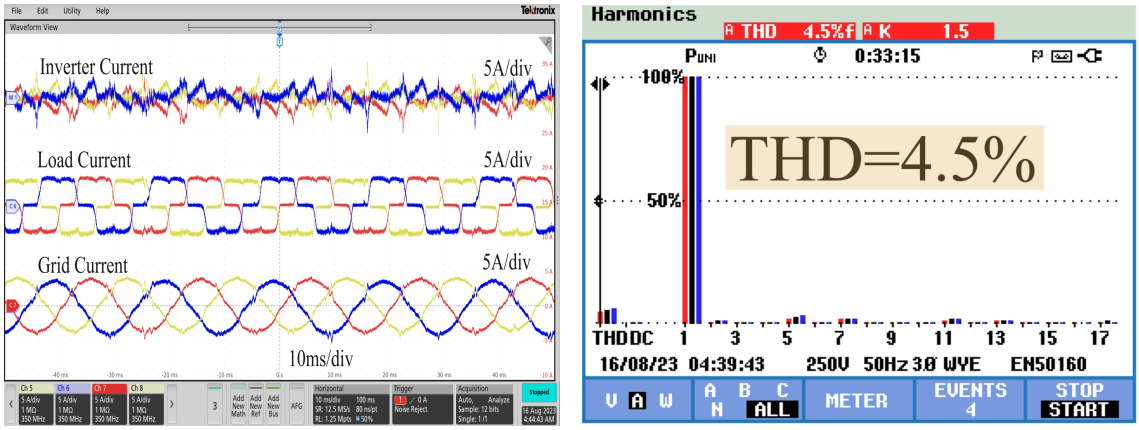

(b) $\tau_s(0.1713msec) = \tau_n(0.1713msec)$.

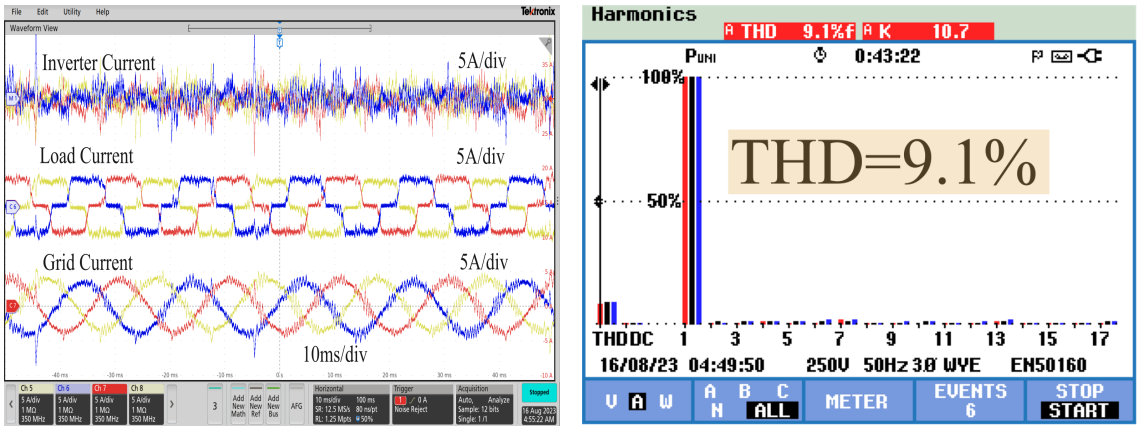

(c) $\tau_s(0.2msec) > \tau_n(0.1713msec)$.

Figure 2.22: The effect of different system time constant over network time constant for SiSAPF circuit on grid current THD. In the left figures, SiSAPF current (top trace X=10ms/div, Y=5A/div), nonlinear load current(middle trace Y=5A/div), and grid current(bottom trace Y=5A/div) for one designed filter inductance and their corresponding grid current THD (right figures).

due to uncompensated grid inductance is demonstrated, as discussed in Section-2.3.3. The grid inductance (Lg) is emulated in the grid line to create a weak grid with a short circuit ratio (SCR) between 2 and 3. The experimental parameters in Table-2.3 for validate the injected power quality at varying controller gains, as shown in Fig.2.15. Under the emulated weak grid conditions, experiments are conducted with controller gains falling

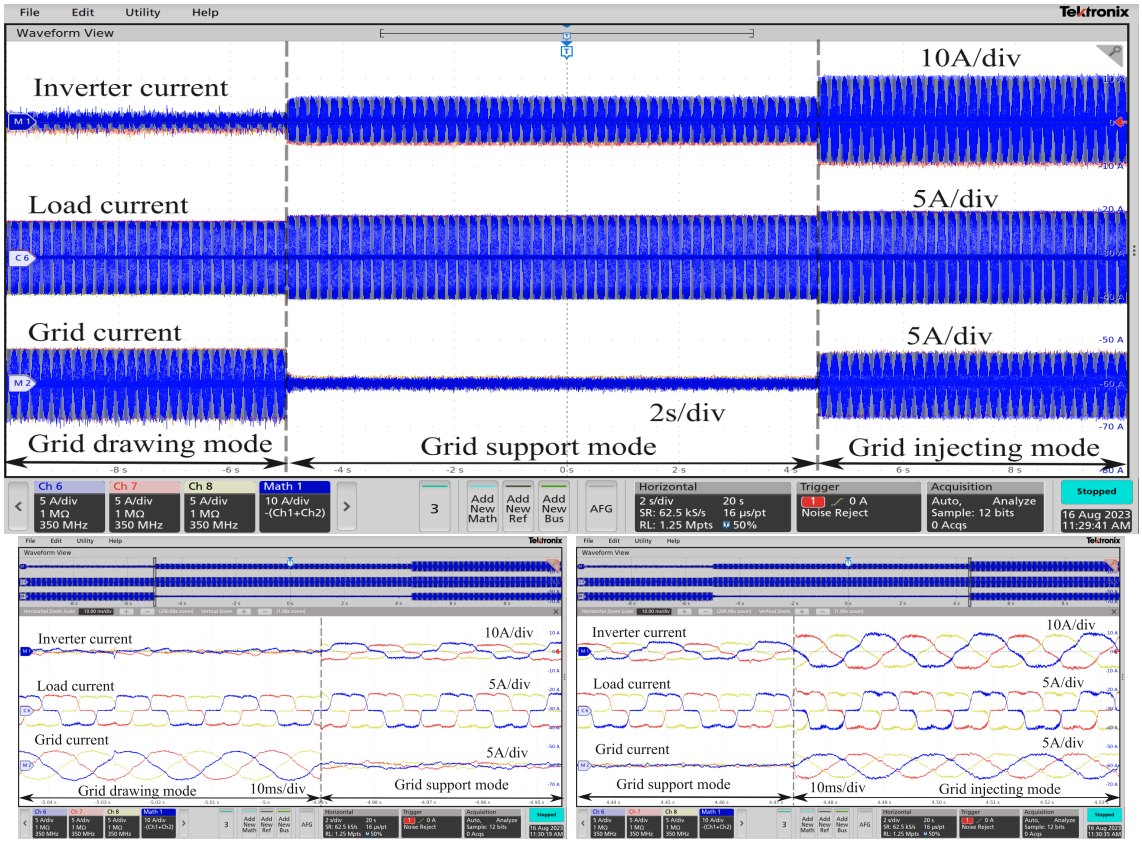

Figure 2.23: The SiSAPF current(top trace X=2sec/div, Y=10A/div), three-phase non-linear load current(middle trace Y=5A/div), and grid current(bottom trace Y=5A/div). The zoomed portions correspond to the dynamic variation of SASAF power from 10 W to 790 W(left figure X=10msec) and 790 W to 1400 W(right figure).

Table 2.3: Considered parameters for weak grid condition experimentation.

Grid voltage(V_g) = 230 V, PCC voltage(V_{PCC})= 140 V, DC-link voltage(V_{dc})= 400 V, load Power(P_L)=1500 W, load current(I_L)= 3.57 A, Inverter Power(P_S)= 3000 W, Inverter current (I_f)= 6.66 A, $\mathbb{R} = 39.2\Omega$, network inductance(L_{NL})=3.2mH, Time constant(τ_n=0.0816msec).

Grid inductance (L_g)	14.5mH
internal resistance of inductance	3.5 Ω
filter inductanceL_{fmax}	3.2 mH
Controller gain (K_P@L_{fmax})	1 P.U
Controller gain (K_{Pweak})	0.2 P.U
Fundamental frequency(F_n)	50 Hz

both outside and inside the intersection area described in Fig. 2.15, and the results are depicted in Fig. 2.24. When the gain is outside the designated area ($K_p > K_{pweak}$), such as at $K_p = 2$ PU, oscillations occur due to impedance interactions, resulting in elevated grid-injected current %THD (9.9%), as seen in the harmonic spectrum in Fig. 2.24a. These oscillations can be suppressed with the appropriate selection of controller gain, as computed in Table-2.3 ($K_{pweak} = 0.2$ P.U), as evidenced by the experimental results in Fig. 2.24b. With the computed controller gain, grid current distortions are mitigated, leading to an improved grid current THD of 4.9%. This discussion highlights the adverse

impact of exceeding threshold controller values on grid power quality in accordance with IEEE standards.

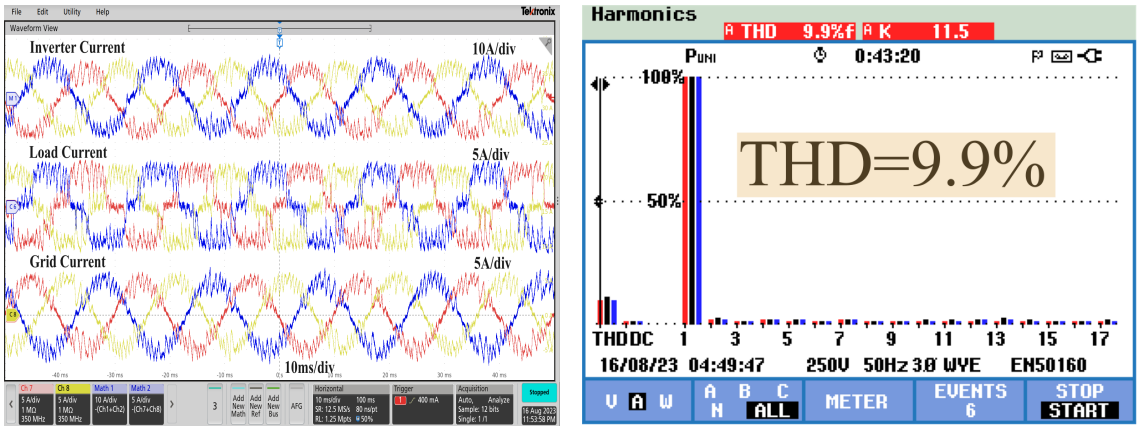

(a) With the controller gain outside the recommended area as described in Fig. 2.15

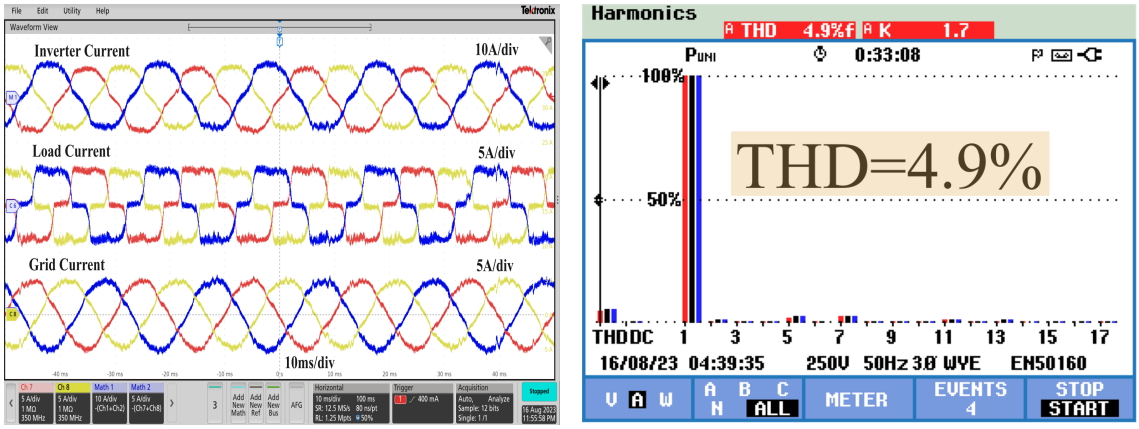

(b) With the controller gain falls within the recommended area as described in Fig. 2.15

Figure 2.24: The SiSAPF current(top trace X=10ms/div, Y=10A/div), three-phase load current(middle trace Y=5A/div), and grid current(bottom trace Y=5A/div) and corresponding grid injected current %THD with mimicked weak grid condition.

2.5 Conclusion

This work demonstrates a solar-interfaced shunt active filter for supplying active power and mitigating nonlinear load harmonics from grid current. The nonlinear load current harmonics are addressed using a synchronous reference frame, and the controller's reactive power component is observed to encompass the three-phase load current bandwidth. The load network's time constant is determined based on the rise time of the reactive power component. This identified network time constant discusses and analyzes an effective filter design. Compared to ripple-based filter designs, the proposed filter design offers a wider bandwidth, significantly enhancing grid current quality by reducing %THD from 22.6% to 4.4%. The closed-loop controller gains are computed using the determined network time constant and filter design to shape the grid current into a pure sinusoidal pattern. During grid power drawing operation, the filter inductance and proportional controller gains are adjusted to match the required network time constant, ensuring that the grid

current quality remains within IEEE standards. In the grid-injected operation mode, interactions with the grid inductance due to injected power are modeled to understand the effect of injected power quality. Consequently, appropriate controller gain tuning dampens oscillations induced by system inductance, maintaining THD within IEEE standards in grid-injected mode.

Chapter 3

A Front End Multi-Functional Solar Converter with Adaptive Controller Bandwidth Realization Through Source and Load Equivalent Impedance Estimation

3.1 The proposed offboard PV interfaced charging circuit with front end inverter

The schematic of Fig. 3.1 introduces the PIFI configuration, adeptly managing dynamic source and load changes. This system adeptly manages harmonics required by the EV charging circuit (Nonlinear load) and seamlessly integrates solar power into the AC network. As depicted in Fig. 3.1, the PIFI is strategically positioned at a common AC interface point (ACIP), facilitating connection to the utility grid and nonlinear load. In this setup, inductance (L_g) precedes the diode bridge rectifier (DBR) as an AC filter to minimize voltage ripple on the DC side[119]. A passive filter, denoted as (L_f), links to the inverter's output terminals. The primary goal of the passive filter is to inject active power and load-demanded harmonics while attenuating switching frequency components. Furthermore, the chosen inductance establishes the PIFI angular frequency at the injected power. Consequently, the design of the filter inductance takes into account the inverter's operating switching frequency and the necessary level of attenuation, ensuring that the inductor provides higher impedance to the switching current ripple by generating the back EMF (e_{sw}).

$$e_{sw} = i_{sw}.\omega_{sw}L_f \tag{3.1}$$

Here, i_{sw} represents the switching harmonic current at the switching frequency ω_{sw}. The inductor's impedance must be equivalent to the resistance corresponding to the active power injected into the grid. Thus, the computation for the filter inductance is as follows:

$$L_f = \frac{3V_{ph(peak)}^2}{P_{pv}\omega_{sw}} \tag{3.2}$$

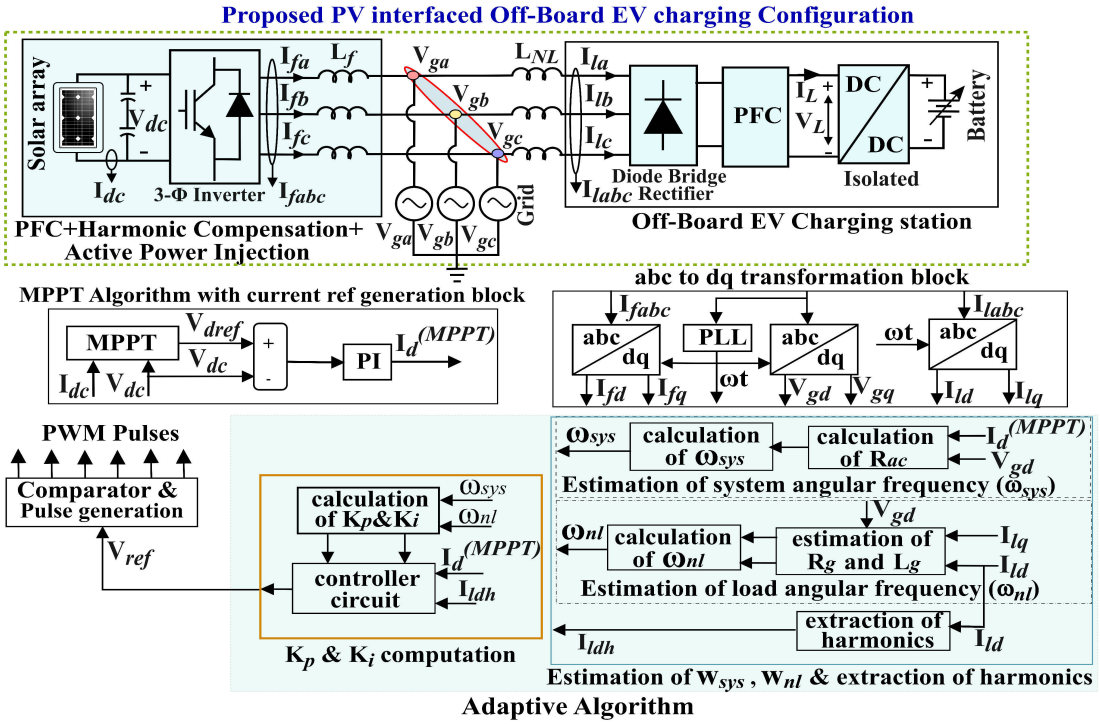

Figure 3.1: The proposed PV interfaced front-end inverter-based offboard charger.

Here, V_{ph} represents the phase voltage of the grid, and P_{pv} stands for the PV instantaneous power injected into the grid. According to equation (3.2), the computed inductance, based on solar power, demonstrates a nonlinear profile at various switching frequencies, as illustrated in Fig.3.2. For a given inductance, the PIFI time constant and the

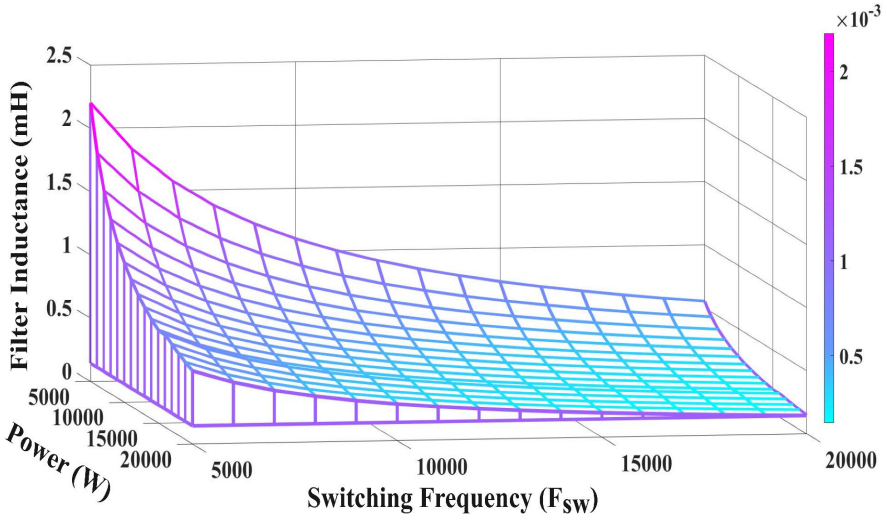

Figure 3.2: The Nonlinear profile of the PIFI filter inductance requirement with varying active power injection and switching frequency.

corresponding angular frequency can be defined as:

$$\tau_{sys} = \frac{L_f}{R_{ac}} \implies \omega_{sys} = \frac{R_{ac}}{L_f} \tag{3.3}$$

Here, R_{ac} represents the equivalent resistance corresponding to the PV-injected power. The signal flow diagram for estimating the system angular frequency at a given filter inductance and PV power is illustrated in Fig. 3.3. The variations in estimated angular

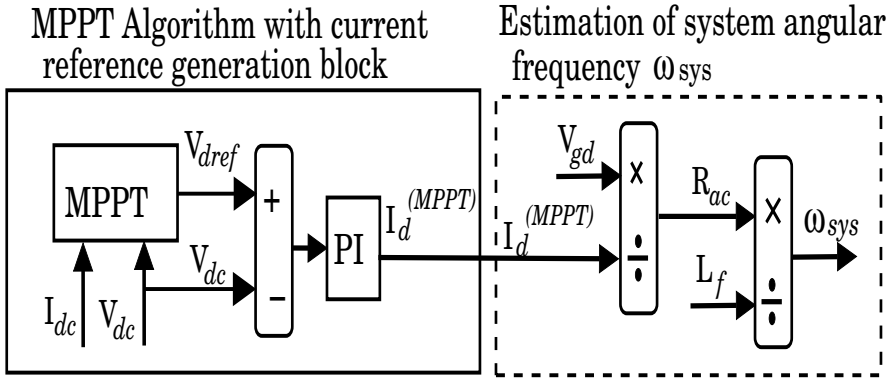

Figure 3.3: The estimation of system angular frequency (ω_{sys}) at different solar irradiance computed using maximum power tracking algorithm.

frequency with varying solar powers at different filter inductances are depicted in Fig. 3.4. The figure highlights the fluctuation in solar power influencing the system's angular frequency at a given filter inductance, thus shaping the system's control dynamics. As depicted in Fig. 3.4, lower power (equivalent to higher resistance) necessitates a higher filter inductance, compromising the PIFI response speed. Conversely, lower inductance raises concerns about current distortion at lower power levels. Considering these trade-offs, it is recommended to select the inductance value by carefully observing the system's angular frequency at the desired solar power injection, as illustrated in Fig. 3.4. Further,

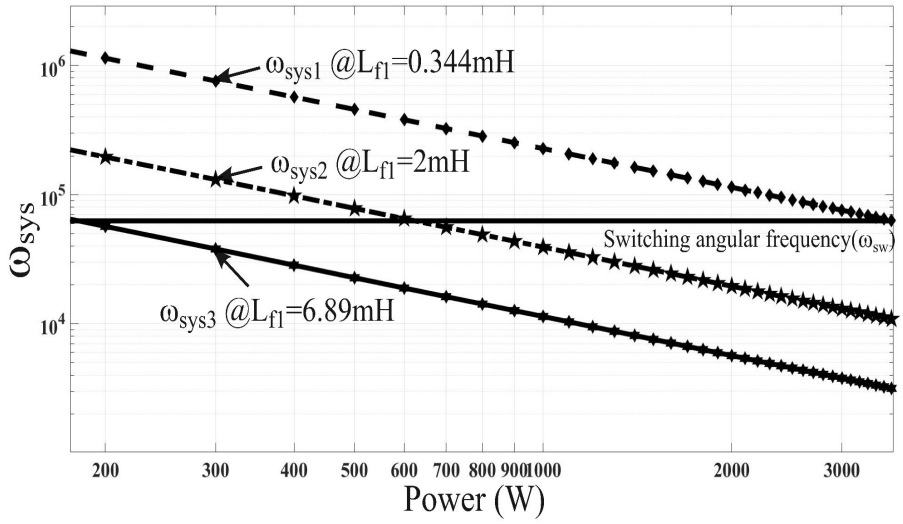

Figure 3.4: The PIFI angular frequency ($\omega_{sys} = \frac{R_{ac}}{L_f}$ realization with injected powers at different filter inductance.

the angular frequency variations with the load network parameters are analyzed in the subsequent section to outstretch the PIFI capability of processing simultaneous load harmonics and source active power.

3.2 Estimation of nonlinear load angular frequency dynamics

The charging stations fed from the diode bridge rectifiers draw the nonlinear current from the AC network as shown in Fig.3.5.

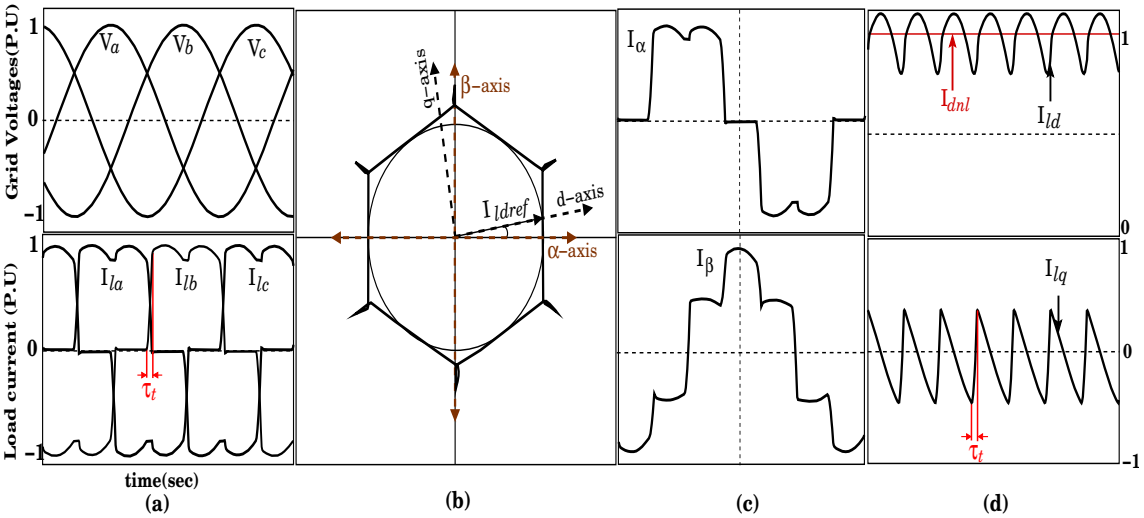

Figure 3.5: Separation of active and reactive components from the nonlinear load current (a) Three-phase grid voltages (top), and corresponding nonlinear load currents (bottom) (b) The space plot formation of the load current in stationary reference frame α-β plane (c) And corresponding reflection on α-axis (top trace) β-axis (bottom) (d) The load current realization in the synchronous reference frame with the grid voltage angle θ on d-axis (top) and q-axis (bottom).

To separate the resistive and inductive components of the load current for estimating the load network time constant, the three-phase grid voltage and the load currents are decomposed into d-axis and q-axis using a synchronous angle (θ) as:

$$\begin{aligned} V_{gd} &= \frac{2}{3}(V_{ga}cos(\omega t) + V_{gb}cos(\omega t - 120^o) + \\ &\quad V_{gc}cos(\omega t + 120^o)) = m_a V_{dc}; \\ V_{gq} &= \frac{-2}{3}(V_{ga}sin(\omega t) + V_{gb}sin(\omega t - 120^o) + \\ &\quad V_{gc}sin(\omega t + 120^o)) = 0; \end{aligned} \tag{3.4}$$

$$i_{ld} = \frac{2}{3}(i_{la}cos(\omega t) + i_{lb}cos(\omega t - 120^0) + i_{lc}cos(\omega t + 120^0)) \tag{3.5}$$

$$i_{lq} = \frac{-2}{3}(i_{la}sin(\omega t) + i_{lb}sin(\omega t - 120^0) + i_{lc}sin(\omega t + 120^0)) \tag{3.6}$$

The synchronous angle (θ) is derived from the grid voltages. In this context, the voltage v_{gd} serves as a reference point for generating the real and reactive load current components, denoted as i_{ld} and i_{lq}, respectively. The diode bridge rectifier establishes a nonlinear

circuit with the line inductance L_{NL}, as illustrated in Fig. 3.1. The characteristics of this nonlinear circuit govern the load current pattern extracted from the ACIP. The ACIP's three-phase grid voltage and nonlinear load current patterns are shown in the top and bottom traces of Fig.3.5(a), respectively. Network parameters, including loading conditions and per-phase input inductance, influence the magnitude and rise time of the current. The AC three-phase load current rise time, depicted in the bottom trace of Fig. 3.5, outlines the maximum bandwidth required for the PIFI to synthesize proper harmonic compensation. This work identifies that only two phases are conducted simultaneously under all loading conditions and form the hexagon pattern in space, as illustrated in Fig. 3.5 (b). The corresponding two-phase stationary reference frame $(\alpha - \beta)$ components and synchronous reference frame components $(d - q)$ are shown in Fig.3.5(c) and (d), respectively. In Fig. 3.5(c) and 3.5(d), it is evident that the transitional rise time is captured in the q-component (i_{lq}) within the synchronous reference frame. Therefore, i_{lq} defines the maximum angular frequency requirement of the load. Moreover, the slope of the current transition is determined by the values of the network inductance and resistance corresponding to the load power. This study establishes the relationship between the network time constant and the rise time as follows:

$$\tau_{nl} = \frac{L_{NLl_{/ph}}}{R_{nl_{/ph}}}(\text{Load network time constant}); \omega_{nl} = \frac{1}{\tau_{nl}} \tag{3.7}$$

$$\tau_r = \tau_{nl} ln9 = \frac{L_{NL}}{R_{nl}} 2.197 = \frac{2.197}{\omega_{nl}} = \frac{0.35}{f_{bw_{max}}} \tag{3.8}$$

The relation between the rise time and load network time constant defined in (3.8) is validated at different inductances and load power as shown in Fig.3.6. From Fig.3.6,

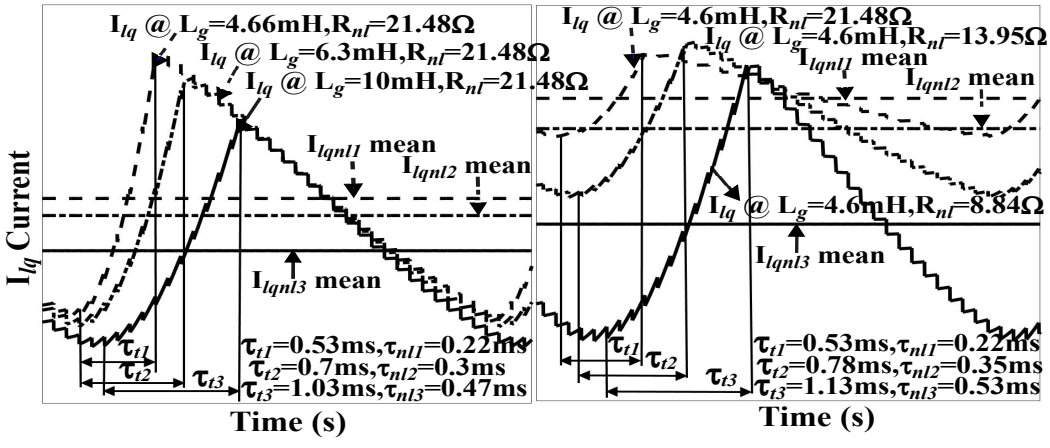

Figure 3.6: The i_{lq} variations (encapsulated load current) with change in load power(left trace) and network inductance(Right trace).

it is confirmed that the load network time constant $(\frac{L_g}{R_{nl}})$ is sufficient to realize the load bandwidth. Therefore to predict the instantaneous load angular frequency, the R_{nl} and L_g are estimated instantaneously using the synchronous grid voltage (v_{gd}) and load currents

(i_{ld} and i_{lq}) as follows:

$$R_{nl_{/ph}} = \frac{2v_{gd}i_{d_{nl}}}{3(i_{d_{nl}}^2 + i_{q_{nl}}^2)} \tag{3.9}$$

$$L_{NL_{/ph}} = \frac{v_{gd}i_{q_{nl}}}{3(i_{d_{nl}}^2 + i_{q_{nl}}^2)} \tag{3.10}$$

The signal diagram of the instantaneous R_{nl} and L_g, along with the nonlinear load angular frequency realization from SRF voltages and currents, is shown in Fig.3.7. From Fig.3.7,

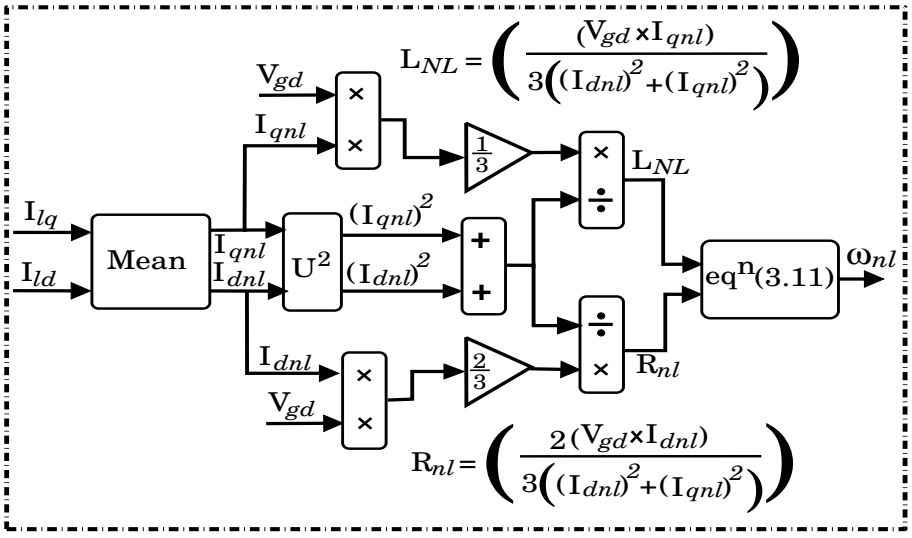

Figure 3.7: The adaptive estimation of R_{nl} and L_g for a dynamic non linear load frequency (ω_{nl}) generation.

it is to be noted that the R_{nl} and L_g are derived in an average sense by computing the average of instantaneous load currents (i_{ld}, and i_{lq}), i.e., i_{dnl} and i_{qnl} for robust parametric estimation.

3.2.1 The requirement of canceling the source power angular frequency for realizing the nonlinear load demanded bandwidth

To handle the demanded load angular frequency through an inverter, the PIFI needs to achieve a higher bandwidth than the load angular frequency. Consequently, even without a controller, ensuring the condition stated in (3.11) is essential for effectively processing nonlinear load harmonics.

$$\omega_{sys} \geq \omega_{nl} \implies \frac{R_{ac}}{L_f} \geq \frac{R_{nl}}{L_g} \implies \frac{1}{L_f P_{ac}} \geq \frac{1}{L_g P_{nl}} \tag{3.11}$$

It indicates that the plane of nonlinear load angular frequencies, characterized by various combinations of L_g and R_{nl}, can only be realized with the system angular frequencies greater than the ω_{nl} as shown in Fig.3.8. This implies that, under equal filter inductance and network inductance, the processing power of the PIFI must be lower than the demanded power of the load, as specified in (3.11) and illustrated in Fig. 3.8, especially in the absence of a controller. However, with the uncertain load and source power

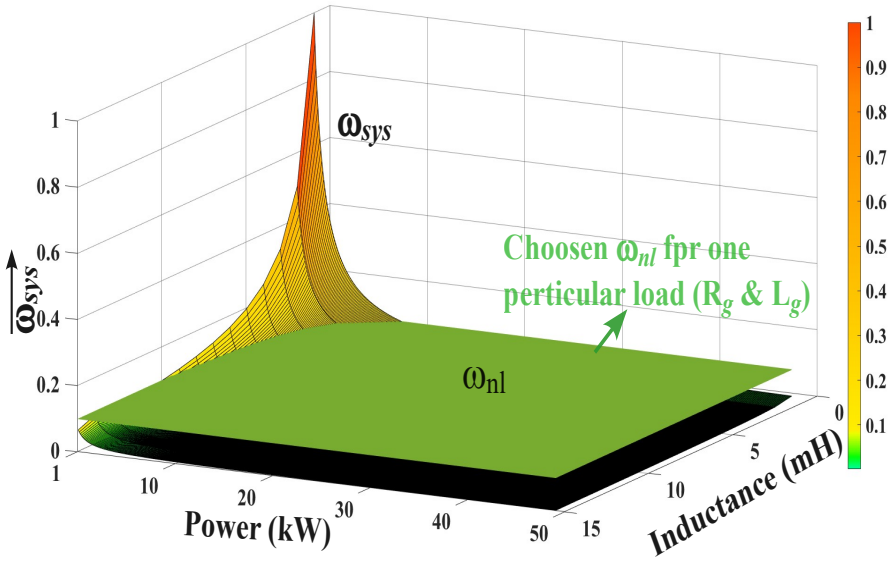

Figure 3.8: The recommended region of non linear load angular frequency (ω_{nl}) map without cancellation PIFI angular frequency (ω_{sys}) influence.

characteristics, it isn't easy to ensure the aforementioned condition (3.11). This limitation constrains the PIFI's ability to effectively track the nonlinear load harmonics. However, with appropriate PI controller closed-loop root cancellations, it is possible to steer the complete closed-loop response as per the required load angular frequency (bandwidth). To illustrate the impact of system poles on the closed-loop response, Fig. 3.9 displays the trajectory of ω_{sys} with random controller root placement. Additionally, Fig. 3.10 shows the concurred root placement with varied filter inductances and resistances, equivalent to grid-injected power. From Fig. 3.9 and Fig. 3.10, it's clear that as inductance

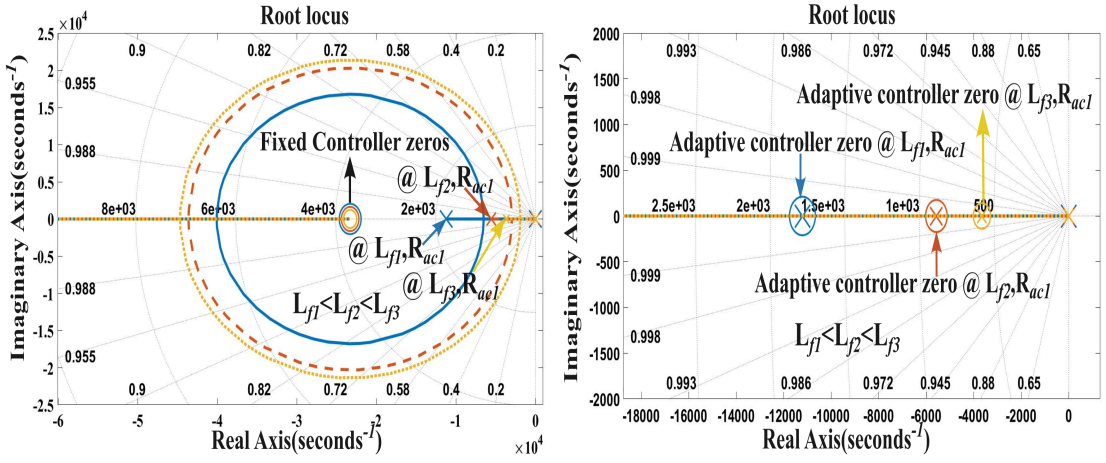

Figure 3.9: The PIFIs angular frequency trajectory with the arbitrary placement of controller root (left) and root placement precisely at the system angular frequency (right) with varying filter inductance values.

increases and resistance decreases (indicating higher grid-injected power), more power oscillations are observed. Nevertheless, the controller can adjust these oscillations through adaptive pole cancellation. By leveraging the concept of adaptive pole cancellation, the

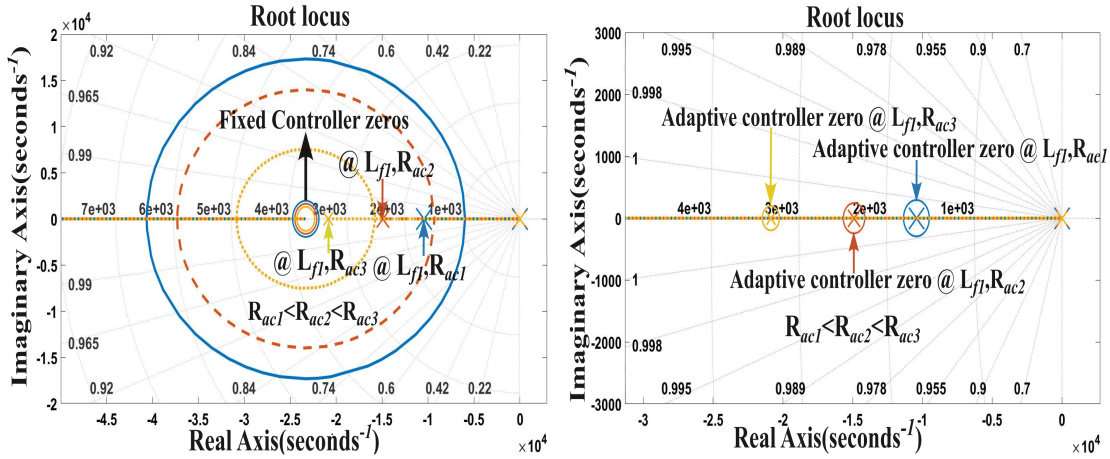

Figure 3.10: The PIFIs angular frequency trajectory with the arbitrary placement of controller root (left) and root placement precisely at the system angular frequency (right) at various injected solar power.

PIFI controller is designed to shape the closed-loop response by the demanded load angular frequency, as detailed in the following section.

3.2.2 The proposed PIFI's closed-loop controller design with rolling gain adjustment mechanism

To accomplish the desired dynamic response to process the load demanded harmonics with the identified filter inductance, the synchronous reference frame (SRF) based dynamic controller gain adjustment is demonstrated in this section. The proposed PIFI controller must act to synthesize the load-demanded harmonics along with the simultaneous solar power injection. Therefore, the reference to the controller is derived using the measured information of instantaneous solar power and the instantaneous currents processing by the load as:

$$\begin{bmatrix} I_{dref} \\ I_{qref} \end{bmatrix} = \begin{bmatrix} I_{dh} + I_d^{(MPPT)} \\ I_{qh} + I_q^{(user)} \end{bmatrix} \tag{3.12}$$

Here $I_{dh} = (I_{ld} - Avg(I_{ld}))$ that keep I_{dref} persistent with the load current ripple information in d-axis. $I_d^{(MPPT)}$ represents the real current reference extracted using the maximum power point tracking algorithm. Similarly, the I_{qh} and $I_q^{(user)}$ represent the q-component of nonlinear load current and user-defined reactive component, respectively. With the defined I_{dref} and I_{qref}, the PIFI's closed-loop transfer function can be derived by observing the rate of change in current reference quantities as:

$$\frac{dI_{dref}}{dt} = \frac{v_{gd}}{L_f} - \frac{R_{ac}}{L_f} I_{dref} + \omega . I_{qref} \tag{3.13}$$

$$\frac{dI_{qref}}{dt} = \frac{v_{gq}}{L_f} - \frac{R_{ac}}{L_f} I_{qref} - \omega . I_{dref} \tag{3.14}$$

The (3.13) and (3.14) can be written classic state space representation ($\dot{x} = Ax + Bu$ and $y = Cx + Du$) as:

$$\begin{bmatrix} \frac{dI_{dref}}{dt} \\ \frac{dI_{qref}}{dt} \end{bmatrix} = \begin{bmatrix} \frac{-R_{ac}}{L_f} & \omega \\ -\omega & \frac{-R_{ac}}{L_f} \end{bmatrix} \begin{bmatrix} I_{dref} \\ I_{qref} \end{bmatrix} + \begin{bmatrix} \frac{V_{dc}}{L_f} & 0 \\ 0 & \frac{V_{dc}}{L_f} \end{bmatrix} \begin{bmatrix} m_d \\ m_q \end{bmatrix} \tag{3.15}$$

$$\begin{bmatrix} I_{fd} \\ I_{fq} \end{bmatrix} = \begin{bmatrix} 1 & 0 \\ 0 & 1 \end{bmatrix} \begin{bmatrix} I_{dref} \\ I_{qref} \end{bmatrix} \tag{3.16}$$

From the state space equation, the transfer function can be derived in the form of $Y(s) = (C(SI - A)^{-1}B + D)$ as:

$$\begin{bmatrix} I_{fd} \\ I_{fq} \end{bmatrix} = \begin{bmatrix} G_{11} & G_{12} \\ G_{21} & G_{22} \end{bmatrix} \begin{bmatrix} m_d \\ m_q \end{bmatrix} V_{dc} \tag{3.17}$$

The derived G_{11} and G_{22} represents the $d-$ loop and $q-$ loop plant transfer functions as shown in Fig.3.11. The plant (PIFI) transfer function can be described as

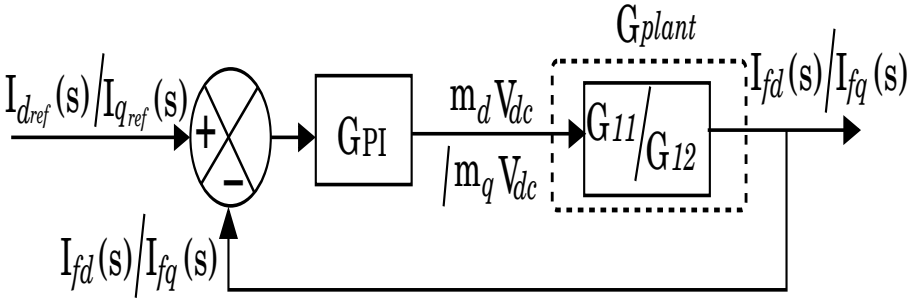

Figure 3.11: The signal flow diagram consolidated plant model along with the controller.

$$G_{11} = G_{22} = \frac{(sL_f + R_{ac})(V_{dc})}{s^2L_f^2 + 2L_fR_{ac}s + R_{ac}^2 + \underbrace{(\omega L_f)^2}_{\approx 0}} \tag{3.18}$$

By neglecting the ωL_f, the closed-loop d-axis and q-axis closed-loop transfer function can be defined as :

$$G_{cl} = \frac{(K_ps + K_I)/L_f}{s^2 + \frac{(R_{ac}+K_P)}{L}s + \frac{K_I}{L_f}} \tag{3.19}$$

To derive the desired closed bandwidth, the roots of the characteristic equation are defined as:

$$\omega_1 + \omega_2 = \frac{R_{ac} + K_P}{L_f} \tag{3.20}$$

$$\omega_1.\omega_2 = K_I/L_f \tag{3.21}$$

By equating ω_1 to ω_{sys} $(= \frac{R_{ac}}{L_f})$ through adaptive estimation based on the available solar

power (I_{dref}) described in Fig.3.3, the controller gains can be written as:

$$K_P = \omega_2 L_f; K_I = \omega_2 R_{ac} \tag{3.22}$$

By substituting (3.22) in (3.19), the closed-loop transfer function is reduced to

$$G_{cl} = \frac{\omega_2}{s + \omega_2} \tag{3.23}$$

The (3.23) indicates that with adaptive estimation and cancellation of ω_{sys} through controller roots (ω_1) realizes the closed loop bandwidth equal to ω_2 as shown in Fig.3.12. The PIFI adaptively synthesizes the nonlinear load bandwidth by making ω_2 equal to

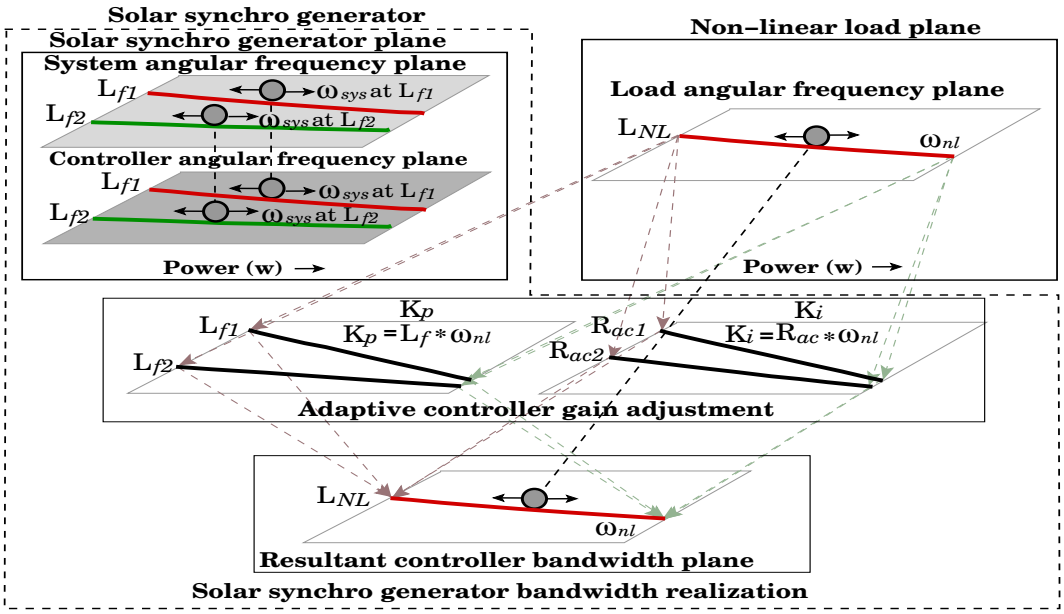

Figure 3.12: The dynamic system pole cancellation technique for an adaptive rolling system bandwidth adjustment in synchronous with the nonlinear load variations.

ω_{nl} through a load angular frequency estimation. As it is shown in Fig.3.12, one of the closed-loop controller roots (ω_1) adaptively tracks the ω_{sys}. It ensures the closed loop response follows the nonlinear load angular frequency (ω_{nl}) by automatically adjusting the controller gains K_P and K_I. The signal flow diagram of the controller gain (K_P and K_I) realization by adaptive estimation of ω_{sys} and ω_{nl} and corresponding gating pulse realization for the three-phase inverter is shown in Fig.3.13.

3.2.3 The proposed rolling controller gain adjustment in digital domain

The proposed rolling controller gain adjustment mechanism is implemented in the digital controller by transforming S-domain transfer functions to Z-domain through a bilinear transformation using

$$s = \frac{2}{T_s} \frac{1 - z^{-1}}{1 + z^{-1}} \tag{3.24}$$

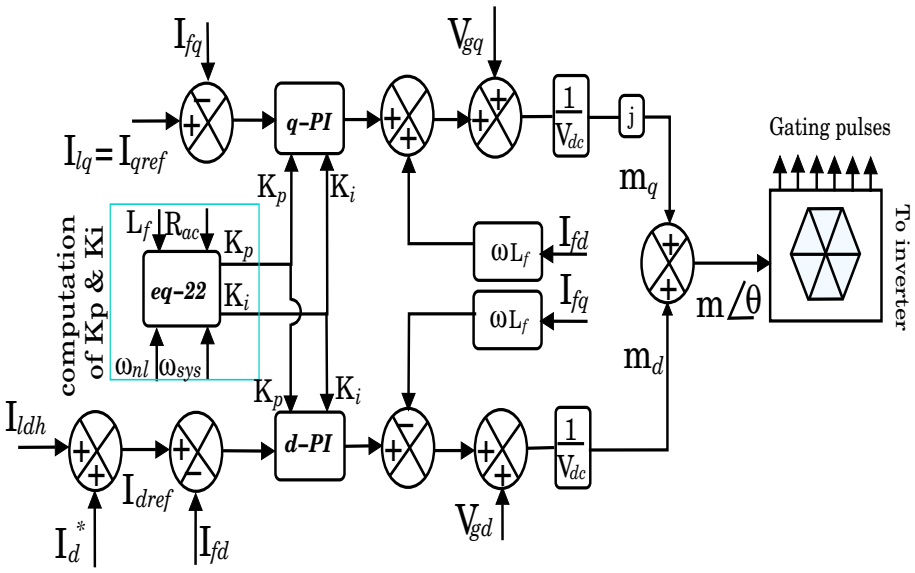

Figure 3.13: The signal flow diagram of PIFI switching pulses synthesis with adaptive controller gain adjustment mechanism.

where T_s is a sampling time , $z = e^{sT}$ and s=j ω. Through bilinear transformation, the closed loop transfer function mentioned in (3.19) can be written in the z-domain as:

$$G_{zcl} = \frac{(K_P T_s^2 + 2K_P T_s)Z^2 + 2K_I T_s^2 z - 2T_s K_P}{az^2 + bz + c} \tag{3.25}$$

$$G_{zcl} = \frac{\frac{(K_P T_s^2 + 2K_P T_s) + 2K_I T_s^2 z^{-1} - 2T_s K_P z^{-2}}{a}}{1 + \frac{b}{a}z^{-1} + \frac{c}{a}z^{-2}} \tag{3.26}$$

where $a = (T_s^2 K_P + 2R_{ac}T_s + 2K_P T_s + 4L_f)$, $b = (2K_I T_s^2 - 8L_f)$ and $c = (T_s^2 K_I - 2R_{ac}T_s - 2K_P T_s + 4L_f)$. With the closed-loop controller root adjustment adaptive to the system and load angular frequency described in the preceding section, the closed-loop transfer function simplifies to:

$$G_{zcl} = \frac{\omega_2 (z+1) T_s}{2(z-1) + \omega_2 (z+1) T_s} \tag{3.27}$$

As (3.27) reaffirms that closed loop response adaptively realizes ω_2 (equal to ω_{nl}) with the proper adjustment of controller gains in Z-domain. However, in the z-domain, the transfer function response is defined by the sampling time (T_s) and switching frequency (ω_{sw}). Therefore the close concurrence of the closed-loop control response with the proposed gain adjustment method is shown in Fig.3.14 in s-domain ((3.19) (3.23)) and z-domain ((3.26),(3.27)) at T_s =$1e^{-5}, 1e^{-6}$ and f_{sw} =10kHz. From Fig.3.14, it is evident that the Z-domain response magnitude and phase match closely with the s-domain response at defined T_s. The corresponding load i_q tracking by the closed-loop control response with the adjusted controller gains at T_s=$1e^{-5}$ and $1e^{-6}$ is shown in Fig.3.15. It is evident from Fig.3.15, in the digital domain, i_q tracks the i_{qref} with the ripple of switching frequency, indicating the enhanced tracking performance at the higher switching frequencies.

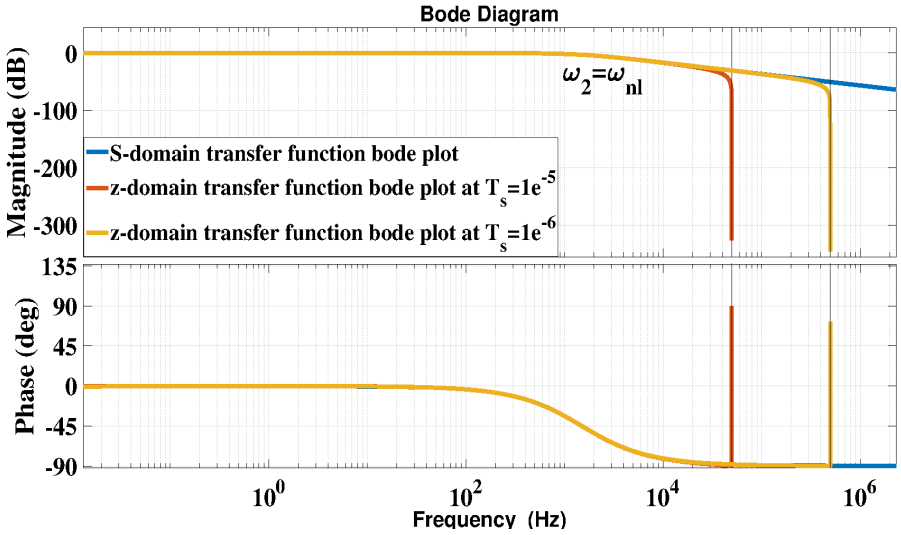

Figure 3.14: The magnitude and phase plots of the closed loop transfer function derived in s-domain (3.19) (3.23) and Z-domain (3.26),(3.27).

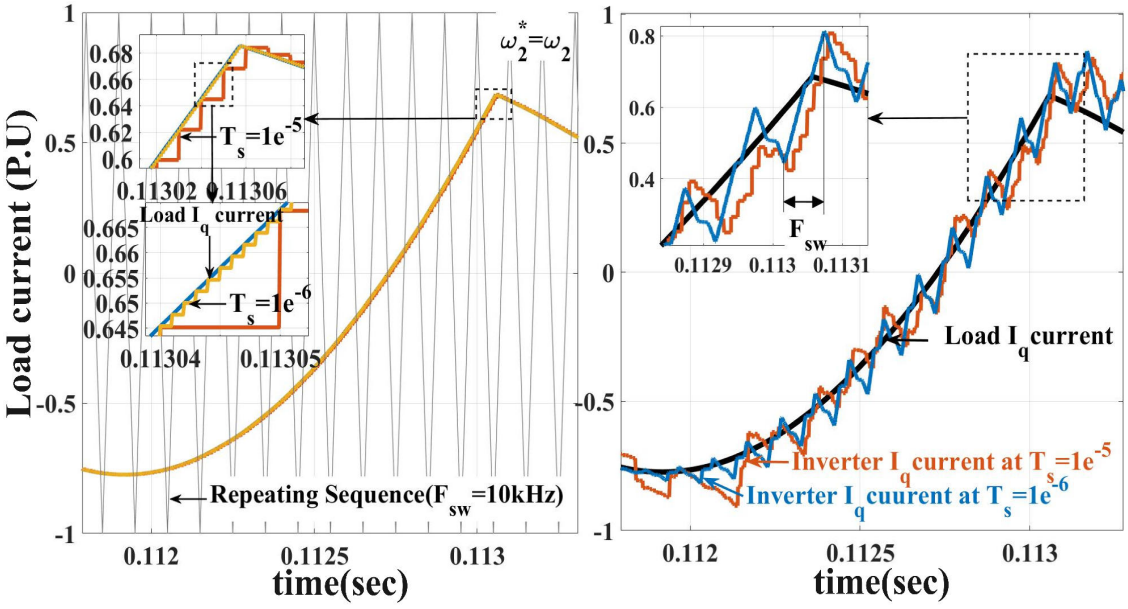

Figure 3.15: The load current rise time reference sampling at the rate of $T_s = 1e^{-5}$ and $1e^{-6}$ along with switching frequency (left trace), The closed loop response load current (i_q) tracking in Z-domain with $T_s = 1e^{-5}$ and $1e^{-6}$ (right trace).

3.3 Results and Discussion

The PIFI prototype is developed in the lab with three-phase inverters fed from the solar emulator interfaced with the grid. The nonlinear load characteristics are mimicked using a diode bridge rectifier connected at the ACIP, as shown in Fig.3.16. The operating parameters of the hardware prototype are tabulated in Table-4.2. The proposed rolling gain algorithm is implemented on the DSP C2000 (F28379D) by computing all digital delays.

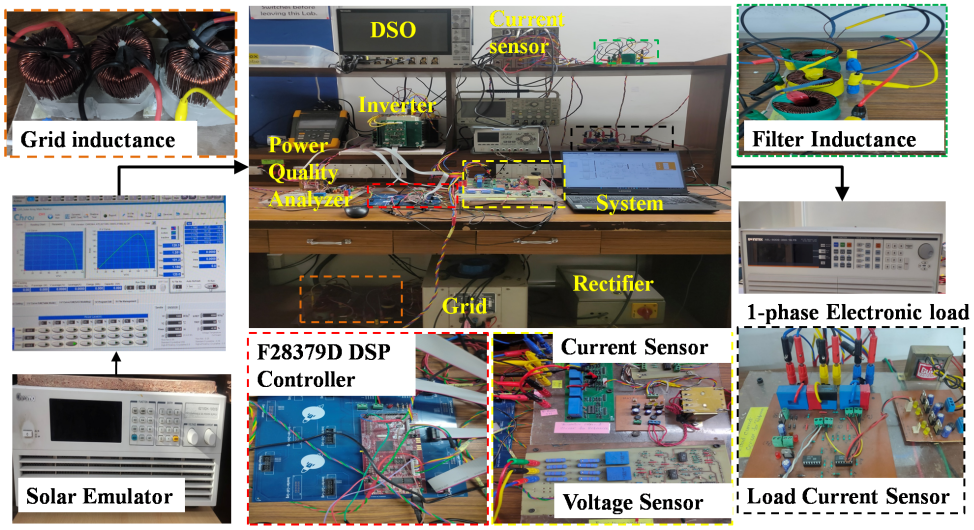

Figure 3.16: The experimental setup for validating the proposed rolling gain adjustment mechanism.

Table 3.1: Experimental operating parameter of solar synchro active power filter

Parameters		rating
Load Power (Max)	P_L	1500 W
Load current	I_0	5.8 A
Non-linear load resistance	R_{nl}	17.5Ω
Load inductance	L_{NL}	3.2 mH
DC voltage	V_{dc}	400 V
Switching Frequency	(F_{sw})	10 kHz
filter inductance	L_f	3.2 mH
sampling time	T_S	$1e^{-5}$
Parametric delay computation		delay
Sensor	t_{sensor}	40μsec
ADC	t_{ADC}	0.58μ sec
Controller	$t_{controller}$	52μsec
switch (ON)	t_{on}	0.15μsec
switch (OFF)	t_{off}	0.37μsec

3.3.1 The rolling gain adjustment adaptive to load power variations at constant PV power

In the rolling gain adjustment process, for computing the nonlinear load angular frequency (ω_2), the equivalent load resistance (R_{nl}) (correspond to the load drawn power) and grid inductance is computed using (3.9) and (3.10). The instantaneous load resistance (R_{nl}) estimation from the measured load current after computing the synchronous quantities is depicted in Fig.3.17.

With an adaptive estimation of R_{nl} at different load powers and by keeping source (PV) power minimum, the corresponding variations of the ω_{nl} are shown in Fig.3.18. From Fig.3.18, it is also evident that at (constant) minimum source power (ω_{sys} is maintained constant) and by adaptively making the estimated ω_{nl} equal to ω_2 controller

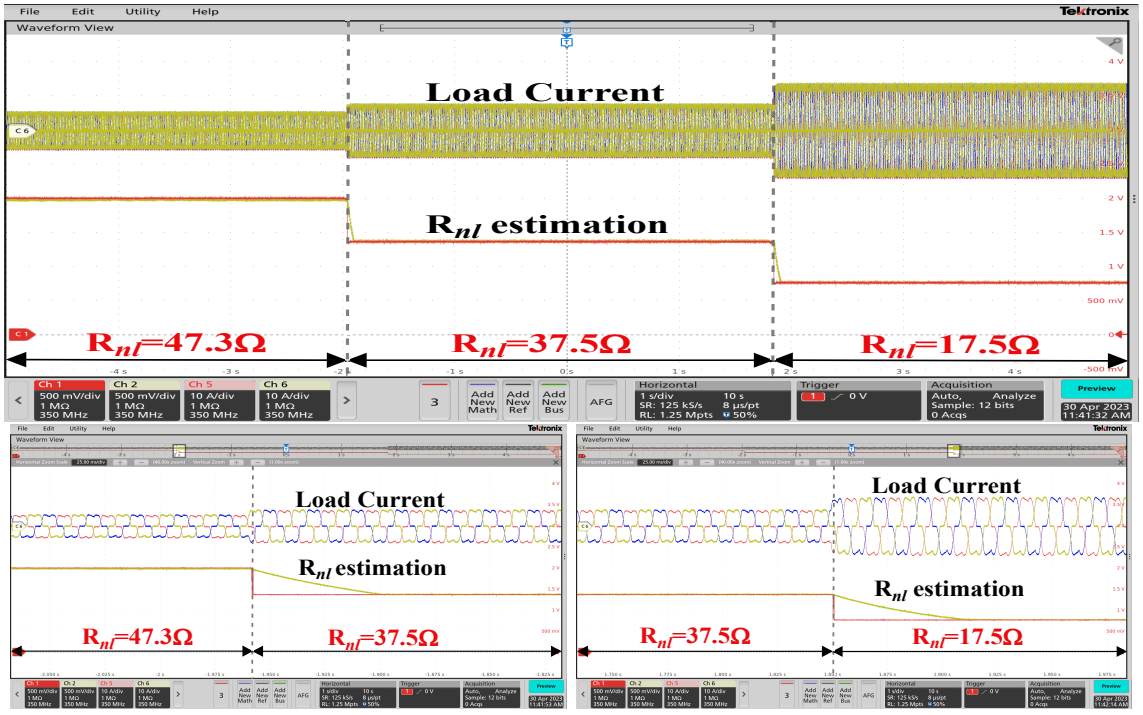

Figure 3.17: The adaptive estimation of load equivalent resistance (R_{nl}) (bottom trace (x-axis:1sec/div, Y-axis:0.5V/div)) with the change in load current (top trace x-axis:25msec/div Y-axis:10A/div). The zoomed portion of the R_{nl} with the power variation from 550W to 760W (bottom left figure x-axis:25msec) and 760W to 1500 W (bottom right figure X:25msec).

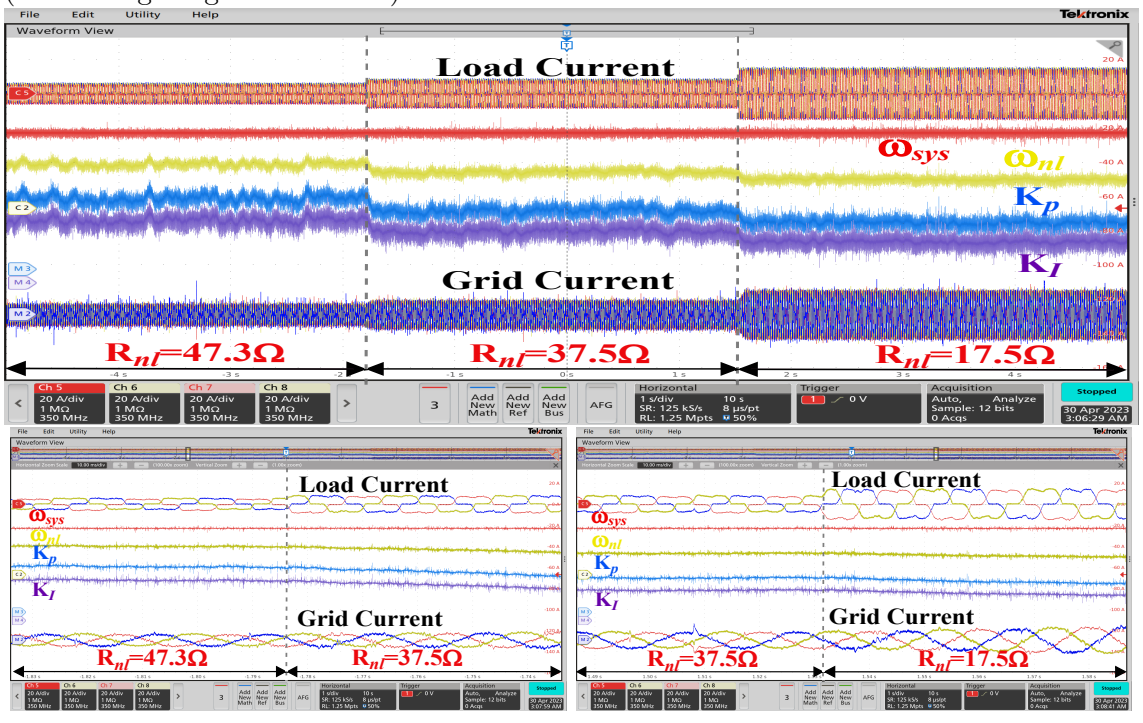

Figure 3.18: The three-phase load current (top trace x:1sec/div Y:20A/div), dynamic variations of ω_{nl}, K_P, and K_I (middle traces Y:1V/div) and corresponding three-phase grid currents (bottom trace Y:20A/div) for the load power variations from 550W to 760W (The zoomed portion bottom left x:10msec/div) and from 760W to 1500W (The zoomed portion bottom right figure).

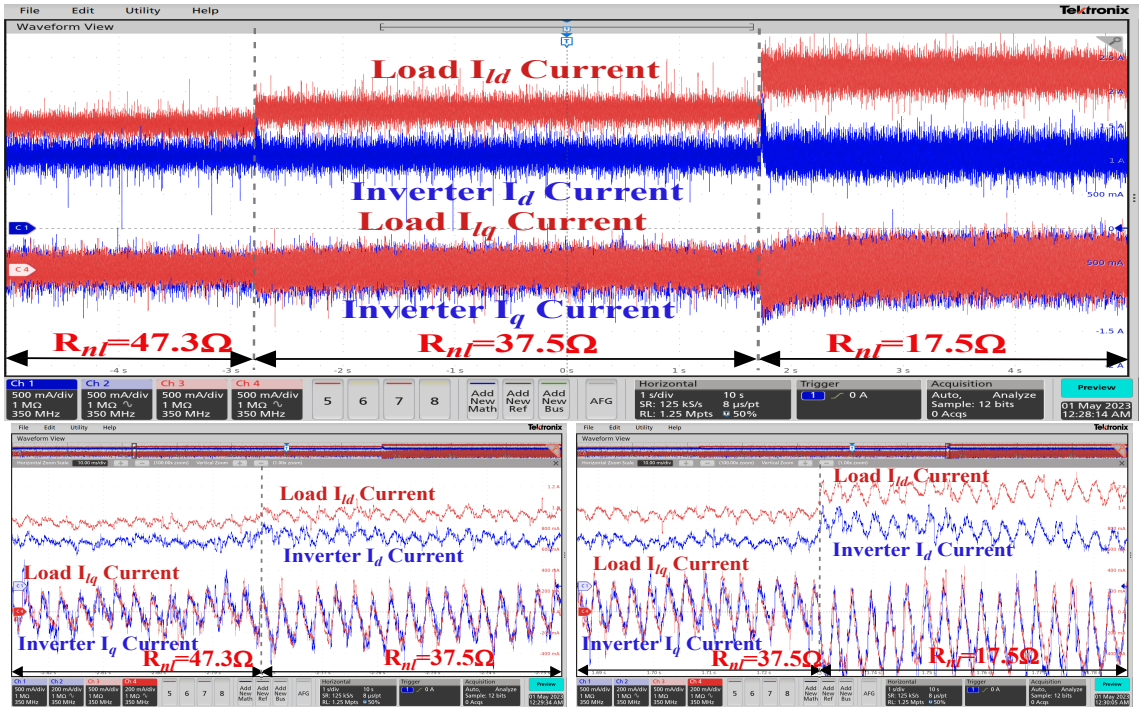

Figure 3.19: The nonlinear load and PIFI's i_d (top two traces x:1sec/div Y:0.5A/div) i_q profiles (bottom overlapping traces x-axis:1sec/div Y-axis:0.5A/div). The corresponding zoomed portion depicting load power changes from 550W to 760W (bottom left figure x:10msec) and 760W to 1500W (bottom right figure).

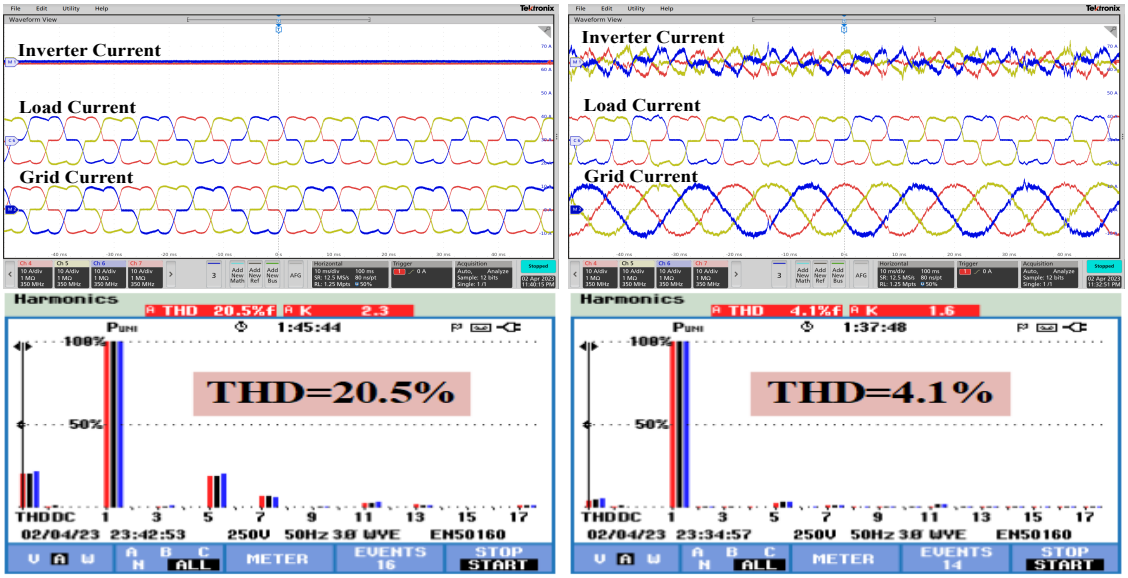

Figure 3.20: The three-phase inverter currents (top trace), three-phase load current (middle trace), and three-phase grid currents (bottom trace) along with the harmonic spectrum without harmonic compensation (left figure) and with harmonic compensation (right figure).

acts to compensate grid harmonics at all nonlinear loading conditions. Since the load current harmonics are captured in synchronous quantity, the adaptive tracking of the load synchronous quantities (i_d, i_q) by the PIFI is demonstrated in Fig.3.19. The close occurrence of nonlinear load and PIFI reactive components assert the appropriate

harmonic support by the PIFI at different loading conditions. At a minimum source power, the PIFI ensures the grid dynamic harmonic compensation as evident through %THD shaping from 20.5% to 4.1%. It confirms that the PIFI acts as a harmonic compensator, and the efficacy of shaping the grid harmonics at different power levels (varied in three steps from 550W to 700 W and 700 W to 1500 W) is demonstrated through experimental results depicted in Fig.3.21. At every load change, the controller gains are adjusted to shape the grid current by processing the load demanded harmonics through PIFI, as shown in Fig.3.21.

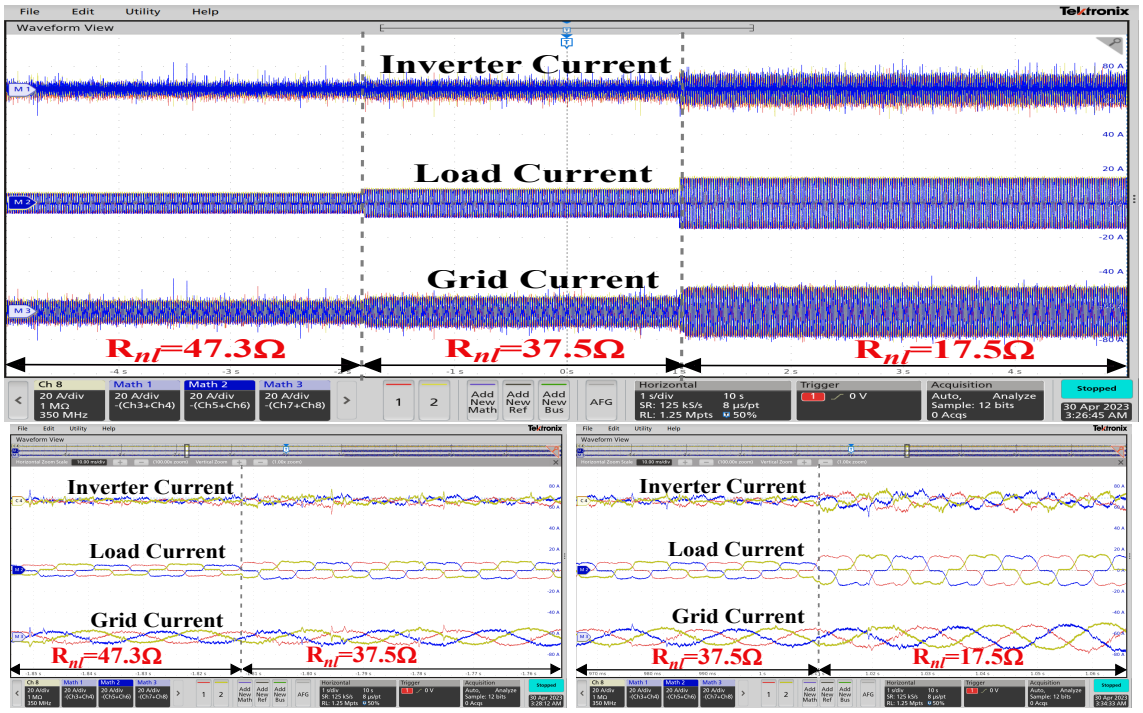

Figure 3.21: The solar PV maximum power tracking and its variations (top figure) and corresponding PIFI's three-phase current (second trace x:1sec/div Y:20A/div), the three-phase load current (Third trace Y:20A/div) and grid current (bottom trace Y:20A/div). The corresponding zoomed portion shows the load power variation from 550W to 760W (bottom left figure x:10msec) and 760W to 1500W (bottom right figure).

3.3.2 The rolling gain adjustment adaptive to PV power variations at constant load power

However, with the available PV power, the PIFI must act to inject the active power with the simultaneous correction of load harmonics. With the maximum derived source available, power information is extracted through a dedicated MPP algorithm (perturb and observe method) for deriving the instantaneous ω_{sys} information. With the instantaneous ω_{sys}, the proposed rolling gain mechanism adjusts the controller gain by changing closed loop root (ω_1) adaptive with ω_{sys} as shown in Fig.3.22.

As the load power is made constant, the angular frequency corresponding to the load network is constant for all the source variations, as shown in Fig.3.22. With updated controller gains following the source power variations, the load and PIFI SRF current

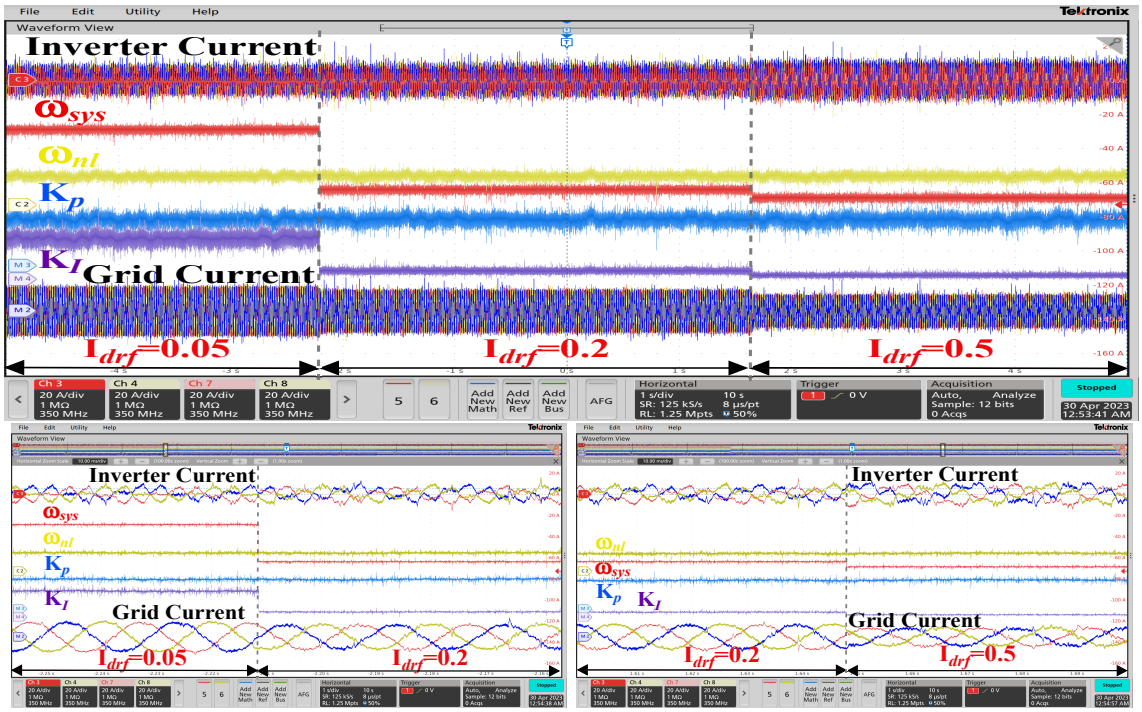

Figure 3.22: The three-phase inverter current (top trace x:1sec/div Y:20A/div), dynamic variations of ω_{sys}, and K_I (middle traces Y-axis:1V/div) and corresponding three-phase grid currents (bottom trace Y:20A/div) for the PIFI power variations from 75W to 300W (The zoomed portion bottom left x:10msec/div) and from 300W to 750W (The zoomed portion bottom right figure).

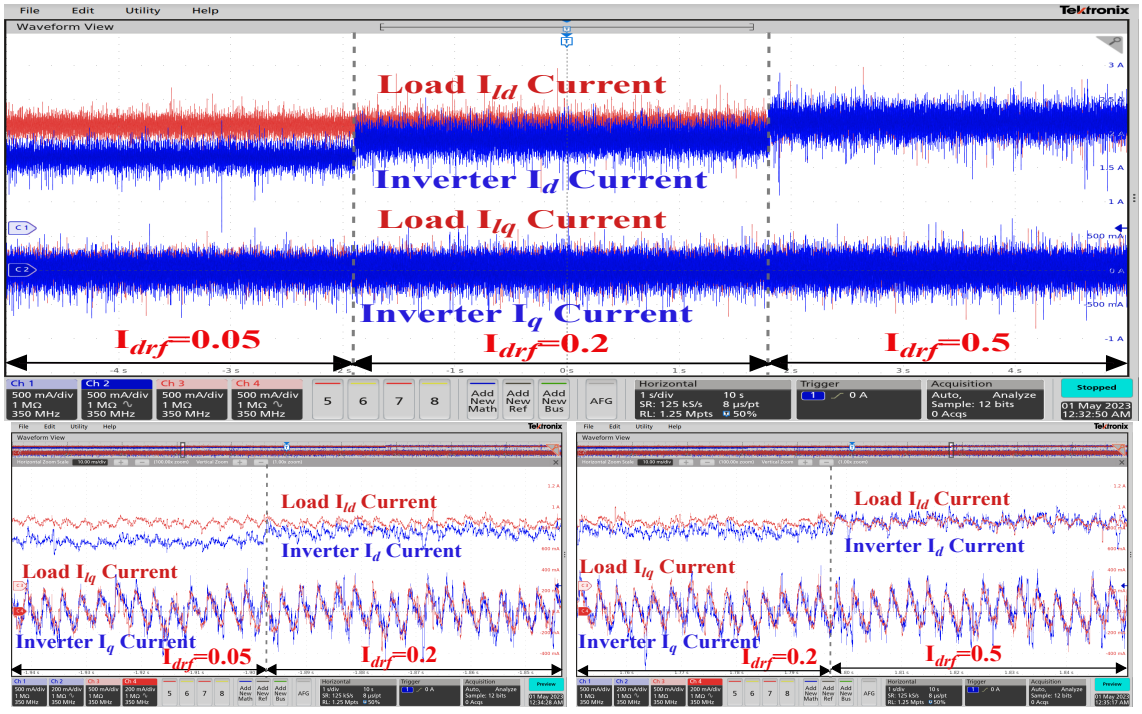

Figure 3.23: The nonlinear load and PIFI's i_d (top two traces x:1sec/div Y:0.5A/div) i_q profiles (bottom overlapping traces x-axis:1sec/div Y-axis:0.5A/div). The corresponding zoomed portion depicts PIFI power changes from 75W to 300W (bottom left figure x:10msec) and 300W to 750W (bottom right figure).

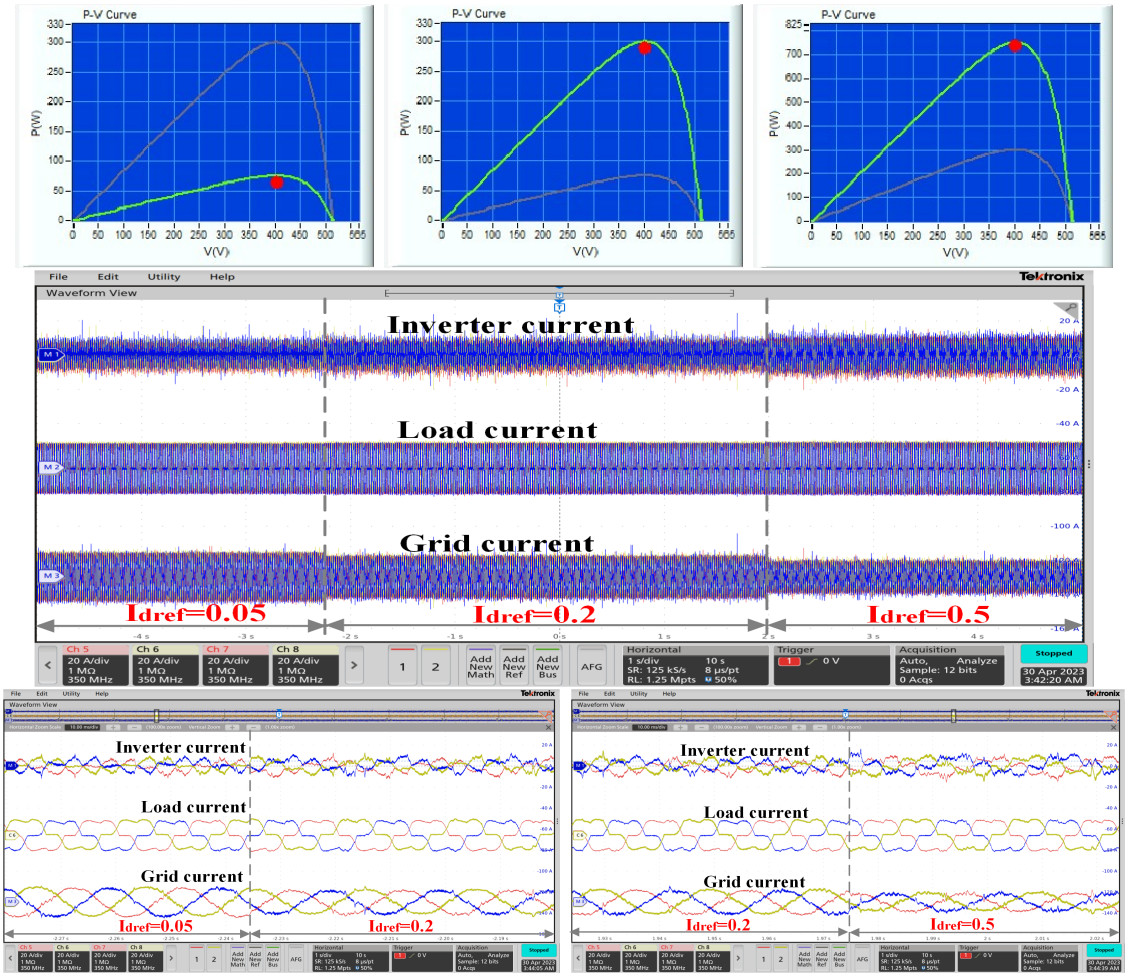

Figure 3.24: The PIFI's three-phase inverter current (top trace x:1sec/div Y:20A/div), the three-phase load current (middle trace Y:20A/div) and grid current (bottom trace Y:20A/div). The corresponding zoomed portion shows the PIFI power variation from 75W to 300W (bottom left figure x:10msec) and 300W to 750W (bottom right figure).

parameters (i_d and i_q) are observed, as shown in Fig.3.23. From Fig.3.23, it is evident that the PIFI's i_q is tracking the load i_q closely at all source power variations, confirming the dynamic controller bandwidth realization to process the load demanded harmonics. Similarly, the PIFI's and load's i_d profile indicates the available PV power injection to the load network at all irradiance conditions. With the adaptive estimation of ω_{sys} and corresponding adjusted gains, the source DC power injection to the AC network with the appropriate harmonic correction is demonstrated by showing the experimental results of three-phase PIFI, load, and grid current, respectively. As the MPP algorithm is used to extract the maximum source power, the corresponding maximum power tracking is shown in the top traces of Fig.3.24. From the inverter three-phase current and the grid current profile shown in Fig.3.24, it is evident that the rolling gain adjustment is superior in shaping the grid current with simultaneous injection of active power (75 W, 300 W, and 750 W).

Further, to show the efficacy of the proposed rolling gain adjustment mechanism adaptability at different modes of operation, the source power and load power are adjusted

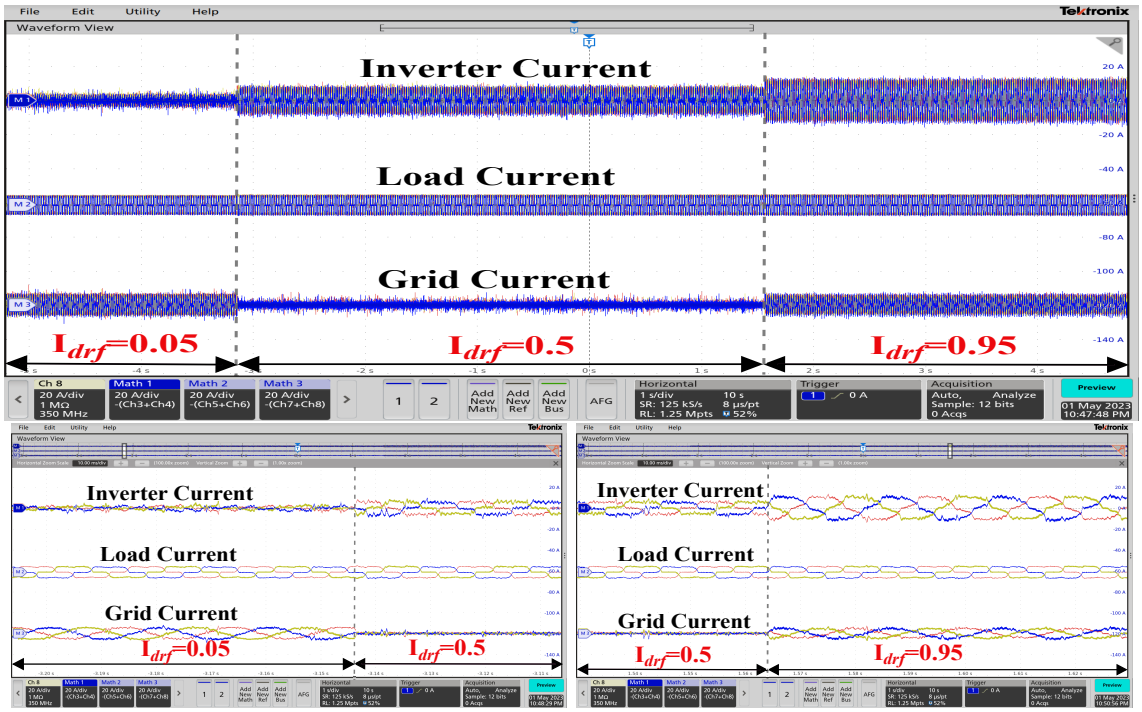

Figure 3.25: The PIFI's three-phase inverter current (top trace x:1sec/div Y:20A/div), the three-phase load current (middle trace Y:20A/div) and grid current (bottom trace Y:20A/div). The corresponding zoomed portion shows the PIFI power variation from 75W to 750W (bottom left figure x-axis:10msec) and 750W to 1500W (bottom right figure).

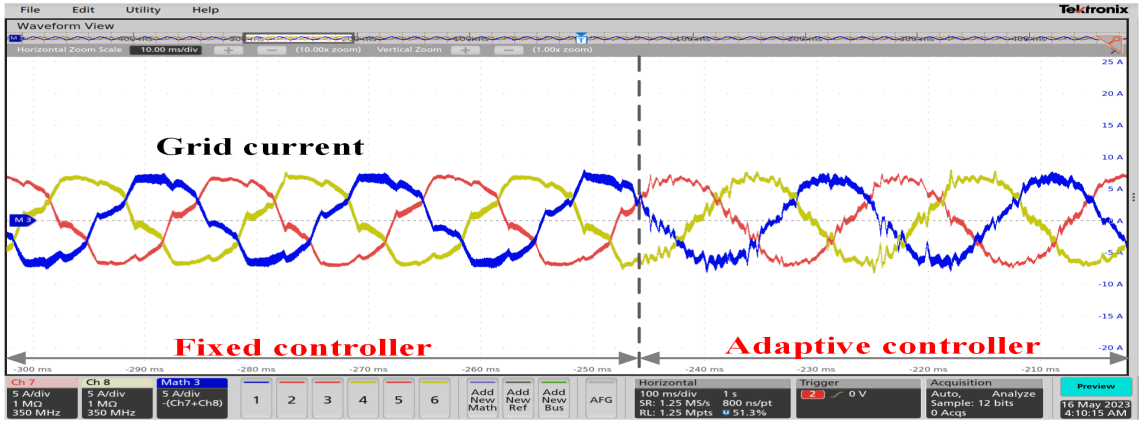

Figure 3.26: The dynamic three-phase grid current behavior with the changeover from the fixed controller to proposed adaptive gain adjustment (X:10msec/div Y:10A/div).

accordingly to derive the grid drawing (load power > source power), compensation mode (load power = source power) and grid injected mode (load power < source power) as shown in Fig.3.25. The zoomed portions of Fig.3.25 depict the superiority of the proposed controller in grid drawing, compensation, and grid-injection modes. As it is shown in Fig.3.25, in grid injection mode, the three-phase current changes its polarity accordingly, and only load-demanded harmonics are synthesized by the PIFI, making the PIFI inject pure sine wave to the grid. Finally, to evaluate the superiority of the proposed controller gain adjustment over the conventional fixed controller gain in correcting grid harmonics by allowing the controller gains adjustment through the proposed algorithm at 245 ms

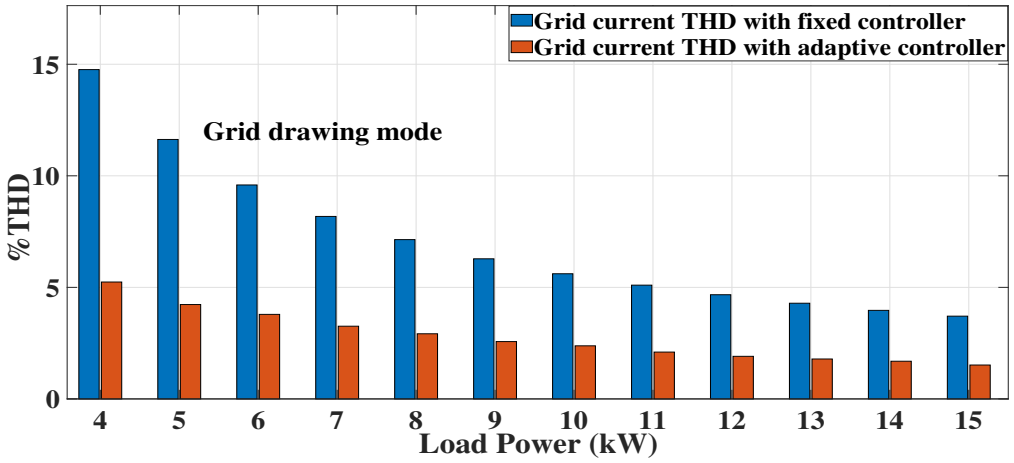

(a) By varying the load power(P_L) and keeping source power(P_{PIFI}) fixed.

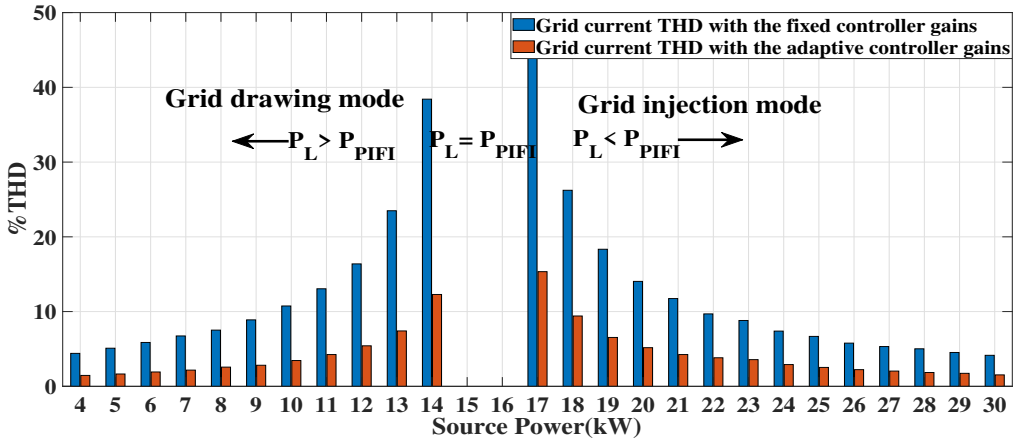

(b) By varying the source power(P_{PIFI}) and keeping load power($P_L = 15kW$) fixed.

Figure 3.27: %THD comparison with fixed controller gains and the proposed rolling gain adjustment.

is demonstrated as shown in Fig.3.26. Similarly, the proposed adaptive controller gain adjustment's efficacy in shaping %THD at different PV power and load powers is shown in Fig.3.27. The comparison is made by keeping the fixed controller designed for the rated solar PV power (normal practice). The adaptive control is varied as per the procedure described in this paper. In both cases, the % THD is compared by varying the load Power from 4 kW to 15 kW as shown in Fig.3.27(a) and by varying the source power from 4kW to 15 kW as depicted in Fig.3.27(b). The three modes are demonstrated with source power by maintaining the load power at 15kW as shown in Fig.3.27(b). The grid current is minimum at load power equal to source power. Thus, the %THD can not be defined otherwise; at all source and power variations, the %THD maintained under 5% (approx) is well justified compared to fixed controller gains.

3.4 Conclusion

This work proposes the solar synchro generator's rolling controller gain adjustment mechanism for simultaneous injection of nonlinear load demanded harmonics and the

PV active power. It is identified that the nonlinear load current rise time (defines the bandwidth) is equal to 2.197 times the network time constant at all loading conditions. Therefore, realizing PIFI closed-loop bandwidth equal to the nonlinear load angular frequency ensures that the demanded load transition rise time is accomplished. Thus to realize the load demanded bandwidth through the controller, the source and load angular frequency variations are predicted. With the help of predicted source and load dynamics, the rolling controller gain adjustment mechanism is demonstrated to realize the closed loop bandwidth equal to the load demanded angular frequency. With the adaptive PI controller gain adjustment, the PIFI tracks the load demanded harmonics irrespective of active power injection, indicating the enhanced grid power quality in both grid power drawing and injection modes of operations. The multi-functionalities of simultaneous active power injection with harmonic current shaping feature make PIFI more attractive in charging station infrastructure due to ensured grid current harmonics below 5% as per IEEE standards.

Chapter 4

A Solar Series Grid Following Harmonic Compensator with Enhanced Grid Current Shaping and Active Power Injection Capability

4.1 The Solar Active Power Cum Harmonic Injector(SAPCHI)

The proposed grid-interfaced solar series inverter-based harmonic compensator shown in Fig. 4.1 aims to compensate for the nonlinear load's current harmonics that shape the grid-injected power quality at different active power injections. As shown in Fig.

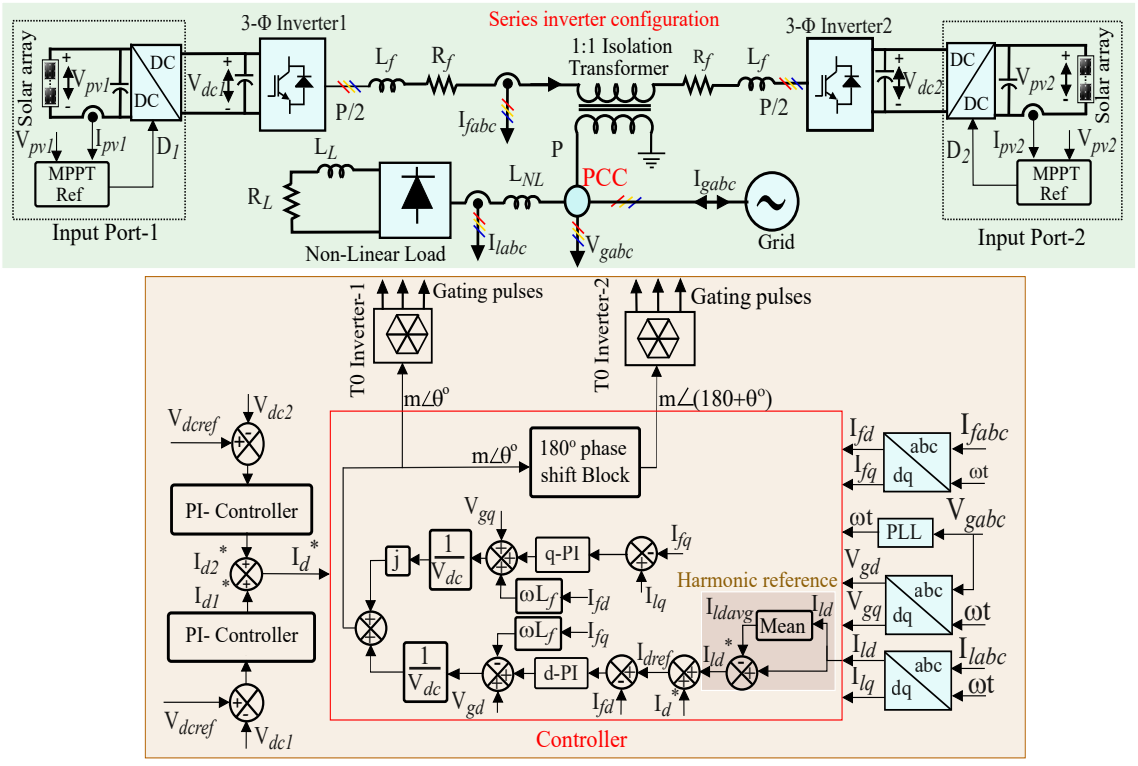

Figure 4.1: The circuit diagram of proposed solar series active power cum harmonic injector with closed-loop control

4.1, in the series configuration, the two three-phase inverters are connected back to back through an isolation transformer that brings the load and grid in series with the inverters. The isolation transformer provides the isolation between grid/nonlinear-load and inverter circuits that arrest the circulating currents through the power and sensor network. The L_f and L_g denote the additional filter inductance apart from the transformer leakage inductance and nonlinear load per phase line inductance, respectively. The design procedure for L_f computation based on the load network time constant (τ_n) is elaborated in Section-4.2. Considering the source and load network impedance, a dedicated closed-loop control methodology is developed for the series inverter configuration as shown in Fig.4.1 for simultaneous grid harmonic shaping and active power injection. In the closed-loop control, the combined reference for the solar inverters from the solar input ports is explained in section-4.3. The implementation of impedance-based control methodology is demonstrated in Section-4.4.

4.1.1 The series inverter switching sequence for virtual load frequency doubling

The proposed series inverter configuration having two inverters can switch independently between eight switching locations (varying from 1(100) to 8(000) for inverter-1 and 1'(100) to 8'(000) for inverter-2) as shown in Fig. 4.2 resulting 64 switching combinations.

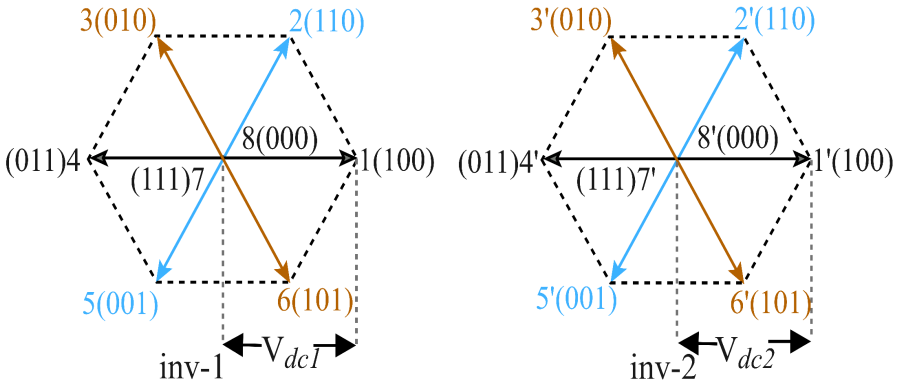

Figure 4.2: Switching hexagon of individual inverters in series inverter topology.

The realization of the switching pattern from the reference phase voltages for both the inverters in two sampling intervals is shown in Fig. 4.3. The individual inverters experience four switching transitions each (0,1,6,7 by inverter-1; 7',4',3',0' by inverter-2), while the combined series inverters produce eight switching transitions (00', 03',13', 63',64',67',77') across the filter. It indicates the passive filter experiences double the switching frequency of each inverter. Doubling the switching frequency in the series inverter helps to reduce the filter size compared to the parallel inverter-based harmonic compensator. The parallel inverter topology produces the same switching frequency as the individual single inverter across the filter, as mentioned in [47]. Apart from the switching frequency, the other advantage of the series inverter is that it shares power in terms of voltage, unlike parallel inverter topology. The voltage synthesized across the load with two inverter voltages can

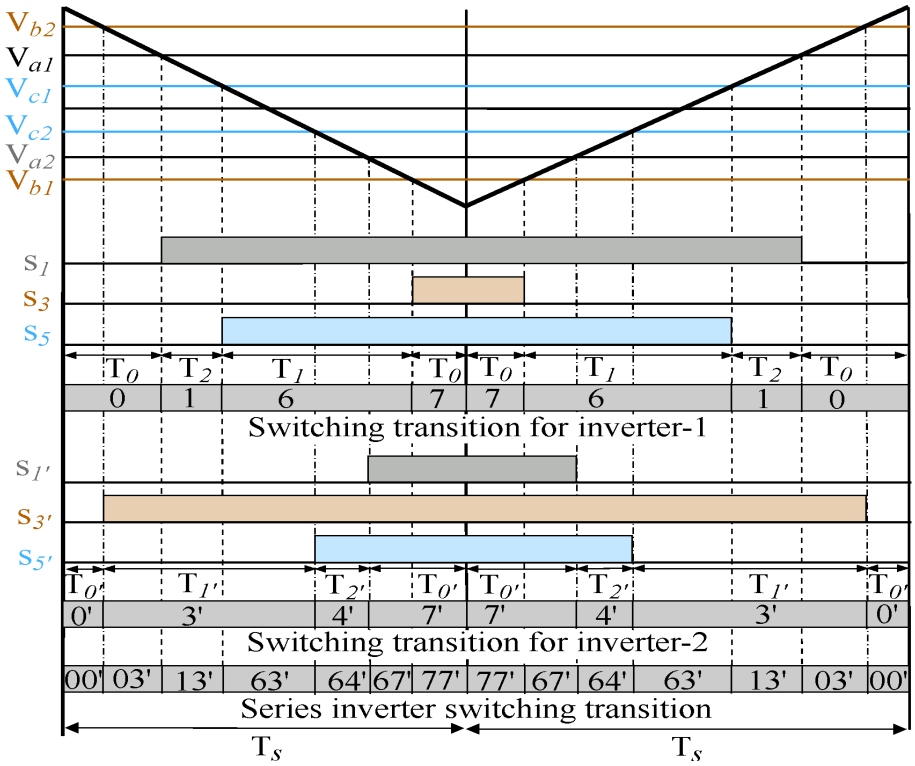

Figure 4.3: Realizing the series inverter topology pulse pattern in two sampling time intervals.

be derived in series inverter as:

$$V_{load} = (V_{dc_1}/2)(S_1 e^{j0} + S_3 e^{j120} + S_5 e^{j240}) - (V_{dc_2}/2)(S_1' e^{j0} + S_3' e^{j120} + S_5' e^{j240}) \tag{4.1}$$

Where S_1, S_3 and S_5 are the top switch switching functions of the inverter-1 while S_1', S_3' and S_5' are the top switch switching functions of the inverter-2. Here V_{dc_1}, V_{dc_2} are inverter-1 and inverter-2 DC bus voltage respectively. With the complementary switching methodology as demonstrated in [47], the series inverter topology realizes the grid voltage with half of the DC bus voltage compared to conventional parallel inverter topology. Thus, reduced DC bus voltage reflects as double the processing current by a series inverter configuration compared to a parallel inverter at a given load power rating. For clear understanding, the realization of the instantaneous grid voltage through a series inverter with half of the DC bus voltage is demonstrated using switching state 14' as follows:

$$V_{14'} = \sqrt{V_1^2 + (-V_4')^2 + 2V_1(-V_4')\cos(\pi)} \tag{4.2}$$

As V_1=$V_{4'}$=V_{dc}, (4.2) can be expanded as

$$V_{14'} = 2V_{dc} \tag{4.3}$$

The series inverter switches in an average sense concerning the reference modulation to process the network current into the load/grid network. The switching output requires

the passive inductor to filter out the switching harmonics and allow the load-demanded harmonics. Hence, the filter design allows the lower-order harmonics demanded by the load, suppresses the switching components, and is also designed based on the network time constant. The design procedure of the filter inductor is discussed in a subsequent section.

4.2 Passive filter inductance design based on the load network time constant

As described in the preceding section, the series inverter configuration can virtually manifest the double switching frequency across the load. It indicates a reduced filter requirement compared to conventional inverter topologies. On the other hand, the improved switching frequency helps to maintain the band gap between the load-demanded harmonics and the switching frequency to manage a harmonic attenuation factor. Although the passive filter is designed to attenuate the switching frequency, it must allow load-demanded harmonics. Therefore, the load time constant-based approach is adopted to design the filter inductance to ensure the effective processing of load harmonics with minimum attenuation. In this work, the load network time constant (τ_n) as a function of L_g and R_L is defined as:

$$\tau_n = \frac{L_g(per-phase\ network\ inductance)}{R_L(Resistance\ correspond\ to\ loadPower)} \tag{4.4}$$

The nonlinear load current rise time (τ_r) is defined by the load network impedance parameters such as L_g and R_L, which brings the relation between the load network time constant and the rise time as:

$$\omega_{bw} = \frac{1}{\tau_r} = \frac{1}{2.197\tau_n} \tag{4.5}$$

Here ω_{bw} denotes the load network bandwidth. The defined relation between rise time and the system bandwidth is validated at different inductances and power, as shown in Fig.4.4. It is observed that the per phase load transitional time (rise time) is approximately

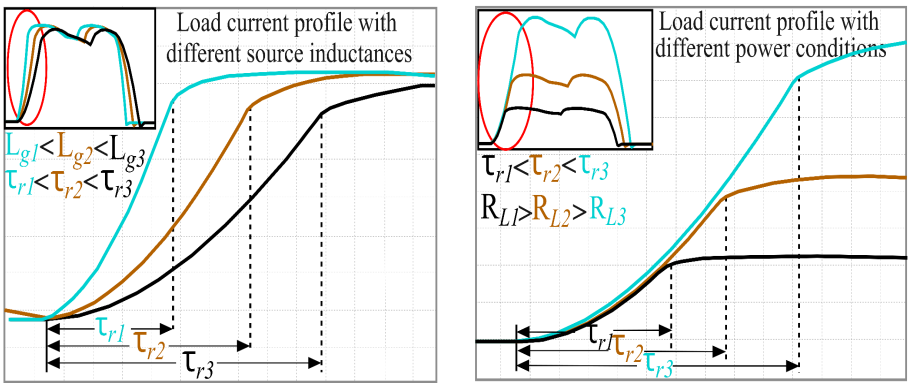

Figure 4.4: The non-linear load current variation with change in inductance L_g (left trace) and loading conditions R_L (Right trace).

2.197 τ_n. Therefore, the load network bandwidth can be determined by the network time constant or by measuring the per-phase diode transitional current waveform. With

the defined load demanded bandwidth, a wide band gap is required to be ensured by adjusting the switching frequency. Therefore, the series inverter configuration is superior in this application due to the inherent doubling of the switching frequency compared to conventional inverter circuits. Considering the achievable attenuation for the switching frequency at the rated load power, the minimum required equivalent inductance ($L_{f_{min}}$) can be computed as follows:

$$e_{f_{sw}} = \mathbb{R} i_{sw} = 2\pi f_{sw} L_f i_{sw} \tag{4.6}$$

$$L_{f_{min}} = \frac{\mathbb{R}}{2\pi f_{sw}} \quad Here \quad \mathbb{R} = \frac{V_{pcc}^2}{P} \tag{4.7}$$

Where i_{sw} is the switching frequency (F_{sw}) harmonic current. The offered impedance by the inductor must be equal to the equivalent resistance ($\mathbb{R}$) corresponding to the active power injected into the grid. As the equivalent load resistance is the parameter to derive the passive inductance, the equivalent resistance seen by the individual inverter of parallel and series configuration at give load power is shown in Table-4.1. It is clear that the load

Table 4.1: Comparison of different inverter topologies for AC filter design.

Parameter	Load Power	Individual inverter in parallel inverter	Individual inverter in series inverter
Phase Voltage	V	$V_P = V$	$V_S = \frac{V}{2}$
Phase Current	I	$I_P = \frac{I}{2}$	$I_S = I$
Active power	$P{=}VI$	$P_P{=}V_P I_P{=}\frac{P}{2}$ (individual inverter)	$P_S{=}V_S I_S{=}\frac{P}{2}$ (individual inverter)
Observed Resistance	$\mathbb{R}{=}\frac{V}{I} = R$	$\mathbb{R}_\mathbb{S}{=}\frac{V_P}{I_P} = 2R$	$\mathbb{R}_\mathbb{P}{=}\frac{V_S}{I_S}{=}\frac{R}{2}$

power is shared between the individual inverters in terms of voltage and current in series and parallel configurations, respectively. Accordingly, the equivalent resistance is halved in the proposed series inverter configuration and doubled in the parallel configuration. Therefore, the required inductance ($L_{f_{min}}$) to attenuate the switching frequency for the series inverter is four times lower than that of the parallel inverter. Further, considering the possibility of deriving double the switching frequency with a series inverter compared to the parallel inverter, the filter inductance is reduced by half with the series inverter. Therefore, the overall reduction in the inductance with the parallel and series configuration can be mathematically modeled as follows:

$$L_{f_{min(P)}} = \frac{\mathbb{R}_\mathbb{P}}{2\pi f_{sw}} = \frac{2R}{2\pi f_{sw}} \tag{4.8}$$

For series inverter configuration

$$\mathbb{R}_{\mathbb{S}} = \frac{\mathbb{R}_{\mathbb{P}}}{4} \tag{4.9}$$

$$L_{f_{min(S)}} = \frac{\mathbb{R}_{\mathbb{S}}}{2\pi f_{sw}} = \frac{R/2}{2\pi(2f_{sw})} = \frac{1}{8}L_{f_{min(P)}} \tag{4.10}$$

From (4.10), it is clear that, under identical power conditions, the series inverter can produce equivalent switching current ripple with only one-eighth of the inductance required in a parallel inverter configuration.

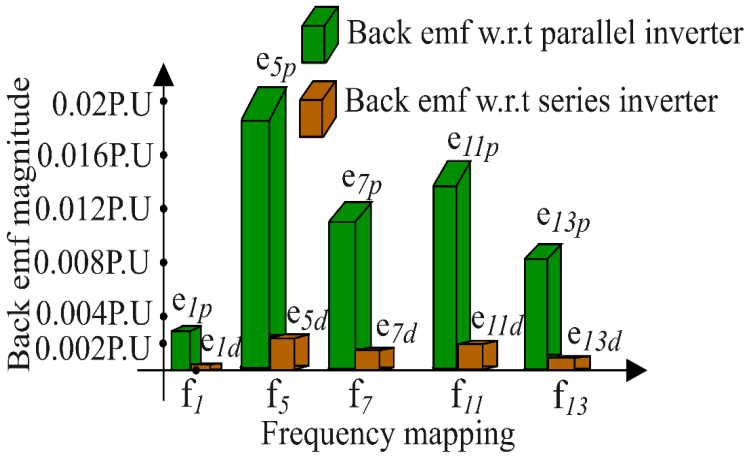

Figure 4.5: The variation of back emf and harmonic current magnitude corresponds to the harmonic component.

The reduced inductance offers significantly lesser attenuation for other load harmonics in series inverter configuration, as shown in Fig. 4.5. With the offered minimum attenuation to the load harmonics, the series configuration effectively processes the load demanded harmonics, as shown in Fig. 4.5. Thus, it improves the grid's current power quality significantly. Apart from the load harmonic processing, the AC filter and the series inverter are responsible for the smooth injection of AC power to the load network. The equivalent AC power injection reference generated for the proposed series configuration based on the availability of input solar power is described in the following section.

4.3 Input port DC chopper design specifications and corresponding solar power reference generation for the series inverter

The dual port series configuration shares power in terms of voltage but processes the same current by both inverters. The DC choppers extract the maximum power from the individual ports. In this work, the DC choppers are designed considering the voltage variation range V_{oc} and V_{mppt}. Considering the operating range of the DC chopper, the reactive components for the DC chopper depicted in Fig.4.6 are designed as follows:

$$L_{dc} = \frac{V_o(1-D)}{\triangle I_L F_{sw}} \tag{4.11}$$

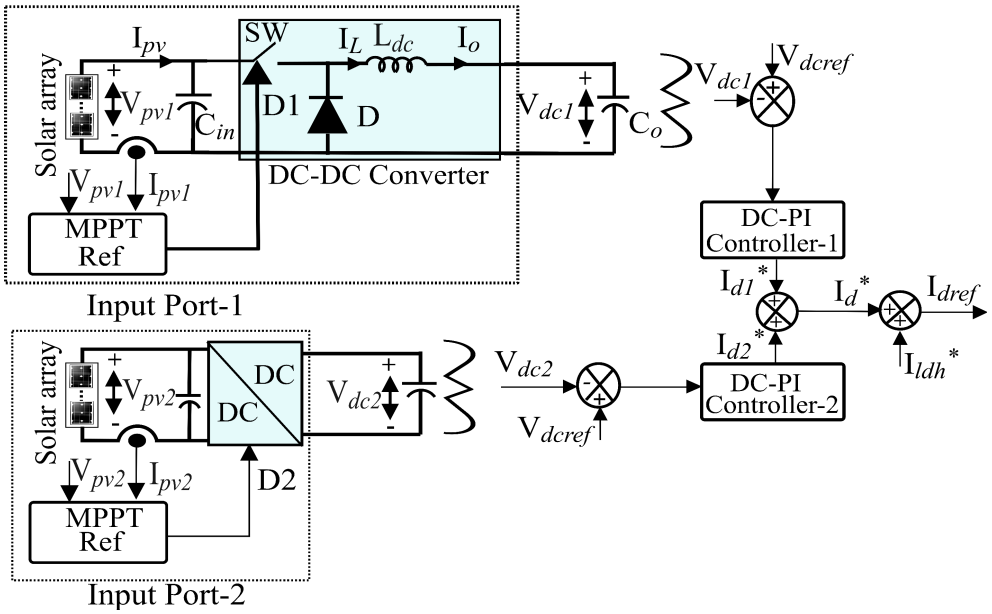

Figure 4.6: The input ports maximum power point tracking and corresponding reference generation for series inverter

$$C_o = \frac{\triangle I_L}{8 \triangle V_o F_{sw}} \tag{4.12}$$

$$C_{in} = \frac{I_o(1-D)D}{\triangle V_{pv} F_{sw}} \tag{4.13}$$

Where L_{dc} corresponds to the inductance, V_o is the output voltage, D is the duty ratio, I_L is the inductor current, C_o is the output capacitance, C_{in} is the input capacitance, I_o and F_{sw} is the switching frequency of the DC to DC converter. The solar panels are connected in series at the input ports to generate the adequate open circuit voltage (V_{oc}). The DC chopper shown in Fig.4.6 is designed to operate the solar panel at MPPT (V_{mppt}) with the operating range of (V_{oc} to V_{mppt}). The duty for the individual DC choppers is derived using the Perturb and Observe (P&O) algorithm. By maintaining the current sec balance, the DC bus voltage of the individual DC chopper is maintained at V_{dcref} irrespective of the processing power, as shown in Fig.4.6. With this, DC-PI generates the individual current reference i_{d1}^* at port-1, i_{d2}^* at port-2 and combined reference can be generated as $i_d^* = i_{d1}^* + i_{d2}^*$. The instantaneous generated i_d^* represents the total available power at the dual input ports, and it can be used to generate the modulation for the individual inverter through closed-loop control, as described in the following section.

4.4 Closed loop controller modeling for the proposed series inverter harmonic and active power injector

This section demonstrates closed-loop controller modeling of the series inverter topology to feed the load-demanded power and harmonics, as detailed control flow architecture shows in Fig. 4.1. For the controller, active and reactive power references are synthesized in the synchronous reference frame (SRF) by taking the PCC voltage as a reference. On

SRF, the PCC voltage can be represented as:

$$\begin{aligned} V_{gd} &= \frac{2}{3}(V_{ga}cos(\omega t) + V_{gb}cos(\omega t - 120^o) + \\ &\quad V_{gc}cos(\omega t + 120^o)) = \frac{m_a V_{dc}}{2}; \\ V_{gq} &= \frac{-2}{3}(V_{ga}sin(\omega t) + V_{gb}sin(\omega t - 120^o) + \\ &\quad V_{gc}sin(\omega t + 120^o)) = 0; \end{aligned} \tag{4.14}$$

Here ωt is the reference angle generated through a phase-locked loop (PLL). With the generated reference angle, the load currents are translated onto SRF as:

$$\begin{aligned} I_{dl} &= \frac{2}{3}(I_{la}cos(\omega t) + I_{lb}cos(\omega t - 120^o) + I_{lc}cos(\omega t + 120^o)); \\ I_{ql} &= \frac{-2}{3}(I_{la}sin(\omega t) + I_{lb}sin(\omega t - 120^o) + I_{lc}sin(\omega t + 120^o)); \end{aligned} \tag{4.15}$$

Here I_{la}, I_{lb} and I_{lc} are the three-phase non-linear load currents sensed before the diode bridge rectifier as shown in Fig.4.1. From the nonlinear load current, the harmonics information is extracted by subtracting the load fundamental current component as:

$$\begin{bmatrix} I_{dh} \\ I_{qh} \end{bmatrix} = \begin{bmatrix} I_{dl} - Avg(I_{dl}) \\ I_{ql} \end{bmatrix} \tag{4.16}$$

With the extracted load current ripple information, the active and reactive power reference to the current controller can be obtained by adding the PV active power reference generated from the maximum power point loop ($I_d^*(MPPT)$) as:

$$\begin{bmatrix} I_{dref} \\ I_{qref} \end{bmatrix} = \begin{bmatrix} I_{dh} + I_d^*(MPPT) \\ I_{qh} \end{bmatrix} \tag{4.17}$$

Here, I_{dref} is the direct axis reference consisting of the solar active power reference and extracted load demanded harmonic reference. Depending upon the available solar power, the series inverter can operate in four different modes of operation, as illustrated in Fig.4.7.

4.4.1 Modes of operation of harmonic compensator

1. **No compensation mode (dotted teal line):** In this mode of operation, the compensator is not enabled, so the load draws the harmonics and active power from the grid ($P_{inv} = 0$ and $P_L = P_g$).

2. **Harmonic compensation mode (Solid teal line):** In this mode of operation, the compensator only supplies the harmonics required by the load ($P_{inv} = P_{Lh}$), and the grid supplies the total load demanded active power.

3. **Grid support mode (dotted violet line):** The compensator in this mode supplies all the harmonics and available active power, which is less than the load demanded

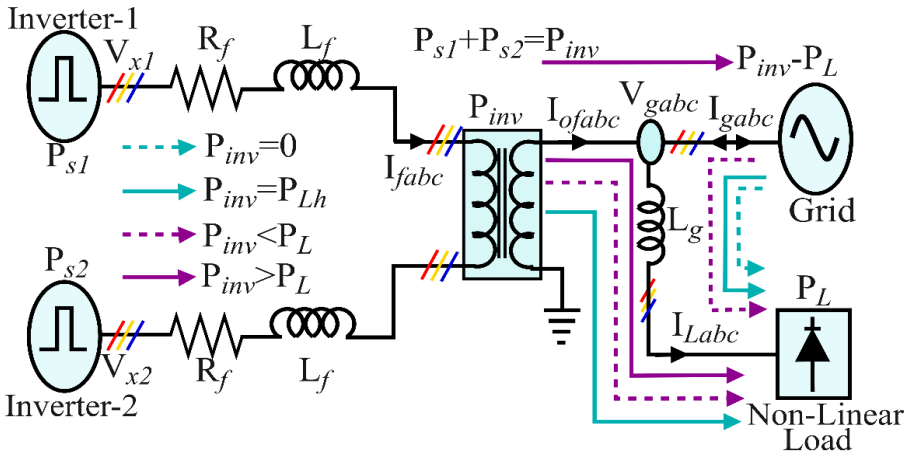

Figure 4.7: The single line diagram of a series inverter harmonic compensator with a different mode of operations.

power (P_{inv}<($P_L + P_{Lh}$)). The grid supplies the remaining load demanded active power.

4. **Grid injection mode (solid violet line):** In this mode of operation, the compensator supplies all the harmonics and active power required by the load. Upon meeting the requirement of active load power, the surplus PV power is injected into the grid (P_{inv}>($P_L + P_{Lh}$)).

4.4.2 System impedance modeling for the controller design

In a series configuration, for individual inverters, the controller gains are derived through impedance modeling with the extracted reference to the series inverter configuration. For preparing the impedance model of the series inverter configuration, the transformer's secondary side circuit is transformed to the primary side, as shown in Fig.4.8. In Fig.4.8, $R_{tf(p)}$ and $L_{tf(p)}$ indicate the resistance and leakage inductance of transformer primary winding. Similarly, $R_{tf(s)}$ and $L_{tf(s)}$ are the resistance and leakage inductance of transformer secondary winding. Considering the transformer with a turns ratio of 1:1, the translated impedance onto the primary side can be depicted as $R_{tf(p)} = R_{tf(s)} = R_{tf}$ and $L_{tf(p)} = L_{tf(s)} = L_{tf}$.With the derived impedance, the transfer function of the system depicted in Fig. 4.8 can be modeled by applying the KVL as:

$$V_{x_1} - i_{fx}(2R_f + 2R_{tf}) - (2L_f + 2L_{tf})\frac{di_{fx}}{dt} - V_{gx} - V_{x_2} = 0 \tag{4.18}$$

$$(V_{x_1} - V_{x_2}) = i_{fx}(2R_f + 2R_{tf}) + (2L_f + 2L_{tf})\frac{di_{fx}}{dt} + V_g \tag{4.19}$$

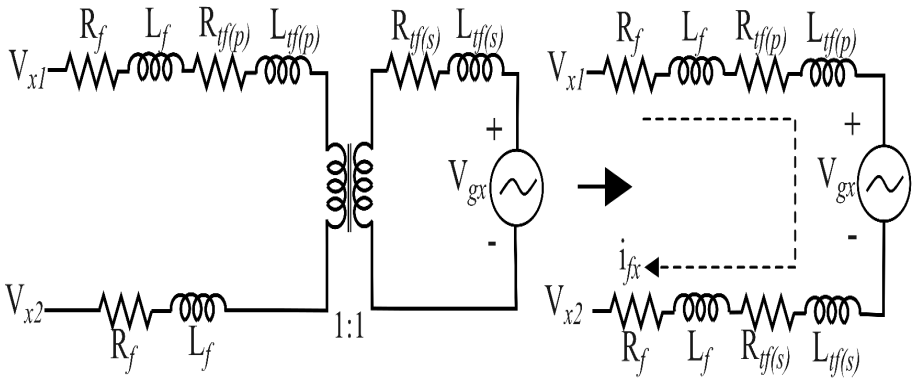

Figure 4.8: The equivalent circuit representation with transformer and transforming all parameters to a primary side of the isolating transformer.

Where V_g is the grid phase voltage. V_g can be written in terms of the power resistor as $V_g = i_{fx}R_d$ where R_d can be written as $R_d = (V_g/i_{fx})$.

$$V_{x_1x_2} = i_{fx}(2R_f + 2R_{tf}) + (2L_f + 2L_{tf})\frac{di_{fx}}{dt} + i_{fx}R_d \tag{4.20}$$

The (4.20) can be written in a composed form as follows:

$$V_{x_1x_2} = R_{eq}i_{fx} + L_{eq}\frac{di_{fx}}{dt}; \quad where(x = a, b, c) \tag{4.21}$$

Where the $V_{x_1x_2}$ is the overall voltage generated by the series inverter. Here $R_{eq} = 2R_f + R_d + 2R_{tf}$, and $L_{eq} = 2L_f + 2L_{tf}$, are the equivalent resistance and inductance for the series inverter topology. Further, the series inverter terminal voltages and currents are translated onto the synchronous reference frame, realizing the active and reactive components as:

$$\begin{aligned} V_{fd} &= \frac{2}{3}(V_{a_1a_2}cos(\omega t) + V_{b_1b_2}cos(\omega t - 120^o) + \\ &\quad V_{c_1c_2}cos(\omega t + 120^o)); \\ V_{fq} &= \frac{2}{3}(V_{a_1a_2}sin(\omega t) + V_{b_1b_2}sin(\omega t - 120^o) + \\ &\quad V_{c_1c_2}sin(\omega t + 120^o)); \end{aligned} \tag{4.22}$$

$$\begin{aligned} i_{fd} &= \frac{2}{3}(i_{fa}cos(\omega t) + i_{fb}cos(\omega t - 120^o) + i_{fc}cos(\omega t + 120^o)); \\ i_{fq} &= \frac{-2}{3}(i_{fa}sin(\omega t) + i_{fb}sin(\omega t - 120^o) + i_{fc}sin(\omega t + 120^o)) \end{aligned} \tag{4.23}$$

From the voltages (V_{fd}, V_{fq}) and currents (i_{fd}, i_{fq}), the system state space model in the form of $Y(s) = (C(SI - A)^{-1}B + D) * U(s)$ is derived (derivation is given in detail in appendix) to design the PI-controller a shown in Fig.4.9. From the state space model, the

plant transfer function (G_{11} and G_{22}) can be derived as:

$$G_{11} = G_{22} = \frac{(sL_{eq} + R_{eq})(V_{dc})}{s^2L_{eq}^2 + 2L_{eq}R_{eq}s + R_{eq}^2 + \underbrace{(\omega L_{eq})^2}_{\approx 0}} \tag{4.24}$$

By neglecting $(\omega L_{eq})^2$, the plant transfer function can be simplified to:

$$G_{plant} = \frac{1}{(sL_{eq} + R_{eq})} = \frac{1/L_{eq}}{s + R_{eq}/L_{eq}} \tag{4.25}$$

The derived plant model in (4.25) represents the parallel and series configurations, but

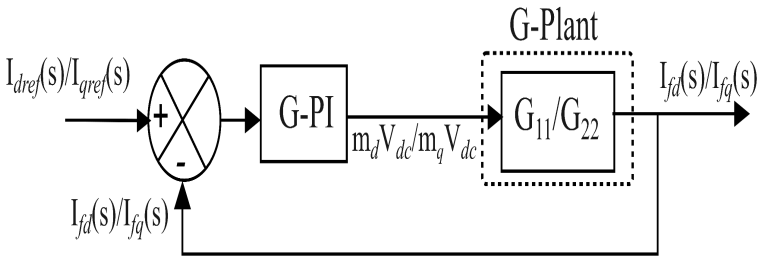

Figure 4.9: The block diagram of the consolidated plant model along with the controller.

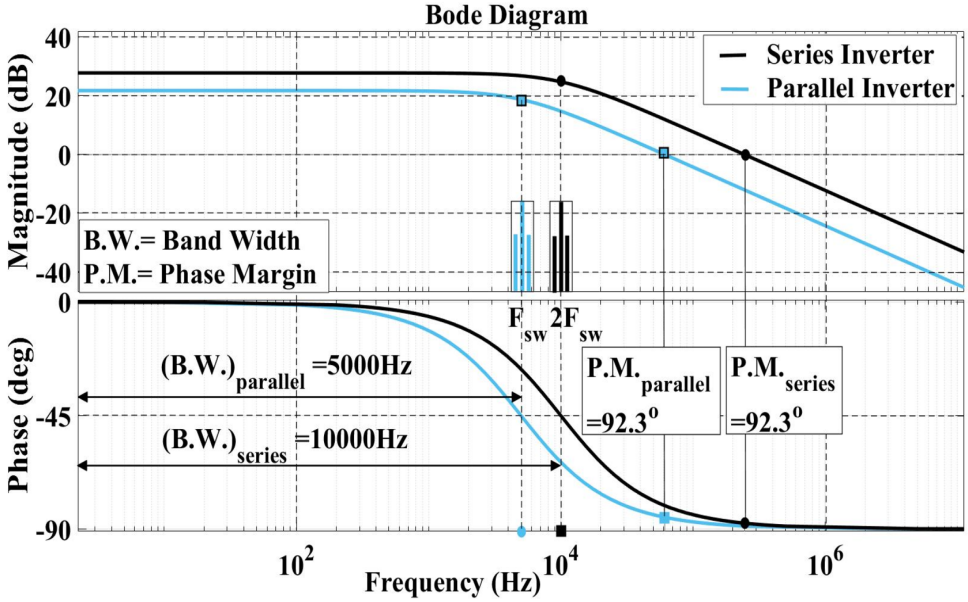

Figure 4.10: Open loop plant transfer function bode plot for series and parallel inverter harmonic cum active power injector.

the equivalent inductance vary for both the configurations as derived in (4.10). With the substituted equivalent inductance in the plant model it is evident from Fig.4.10, that the series inverter yields double the bandwidth compared to parallel inverter configuration.

4.4.3 Designing of the PI controller

For the simplified plant model, the PI controller is designated, and proportional and integral controller coefficients are modeled as follows:

$$G_{PI}(s) = K_P + \frac{K_i}{s}; \quad G_{open}(s) = G_{PI}(s) * G_{plant}(s) \tag{4.26}$$

$$G_{open}(s) = \left[\frac{K_p}{sL_{eq}}\right]\left[s + \frac{K_i}{K_p}\right]\left[\frac{1}{s + \frac{R_{eq}}{L_{eq}}}\right] \tag{4.27}$$

The bode plot of the $G_{open}(s) = G_{PI}(s) * G_{plant}(s)$ is plotted in Fig.4.11 for the different

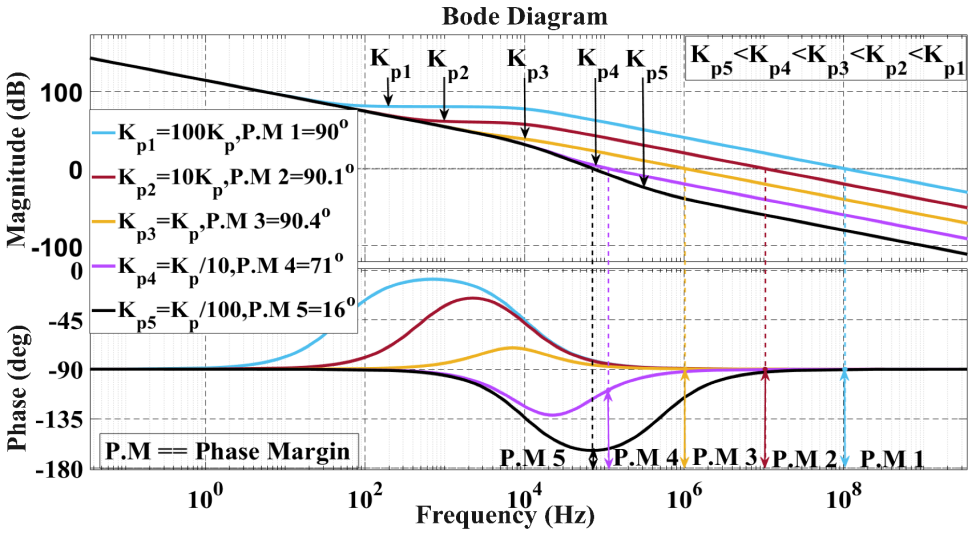

Figure 4.11: Open-loop transfer function bode plot for a series inverter with different controller proportional gains.

values of K_p by fixing the value of K_i for series inverter topology. From Fig.4.11, it is observed that when the value of the K_p is very less (K_{p5}) the system phase margin is very low (16^o) while at other values of K_p (K_{p1}, K_{p2}, K_{p3} and K_{p4}) the system phase margin is higher. The gain margin of the system is always positive. By applying the pole-zero cancellation criterion, the K_p and K_i values for inner current control loop can be computed as

$$K_p = \frac{L_{eq}}{\tau_s}; K_i = \frac{R_{eq}}{L_{eq}} K_p \tag{4.28}$$

Where τ_s is the closed loop time constant of the system. For parallel and series inverter, the values of K_p and K_i can be expressed as follows:

$$K_{p_p} = \frac{L_{eq_p}}{\tau_s}; K_{p_d} = \frac{L_{eq_d}}{\tau_s}; K_{i_p} = \frac{R_{eq_p}}{L_{eq_p}} K_{p_p}; K_{i_d} = \frac{R_{eq_d}}{L_{eq_d}} K_{p_d} \tag{4.29}$$

With computed values of K_p & K_i using (4.29), the step response of closed-loop transfer

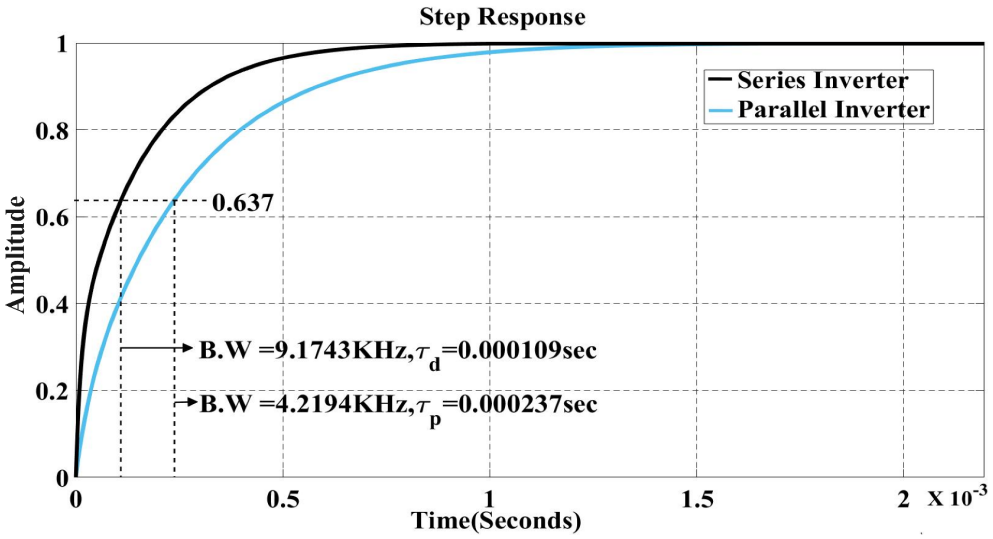

Figure 4.12: Step response of closed-loop transfer function for series and parallel harmonic cum active power injector.

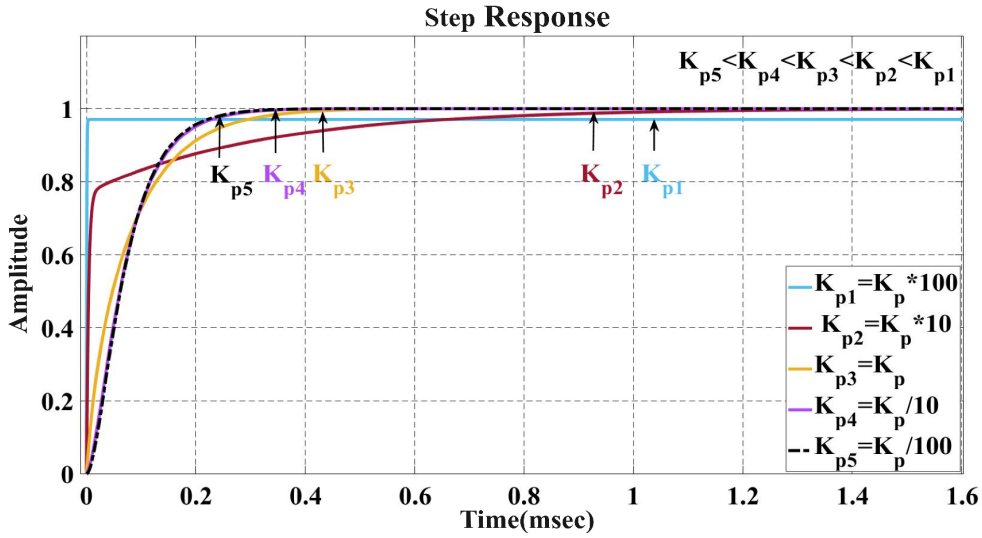

Figure 4.13: Closed-loop transfer function step response for a series inverter with different controller proportional gains (K_p).

function is plotted for series and parallel inverter is shown in Fig.4.12. Observing the step response of the closed-loop transfer function, as illustrated in Fig. 4.12, the dynamic response is quicker for the series inverter than the parallel inverter typology. The step response of the closed-loop transfer function for the series inverter is plotted at different values of K_p and shown in Fig.4.13. From Fig.4.13, it is observed that when K_p increases the system dynamic response will be faster.

4.5 Results and Discussion

The effectiveness of the proposed configuration over parallel inverters in terms of improved grid power quality and active power injection is verified through a hardware prototype. The real-time performance comparison of the proposed series inverter and parallel

inverter in terms of active power injection with simultaneous harmonic compensation is demonstrated through the experimental prototype developed in the lab as shown in Fig.4.14. The developed experimental prototype specifications are tabulated in Table-4.2.

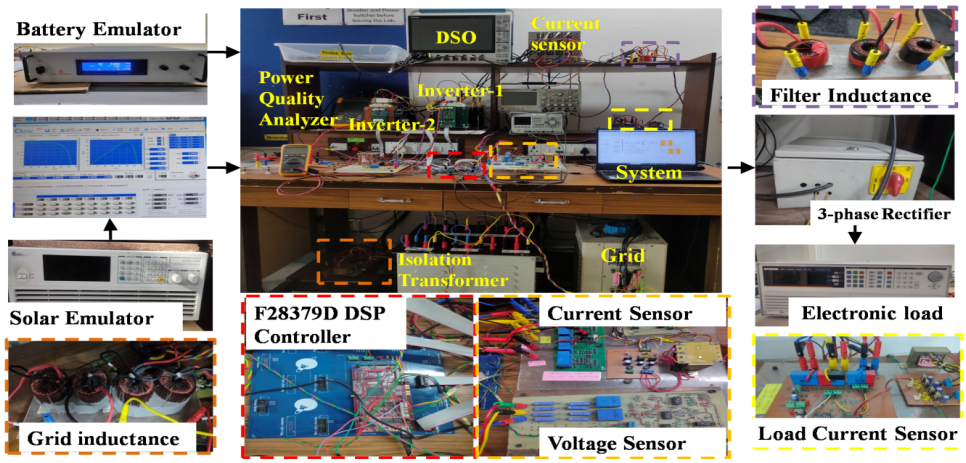

Figure 4.14: The experimental lab prototype for demonstrating series and parallel configuration.

Table 4.2: Experimental operating parameter of series and parallel harmonic compensator.

Parameters	Symbols	Parallel	Series
Power (Load)	(P)	1550 W	1550 W
DC voltage	(V_{dc})	400 V	200 V
Switching Frequency	(F_{sw})	5 KHz	5 KHz
Load experienced harmonics	(H_{sw})	5 KHz	10 KHz
filter inductance	$(L_{f_{min}})$	1.49 mH	0.186 mH
PCC line-line voltage	V_{L-L}	130 V	130 V
proportional gain	K_P	13.31	4.412
Integral gain	K_I	43642.28	43642.28
DC buck Inductance	L_{dc}	-	3.5 mH
DC input capacitance	C_{in}	-	48 μF
DC-link capacitance	$C_o + C_{dc}$	-	2214.06 μF

4.5.1 Hardware validation for harmonic compensation

The following observations are made in regard to a nonlinear load that is initially connected to the grid. The load current drawn from the grid is found to have a total harmonic distortion (THD) of 21.9%, as shown in Fig.4.15a. After implementing an isolated parallel configuration for harmonic compensation, the grid current THD is reduced to 6.7%. However, the proposed series configuration offers better harmonic compensation due to its enhanced bandwidth. With the proposed series configuration, the grid current THD is further reduced to 4.5% as depicted in Fig.4.15c (right). The results demonstrate the efficacy of dedicated harmonic compensation in achieving improved bandwidth and

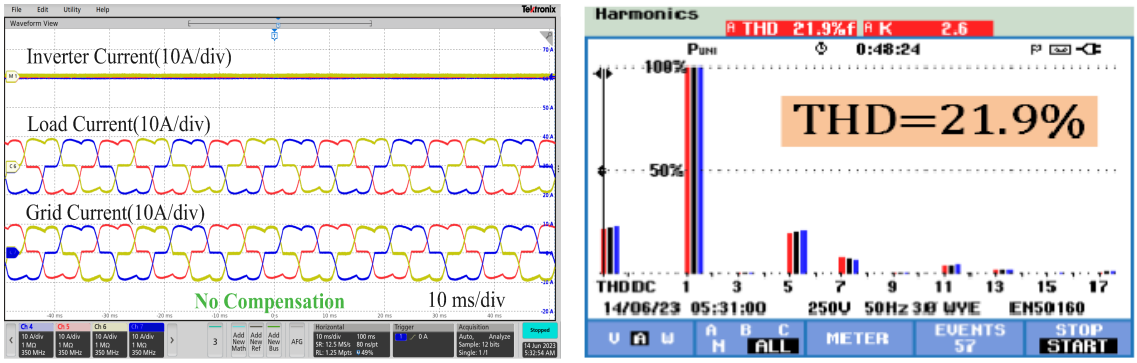

(a) With no harmonic compensation.

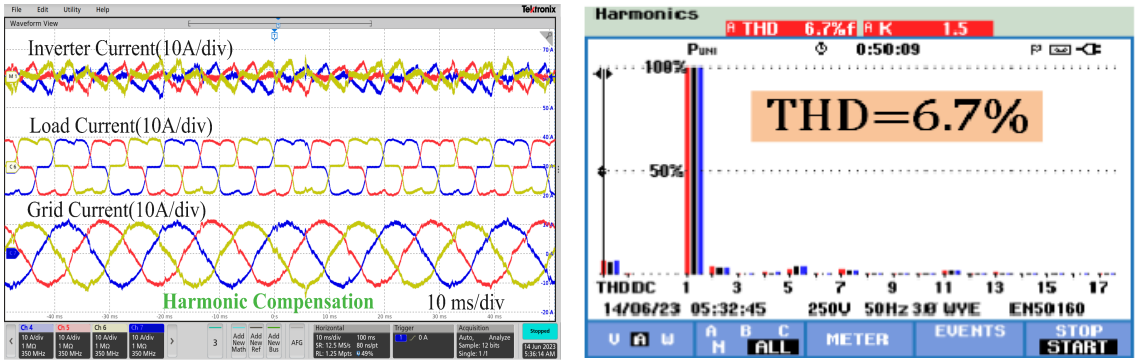

(b) Harmonic compensation with parallel inverter configuration.

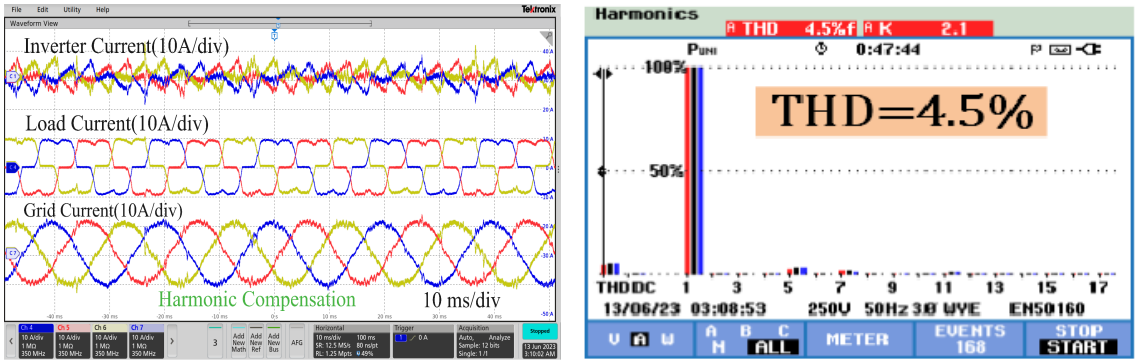

(c) Harmonic compensation with series inverter configuration.

Figure 4.15: Inverter currents (top trace), load currents (Middle trace), and grid currents (bottom trace) along with grid current THD for parallel (Fig. 4.15b) and series (Fig. 4.15c) harmonic compensator.

enhanced harmonic compensation capability. Additionally, the series solar inverter configuration is effective in simultaneous active power injection along with load harmonic compensation.

4.5.2 The experimental validation of proposed series configuration operational capability of simultaneous active power and harmonic injection

With the symmetric input power variations

The series inverter's active power injection and nonlinear harmonic compensation load are evaluated experimentally by tracking an individual inverter's maximum power point (P & O method). With the dynamic irradiance change, the adopted MPP algorithm of

individual inverter tracks the maximum power and derives the current reference to the proposed series inverter configuration. The series inverter configuration delivers power to the network in grid support mode and/or grid injection mode based on the available solar energy, as depicted in Fig. 4.16. To establish different power modes, the series

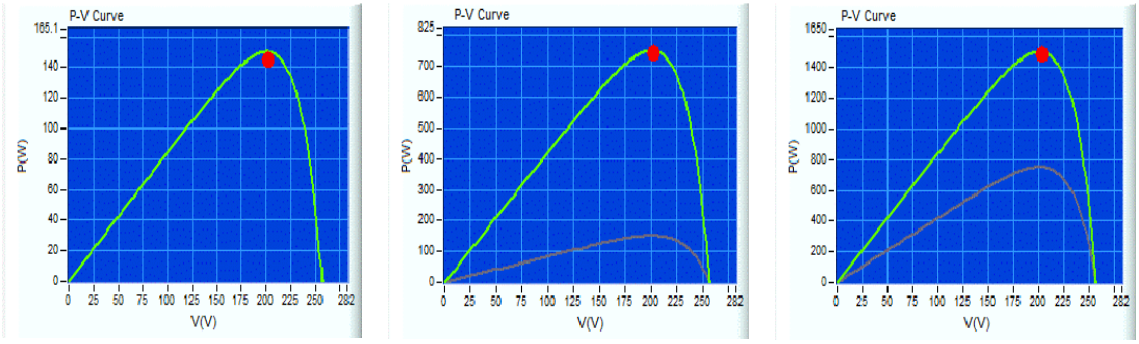

(a) $L_f = L_{fmin} = 0.6mH$.

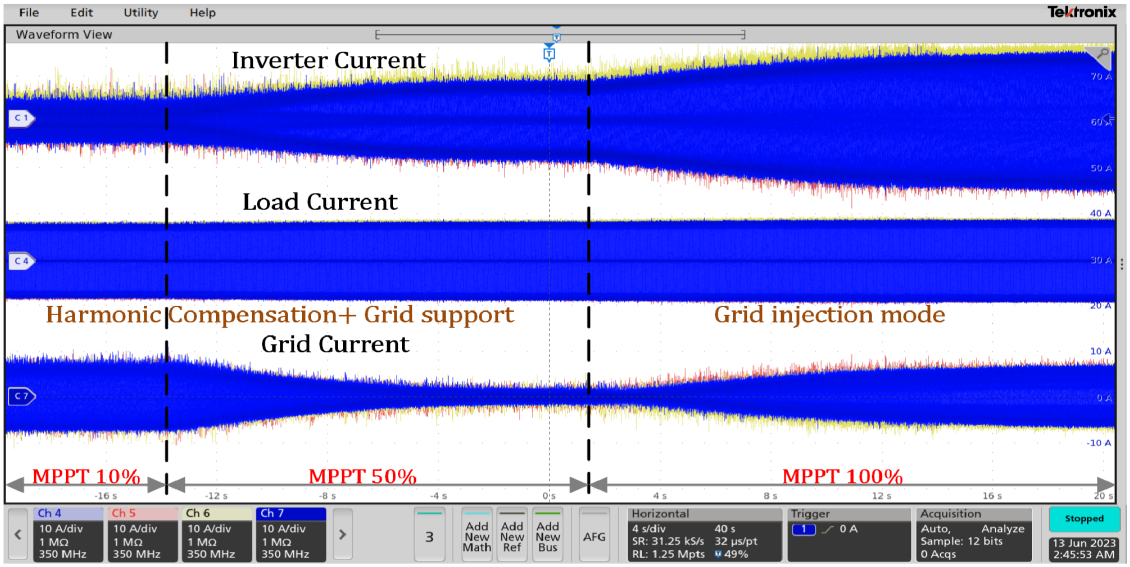

(b) Series inverter three-phase current (top trace: X=4 sec/div, Y=10 A/div), Load current(middle trace: Y=10 A/div), and grid current(bottom trace: Y=10 A/div).

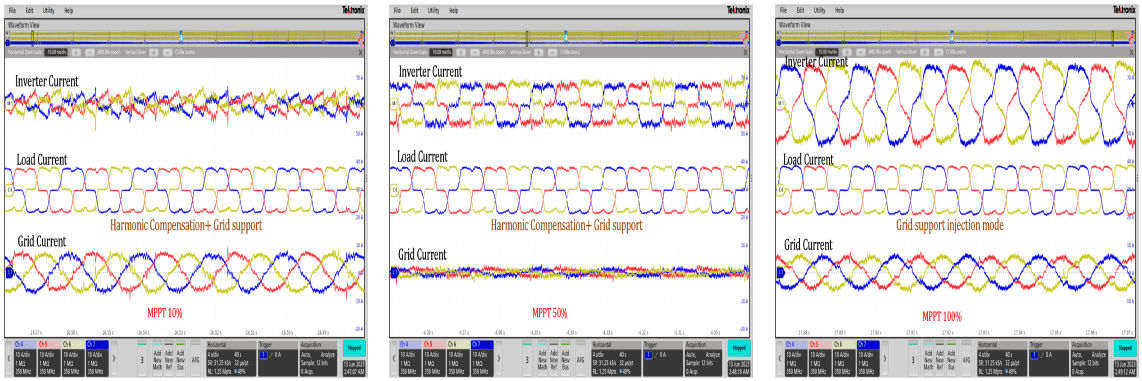

(c) Corresponding zoomed portions of series inverter power 300 W(bottom left figure: X=10 msec/div, Y=10 A/div), 1500 W(bottom middle figure: Y=10 A/div), 3000 W(bottom right figure: Y=10 A/div).

Figure 4.16: The series configuration behavioral studies at different solar irradiance.

configuration is tested dynamically with power outputs ranging from 10% (300 W) to 50% (1500 W) and 100% (3000 W) at the nonlinear load of 1550 W.

Table 4.3: Different modes of operation of the series harmonic compensator.

Modes	Harmonic Compensation mode	Grid support mode	Grid injection mode
Series inverter power	300 W	1500 W	3000 W
Solar inverter current (peak)	1.88 A	8.799 A	17.59 A
Load current (peak)	9.742 A	9.742 A	9.742 A
Grid current (peak)	7.856 A	0.94 A	-7.857 A
Grid current THD	4.5%	-	4.6%

As in series configuration, two inverters share the power equally; the individual inverters operate at half of the rated power, i.e., 150 W (10% of rated power), 750 W (50% of rated), and 1500 W (100% of rated), as illustrated in Fig. 4.16(a). By maintaining a 1550 W nonlinear load and varying the maximum power point tracking (MPPT) power, the series configuration operates exclusively in compensation mode (300 W solar power), grid support mode (1500 W), and grid injection mode (3000 W solar power), as described in the middle scope traces of Fig. 4.16. The corresponding zoomed portions of the inverter current, load current, and grid current profiles are shown for the compensation mode (left figure), grid supporting mode (middle figure), and grid injection mode (right figure) in the bottom scope traces of Fig.4.16.

In the case of compensation mode (bottom left of Fig. 4.16), only the series inverter supports the harmonics (10% of rated), resulting in a sinusoidal grid current with a corresponding load active power of 1550 W. On the other hand, when the solar irradiance is at 50%, the series inverter injects 1500 W of solar active power into the load, while the remaining 50 W required by the load is drawn from the grid, as depicted in the bottom middle scope traces of Fig. 4.16. With the surplus solar active power of 3000 W, the series configuration injects 1450 W into the grid, as shown in the bottom right scope traces of Fig. 4.16.In all conditions, the grid current shapes into sinusoidal and maintains the %THD as mentioned in Table-4.3.

With arbitrary irradiance change at input ports

Along with the scenario of uniform irradiance across the input ports, the arbitrary solar irradiance change scenario is validated experimentally by varying the input power across the two ports arbitrarily, as depicted in Fig.4.17. In the experimental validation, the power of one of the input ports changes from 240 W (20%) to 1200 W (100%), and another source is maintained at 240 W (20%) as depicted in Fig. 4.17a. The DC-link voltage at both the input ports is regulated at 200V irrespective of input power variations, as shown in Fig. 4.17b. In the DC chopper output capacitor, the current-sec balance generates the current reference for the series configuration inverters as illustrated in Fig. 4.17. Based on the generated reference, the series inverter injects the combined active power (summation of two input ports) along with the load demanded harmonics from the grid, as shown

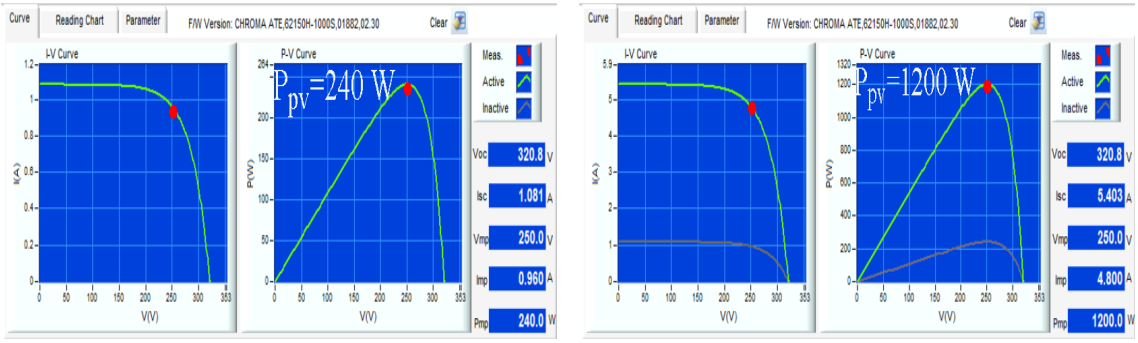

(a) The input port solar power tracking I-V and P-V curves at 240 W(left) and 1200 W (right).

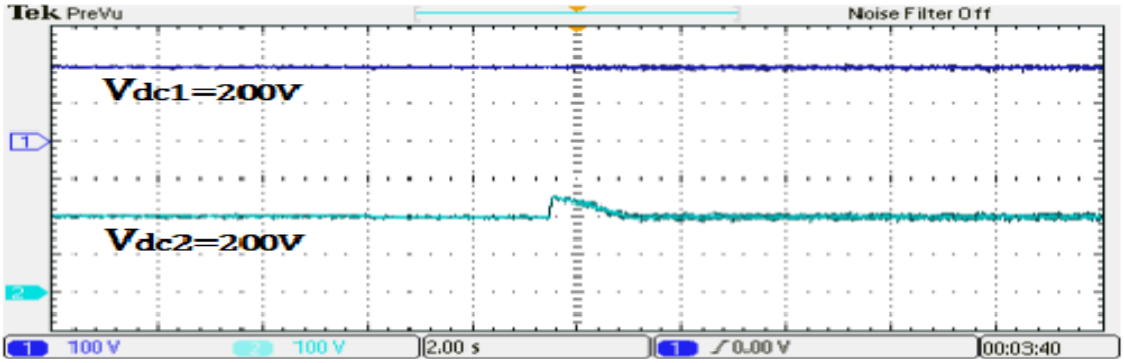

(b) The series configuration DC-link voltage regulation with change in solar input power.

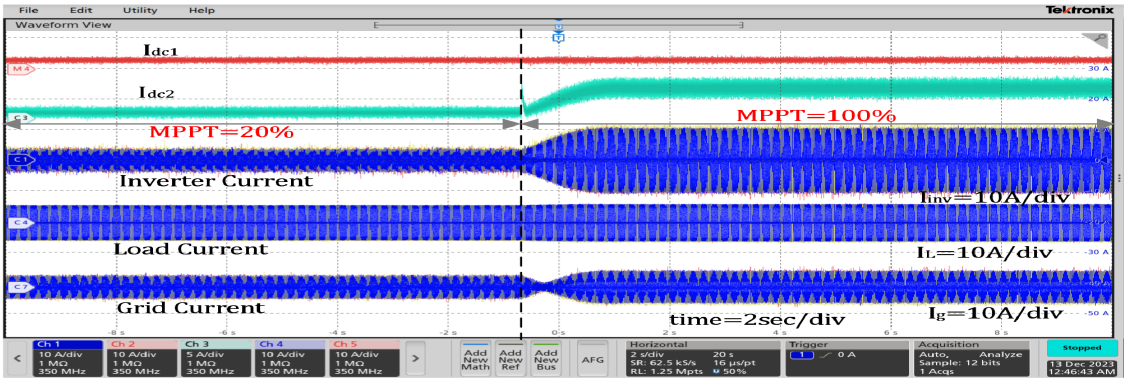

(c) Variation of input port-1 DC source current (top trace), Input port-2 DC source current (second trace), series inverter processing current (third trace: X-axis: 2 sec/div, Y-axis: 10 A/div), AC Load current (fourth trace: Y-axis:10 A/div) and grid current (bottom trace: Y-axis: 10 A/div). with the asymmetrical change of input port-2 power from 240 W to 1200 W.

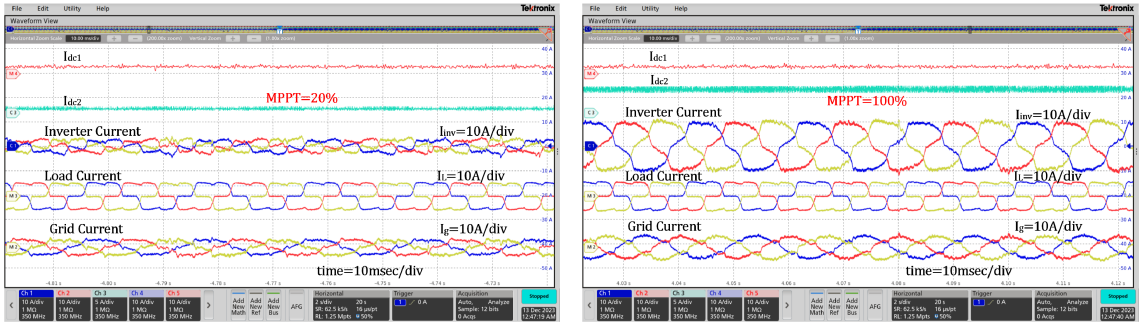

(d) corresponding zoomed portion of Fig.4.17c at individual input ports at 240 W and 240 W (left side) and at input port-1 and input port-2 operated with 240 W, 1200 W respectively (Right side).

Figure 4.17: The input (DC) and output (AC) current and voltage signatures of proposed series configuration with asymmetrical solar irradiance variations.

in Fig.4.17c. As shown in the left zoomed portion of Fig.4.17d, the combined power of 480W (240W+240W) is supported by the series configuration, and the remaining load demand power of 400 W is drawn from the grid. The right zoomed figure depicts the combined power of 1440 W (1200 input port-1 + 240 input port-2)) is processed by the series configuration that injects 560 W into the grid at the load power of 880 W. Similarly,

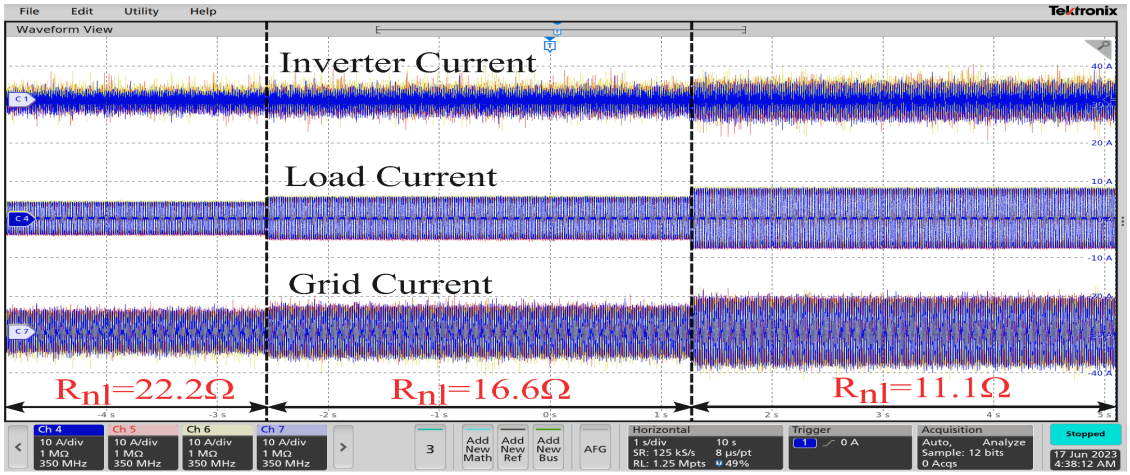

(a) The inverter current (top trace X:1sec/div Y:10A/div), the three-phase load current (middle trace Y:10A/div) and grid current (bottom trace Y:10A/div).

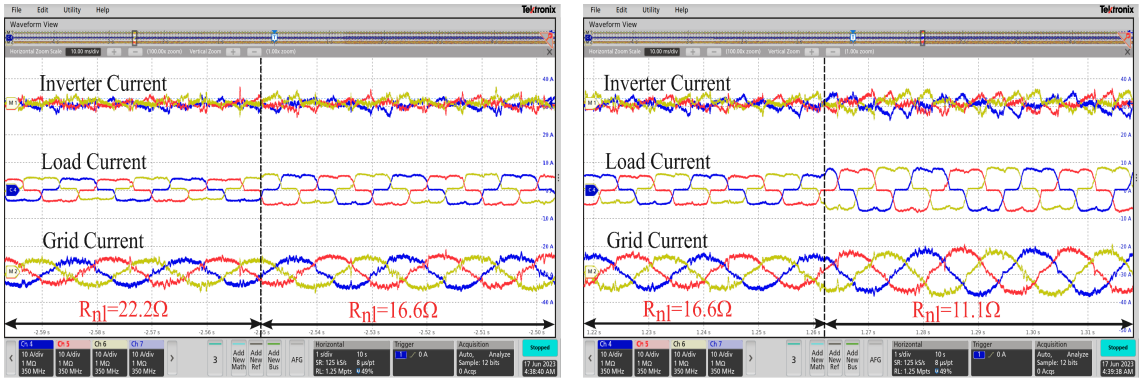

(b) The zoomed portion depicting the load power variation from 660 W to 885 W (left figure X:10msec) and 885 W to 1330 W (right figure).

Figure 4.18: The series SAPCHI experimental results with dynamic load variation.

the proposed series configuration is tested at dynamic loading conditions by varying the charging station load from 660 W to 885 W and 885W to 1330W, as shown in Fig.4.18. The configuration is tested at harmonic compensation mode alone at minimum solar irradiance. From the experimental results shown in Fig.4.18, it is visible that, irrespective of load change (lower to higher), the proposed configuration can compensate harmonics and shape the grid current as per the IEEE-519 standards. The experimental results clearly show that the proposed configuration efficiently extends harmonic support in load and input power dynamic variations.

4.6 Conclusion

This work demonstrates the effectiveness of a series solar inverter configuration in simultaneously compensating for nonlinear load harmonics and injecting active power. With unique attributes, such as operating with half of the pole voltage and exhibiting double the switching frequency, the series inverter reduces the filter size requirement by eight times compared to a parallel inverter. Moreover, the doubled system bandwidth enhances extended harmonic compensation, reducing grid current %THD. The superiority of the proposed series inverter is tested under different test conditions, such as symmetrical and asymmetrical solar power change (DC side) and different loading conditions (AC side). Experimental results validate that the proposed configuration effectively shapes the harmonics, resulting in a grid current %THD that complies with IEEE-519 standards in real-time conditions.

Appendix

The instantaneous active and reactive current variations with time can be expressed by differentiating (i_{fd} and i_{fq}) as:

$$\begin{aligned}
\frac{di_{fd}}{dt} &= \frac{2}{3}((\frac{di_{fa}}{dt})cos(\omega t) + (\frac{di_{fb}}{dt})cos(\omega t - 120) + (\frac{di_{fc}}{dt}) \\
&\quad cos(\omega t + 120)) - \frac{2}{3}\omega(i_{fa}sin(\omega t) + i_{fb}sin(\omega t - 120^o) \\
&\quad + i_{fc}sin(\omega t + 120^o)) \\
\frac{di_{fq}}{dt} &= -\frac{2}{3}((\frac{di_{fa}}{dt})sin(\omega t) + (\frac{di_{fb}}{dt})sin(\omega t - 120) + (\frac{di_{fc}}{dt}) \\
&\quad sin(\omega t + 120)) - \frac{2}{3}\omega(i_{fa}cos(\omega t) + i_{fb}cos(\omega t - 120^o) + \\
&\quad i_{fc}cos(\omega t + 120^o)); \qquad (4.30)
\end{aligned}$$

Using(4.21), the equation (4.30) can be simplified to

$$\begin{aligned}
\frac{di_{fd}}{dt} &= \frac{2}{3}((\frac{V_{a1a2}}{L_{eq}} - \frac{R_{eq}}{L_{eq}}i_{fa})cos(\omega t) + (\frac{V_{b1b2}}{L_{eq}} - \frac{R_{eq}}{L_{eq}}i_{fb}) \\
&\quad .cos(\omega t - 120) + (\frac{V_{c1c2}}{L_{eq}} - \frac{R_{eq}}{L_{eq}}i_{fc})cos(\omega t + 120)) \\
&\quad + \omega i_{qref} \\
\frac{di_{fq}}{dt} &= \frac{2}{3}((\frac{V_{a1a2}}{L_{eq}} - \frac{R_{eq}}{L_{eq}}i_{fa})sin(\omega t) + (\frac{V_{b1b2}}{L_{eq}} - \frac{R_{eq}}{L_{eq}}i_{fb}) \\
&\quad .sin(\omega t - 120) + (\frac{V_{c1c2}}{L_{eq}} - \frac{R_{eq}}{L_{eq}}i_{fc})sin(\omega t + 120)) \\
&\quad - \omega i_{dref} \qquad (4.31)
\end{aligned}$$

$$\begin{aligned}\frac{di_{fd}}{dt} &= \frac{2}{3}(\frac{V_{a1a2}}{L_{eq}}cos(\omega t) + \frac{V_{b1b2}}{L_{eq}}cos(\omega t - 120) + \\ &\frac{V_{c1c2}}{L_{eq}}cos(\omega t + 120)) - \frac{2}{3}(\frac{R_{eq}}{L_{eq}}i_{fa}cos(\omega t) + \\ &\frac{R_{eq}}{L_{eq}}i_{fb}cos(\omega t - 120) + \frac{R_{eq}}{L_{eq}}i_{fc}cos(\omega t + 120)) + \omega i_{fq} \\ \frac{di_{fq}}{dt} &= -\frac{2}{3}(\frac{V_{a1a2}}{L_{eq}}sin(\omega t) + \frac{V_{b1b2}}{L_{eq}}sin(\omega t - 120) + \\ &\frac{V_{c1c2}}{L_{eq}}sin(\omega t + 120)) + \frac{2}{3}(\frac{R_{eq}}{L_{eq}}i_{fa}sin(\omega t) + \\ &\frac{R_{eq}}{L_{eq}}i_{fb}sin(\omega t - 120) + \frac{R_{eq}}{L_{eq}}i_{fc}sin(\omega t + 120)) - \omega i_{fd}\end{aligned} \tag{4.32}$$

Using equation 4.22,4.23, the equation 4.32 can be simplified to

$$\begin{aligned}\frac{di_{fd}}{dt} &= \frac{V_{fd}}{L_{eq}} - \frac{R_{eq}}{L_{eq}}i_{fd} + \omega i_{fq} \\ \frac{di_{fq}}{dt} &= \frac{V_{fq}}{L_{eq}} - \frac{R_{eq}}{L_{eq}}i_{fq} - \omega i_{fd}\end{aligned} \tag{4.33}$$

$$V_{fd} = R_{eq}i_{fd} + L_{eq}\frac{di_{fd}}{dt} - \omega L_{eq}i_{fq} \tag{4.34}$$

$$V_{fq} = R_{eq}i_{fq} + L_{eq}\frac{di_{fq}}{dt} + \omega L_{eq}i_{fd} \tag{4.35}$$

Using (4.33), the state space equations can be written in the form of $\dot{x} = Ax + Bu$ and $y = Cx + Du$ as:

$$\begin{bmatrix}\frac{di_{fd}}{dt} \\ \frac{di_{fq}}{dt}\end{bmatrix} = \begin{bmatrix}\frac{-R_{eq}}{L_{eq}} & \omega \\ -\omega & \frac{-R_{eq}}{L_{eq}}\end{bmatrix}\begin{bmatrix}i_{fd} \\ i_{fq}\end{bmatrix} + \begin{bmatrix}\frac{V_{dc}}{L_{eq}} & 0 \\ 0 & \frac{V_{dc}}{L_{eq}}\end{bmatrix}\begin{bmatrix}m_d \\ m_q\end{bmatrix} \tag{4.36}$$

$$\begin{bmatrix}i_{ofd} \\ i_{ofq}\end{bmatrix} = \begin{bmatrix}1 & 0 \\ 0 & 1\end{bmatrix}\begin{bmatrix}i_{fd} \\ i_{fq}\end{bmatrix} \tag{4.37}$$

From the state space equation, the transfer function can be derived in the form of $Y(s) = (C(SI - A)^{-1}B + D) * U(s)$ as:

$$\begin{bmatrix}i_{ofd} \\ i_{ofq}\end{bmatrix} = \begin{bmatrix}1 & 0 \\ 0 & 1\end{bmatrix}\begin{bmatrix}s + \frac{R_{eq}}{L_{eq}} & -\omega \\ \omega & s + \frac{R_{eq}}{L_{eq}}\end{bmatrix}^{-1}\begin{bmatrix}\frac{V_{dc}}{L_{eq}} & 0 \\ 0 & \frac{V_{dc}}{L_{eq}}\end{bmatrix}\begin{bmatrix}m_d \\ m_q\end{bmatrix} \tag{4.38}$$

$$\begin{bmatrix}i_{ofd} \\ i_{ofq}\end{bmatrix} = \begin{bmatrix}\frac{(s+\frac{R_{eq}}{L_{eq}})(\frac{V_{dc}}{L_{eq}})}{(s+\frac{R_{eq}}{L_{eq}})^2+\omega^2} & \frac{\omega(\frac{V_{dc}}{L_{eq}})}{(s+\frac{R_{eq}}{L_{eq}})^2+\omega^2} \\ \frac{-\omega(\frac{V_{dc}}{L_{eq}})}{(s+\frac{R_{eq}}{L_{eq}})^2+\omega^2} & \frac{(s+\frac{R_{eq}}{L_{eq}})(\frac{V_{dc}}{L_{eq}})}{(s+\frac{R_{eq}}{L_{eq}})^2+\omega^2}\end{bmatrix}\begin{bmatrix}m_d \\ m_q\end{bmatrix} \tag{4.39}$$

$$\begin{bmatrix}i_{ofd} \\ i_{ofq}\end{bmatrix} = \begin{bmatrix}G_{11} & G_{12} \\ G_{21} & G_{22}\end{bmatrix}\begin{bmatrix}m_d \\ m_q\end{bmatrix} \tag{4.40}$$

The derived G_{11} and G_{22} represents the $d-$ loop and $q-$ loop plant transfer functions as shown in Fig. 4.9. The plant transfer function is described as follows:

$$G_{11} = G_{22} = \frac{(sL_{eq} + R_{eq})(V_{dc})}{s^2 L_{eq}^2 + 2L_{eq}R_{eq}s + R_{eq}^2 + \underbrace{(\omega L_{eq})^2}_{\approx 0}} \tag{4.41}$$

By neglecting $(\omega L_{eq})^2$, the plant transfer function can be simplified to:

$$G_{plant} = \frac{1}{(sL_{eq} + R_{eq})} \tag{4.42}$$

Chapter 5

Conclusion

5.1 Summary

Significant contributions of the presented research work are as follows:

1. Acknowledging the critical importance of designing appropriate passive filters for solar interface inverters, particularly in shaping grid power quality, this study presents a novel passive filter design approach. The methodology revolves around computing instantaneous load time constants at various power processing stages, considering both load and source dynamics. The active filter developed through this method is tasked with a dual role: mitigating harmonics from nonlinear loads and injecting active power into the grid, even under weak grid conditions. Moreover, this innovative approach explores the significant correlation between passive filter bandwidth and its ability to attenuate switching frequencies while accommodating permissible load-induced harmonics. Additionally, the study elaborates on the process of modeling and fine-tuning the current controller, which involves monitoring the load network's time constant across different source and load power scenarios to determine the bandwidth necessary for effectively managing load-induced harmonics in compliance with IEEE-519 standards. The SiSAPF system can operate in grid power injection and drawing modes, depending on available solar power and demand for load. In the grid-injected mode, where interactions between grid impedance and network impedance lead to power oscillations at the fundamental frequency, the study proposes establishing appropriate controller gain boundaries by assessing interactive time constants. Subsequently, experimental validation of the solar-interfaced shunt active power filter (SISAPF) with active power injection capability is conducted in both grid power drawing and injection modes, showcasing the effectiveness of the enhanced bandwidth in handling load-induced harmonics and solar power dynamic variations.

2. Acknowledging the limitations of existing literature, this study proposes a solar-interfaced offboard charging station employing a front-end inverter topology. This system adeptly manages dynamic fluctuations in both source and load power. The front-end converter acts as a seamless regulator of solar power in response to load demands, simultaneously addressing harmonics to synthesize grid-drawn/injected current at unity power factor by positioning the solar interface on the AC side. The converter introduces a novel dedicated rolling gain adjustment control mechanism,

operating in four distinct modes with diverse functionalities (as elaborated in Table-5.1). This mechanism comprises two key steps:

Table 5.1: PIFI with available modes of operation

P_{pv}=solar power,P_L=Load power,P_R=Rated power

Modes	Source Power	Load Power	Grid power	Harmonic support	Power factor
Mode-1	$P_{pv}=P_R$	$P_L<P_R$	injection	yes	unity
Mode-2	$P_{pv}=P_R$	$P_L=P_R$	-	yes	unity
Mode-3	$P_{pv}<P_R$	$P_L<P_{pv}$	injection	yes	unity
Mode-4	$P_{pv}<P_R$	$P_L=P_R$	drawing	yes	unity

- First, load and source dynamics are determined through equivalent impedance parameter estimation at instantaneous and solar power.
- Second, controller gains can be adjusted based on estimated dynamics to produce load harmonics using available PV power. The load and solar angular frequencies are estimated utilizing voltage and current active and reactive components in a synchronous reference frame.

The closed-loop controller accurately tracks the load angular frequency derived from estimated load network inductance and per-phase resistance. Dynamic variations in the converter operating angular frequencies are modeled based on changes in solar and load power, enabling the adaptation of controller gains. With these dynamically updated gains, the front-end inverter effectively generates harmonics in line with load demands across a broad spectrum of source and load power variations. As a result, the proposed converter functions as a modified front-end inverter with power factor correction (PFC) for a charging station equipped with active power injection capability.

3. With the aim of further improving harmonic compensation capability through suitable filter sizing and power distribution in terms of voltage, a novel series inverter configuration is proposed for active filtering and real power injection in solar applications. This configuration entails the filter experiencing twice the switching frequency compared to other topologies. This virtual doubling of the switching frequency creates a widened band gap between switching harmonics and load-induced harmonics, resulting in reduced attenuation for load-induced harmonics. Moreover, the series inverter's topological advantage, which processes double the current at half the voltage, reduces filter requirements compared to parallel inverter topologies. Considering all these factors and the load network time constant, a new filter design methodology is outlined. This methodology is demonstrated to yield the optimal filter size for suppressing switching harmonics and effectively managing load-induced harmonics, surpassing available methods in the literature. The optimal filter size also ensures an enhanced closed-loop control bandwidth, thereby enhancing grid

power quality according to IEEE-519 standards compared to conventional parallel inverter topologies. The effectiveness of the proposed series inverter with superior harmonic compensation capability across various active solar power variations is experimentally verified to validate the real-time adaptability of the proposed configuration.

5.2 Scope of Future Research

1. In-series inverter topology Energy management between two sources while active power injection and harmonic compensation can be implemented.
2. An adaptive current Controller can be implemented for weak grid conditions for solar inverters using the derived plant transfer model.
3. Different PWM techniques can be analyzed for the proposed series configuration to reduce the magnitude of leakage current to achieve the maximum DC gain with an isolated DC bus.
4. Different MPPT techniques can also be realized to extract the maximum power in case of partial shading conditions for the novel proposed configuration.

References

[1] Malabika Basu, S.P. Das, and G.K. Dubey. Parallel converter scheme for high-power active power filters. *Electric Power Applications, IEE Proceedings* -, 151:460 – 466, 08 2004. doi: 10.1049/ip-epa:20040211.

[2] M. Sedighy, S.B. Dewan, and F.P. Dawson. A robust digital current control method for active power filters. *IEEE Transactions on Industry Applications*, 36 (4):1158–1164, 2000.

[3] Ieee standard dictionary of electrical and electronics terms. *IEEE Transactions on Power Apparatus and Systems*, PAS-99(6):37a–37a, 1980.

[4] H. Awad and M.H.J. Bollen. Power electronics for power quality improvements. In *2003 IEEE International Symposium on Industrial Electronics (Cat. No.03TH8692)*, volume 2, pages 1129–1136 vol. 2, 2003.

[5] Tushar Bhavsar and G. Narayanan. Harmonic analysis of advanced bus-clamping pwm techniques. *IEEE Transactions on Power Electronics*, 24(10):2347–2352, 2009. doi: 10.1109/TPEL.2009.2013492.

[6] E.W. Gunther and H. Mebta. A survey of distribution system power quality-preliminary results. *IEEE Transactions on Power Delivery*, 10(1):322–329, 1995. doi: 10.1109/61.368382.

[7] A. von Jouanne and B. Banerjee. Assessment of voltage unbalance. *IEEE Transactions on Power Delivery*, 16(4):782–790, 2001.

[8] Jos Arrillaga Neville R. Watson. *Power System Harmonics*. Jhon Wiley and Sons, 2nd edition, 2016.

[9] K. R. Padiyar. *FACTS Controllers in Power Transmission Distribution*. Anshan, new age edition, 2009.

[10] V.E. Wagner, J.C. Balda, D.C. Griffith, A. McEachern, T.M. Barnes, D.P. Hartmann, D.J. Phileggi, A.E. Emannuel, W.F. Horton, W.E. Reid, R.J. Ferraro, and W.T. Jewell. Effects of harmonics on equipment. *IEEE Transactions on Power Delivery*, 8(2):672–680, 1993. doi: 10.1109/61.216874.

[11] G. Manchur and C.C. Erven. Development of a model for predicting flicker from electric arc furnaces. *IEEE Transactions on Power Delivery*, 7(1):416–426, 1992.

[12] J.S. Subjak and J.S. McQuilkin. Harmonics-causes, effects, measurements, and analysis: an update. *IEEE Transactions on Industry Applications*, 26(6):1034–1042, 1990.

[13] M. D. Cox and A. Mirbod. A new static var compensator for an arc furnace. *IEEE Transactions on Power Systems*, 1(3):110–119, 1986.

[14] G. Blajszczak. Direct method for voltage distortion compensation in power networks by series converter filter. *IEE Proceedings - Electric Power Applications*, 142:308 – 312, 1995.

[15] Gu Jianjun, Xu Dianguo, Liu Hankui, and Gong Maozhong. Unified power quality conditioner (upqc): the principle, control and application. In *Proceedings of the Power Conversion Conference-Osaka 2002 (Cat. No.02TH8579)*, volume 1, pages 80–85 vol.1, 2002.

[16] Ieee recommended practice for electric power distribution for industrial plants. *IEEE Std 141-1993*, pages 1–768, 1994. doi: 10.1109/IEEESTD.1994.121642.

[17] Ieee recommended practice for grounding of industrial and commercial power systems. *IEEE Std 142-2007 (Revision of IEEE Std 142-1991)*, pages 1–225, 2007. doi: 10.1109/IEEESTD.2007.4396963.

[18] Ieee recommended practice and requirements for harmonic control in electric power systems. *IEEE Std 519-2014 (Revision of IEEE Std 519-1992)*, pages 1–29, 2014. doi: 10.1109/IEEESTD.2014.6826459.

[19] Electromagnetic compatibility (emc) - part 3-2: Limits - limits for harmonic current emissions (equipment input current $\leq$ 16 a per phase). *IEC 61000-3-2:2018*, page 73, 2018.

[20] Ieee guide for identifying and improving voltage quality in power systems. *IEEE Std 1250-2018 (Revision of IEEE Std 1250-2011)*, pages 1–63, 2018. doi: 10.1109/IEEESTD.2018.8532376.

[21] Ieee recommended practice for monitoring electric power quality. *IEEE Std 1159-2019 (Revision of IEEE Std 1159-2009)*, pages 1–98, 2019. doi: 10.1109/IEEESTD.2019.8796486.

[22] Ieee recommended practice for voltage sag and short interruption ride-through testing for end-use electrical equipment rated less than 1000 v. *IEEE Std 1668-2017 (Revision of IEEE Std 1668-2014)*, pages 1–85, 2017. doi: 10.1109/IEEESTD.2017.8120227.

[23] Ieee recommended practice for the design of reliable industrial and commercial power systems. *IEEE Std 493-2007 (Revision of IEEE Std 493-1997)*, pages 1–383, 2007. doi: 10.1109/IEEESTD.2007.380668.

[24] Ieee guide for voltage sag indices. *IEEE Std 1564-2014*, page 1–59, 2014.

[25] Ieee standard for interconnection and interoperability of distributed energy resources with associated electric power systems interfaces. *IEEE Std 1547-2018 (Revision of IEEE Std 1547-2003)*, pages 1–138, 2018. doi: 10.1109/IEEESTD.2018.8332112.

[26] Ieee draft recommended practice for the analysis of fluctuating installations on power systems. *IEEE P1453/D7, March 2015*, pages 1–72, 2015.

[27] Y. Y. Chen, G. W. Chang, and S. C. Lin. A digital implementation of iec 61000-4-15 flickermeter. In *2015 IEEE Power Energy Society General Meeting*, pages 1–5, 2015. doi: 10.1109/PESGM.2015.7286254.

[28] B. Singh, K. Al-Haddad, and A. Chandra. A review of active filters for power quality improvement. *IEEE Transactions on Industrial Electronics*, 46(5):960–971, 1999. doi: 10.1109/41.793345.

[29] Damian A. Gonzalez and John C. McCall. Design of filters to reduce harmonic distortion in industrial power systems. *IEEE Transactions on Industry Applications*, IA-23(3):504–511, 1987.

[30] Mark McGranaghan and Bill Roettger. Economic evaluation of power quality. *IEEE Power Engineering Review*, 22(2):8–12, 2002.

[31] J.C. Das. Passive filters-potentialities and limitations. In *Conference Record of the 2003 Annual Pulp and Paper Industry Technical Conference, 2003.*, pages 187–197, 2003.

[32] V. Soares, P. Verdelho, and G.D. Marques. An instantaneous active and reactive current component method for active filters. *IEEE Transactions on Power Electronics*, 15(4):660–669, 2000.

[33] H. Akagi and H. Fujita. A new power line conditioner for harmonic compensation in power systems. *IEEE Transactions on Power Delivery*, 10(3):1570–1575, 1995. doi: 10.1109/61.400941.

[34] H. Akagi, A. Nabae, and S. Atoh. Control strategy of active power filters using multiple voltage-source pwm converters. In *1985 Annual Meeting Industry Applications Society*, pages 460–466, 1985.

[35] Hirofumi Akagi, Yoshihira Kanazawa, and Akira Nabae. Instantaneous reactive power compensators comprising switching devices without energy storage components. *IEEE Transactions on Industry Applications*, IA-20(3):625–630, 1984. doi: 10.1109/TIA.1984.4504460.

[36] Sergio Alejandro Gonzalez, Rogelio Garcia-Retegui, and Mario Benedetti. Harmonic computation technique suitable for active power filters. *IEEE Transactions on Industrial Electronics*, 54(5):2791–2796, 2007.

[37] W.M. Grady, M.J. Samotyj, and A.H. Noyola. Survey of active power line conditioning methodologies. *IEEE Transactions on Power Delivery*, 5(3):1536–1542, 1990.

[38] Brij N. Singh, Bhim Singh, Ambrish Chandra, Parviz Rastgoufard, and Kamal Al-Haddad. An improved control algorithm for active filters. *IEEE Transactions on Power Delivery*, 22(2):1009–1020, 2007. doi: 10.1109/TPWRD.2006.886790.

[39] E.H. Watanabe H.Akagi and M.Aredes. *Instantaneous Power Theory and Applications to Power Conditioning*. New York: Wiley, 2ed edition, 2017.

[40] B. Singh, K. Al-Haddad, and A. Chandra. A new control approach to three-phase active filter for harmonics and reactive power compensation. *IEEE Transactions on Power Systems*, 13(1):133–138, 1998. doi: 10.1109/59.651624.

[41] Bhim Singh, P. Jayaprakash, T. R. Somayajulu, and D. P. Kothari. Reduced rating vsc with a zig-zag transformer for current compensation in a three-phase four-wire distribution system. *IEEE Transactions on Power Delivery*, 24(1):249–259, 2009.

[42] *United Nations Framework Convention on Climate Change*. UNFCCC, 2016. Paris agreement.

[43] Mohammed Qasim, Parag Kanjiya, and Vinod Khadkikar. Artificial-neural-network-based phase-locking scheme for active power filters. *IEEE Transactions on Industrial Electronics*, 61(8):3857–3866, 2014. doi: 10.1109/TIE.2013.2284132.

[44] Asmae Azzam Jai and Mohammed Ouassaid. Machine learning-based adaline neural pq strategy for a photovoltaic integrated shunt active power filter. *IEEE Access*, 11: 56593–56618, 2023. doi: 10.1109/ACCESS.2023.3281488.

[45] Doğan Çelik, Hafiz Ahmed, and Mehmet Emin Meral. Kalman filter-based super-twisting sliding mode control of shunt active power filter for electric vehicle charging station applications. *IEEE Transactions on Power Delivery*, 38(2): 1097–1107, 2023. doi: 10.1109/TPWRD.2022.3206267.

[46] Sawsan S. Sayed and Ahmed M. Massoud. Review on state-of-the-art unidirectional non-isolated power factor correction converters for short-/long-distance electric vehicles. *IEEE Access*, 10:11308–11340, 2022. doi: 10.1109/ACCESS.2022.3146410.

[47] Baibhav Kumar Gupta, K. Ramachandra Sekhar, and Amol Ishwarrao Gedam. Solar interfaced series inverter with provision of common dc bus grounding. *IEEE Transactions on Industrial Electronics*, 69(4):3656–3666, 2022. doi: 10.1109/TIE.2021.3073303.

[48] Rahul Kumar Agarwal, Ikhlaq Hussain, and Bhim Singh. Implementation of llmf control algorithm for three-phase grid-tied spv-dstatcom system. *IEEE Transactions on Industrial Electronics*, 64(9):7414–7424, 2017. doi: 10.1109/TIE.2016.2630659.

[49] Bhim Singh, Maulik Kandpal, and Ikhlaq Hussain. Control of grid tied smart pv-dstatcom system using an adaptive technique. *IEEE Transactions on Smart Grid*, 9(5):3986–3993, 2018. doi: 10.1109/TSG.2016.2645600.

[50] Kamran Jalili and Steffen Bernet. Design of *lcl* filters of active-front-end two-level voltage-source converters. *IEEE Transactions on Industrial Electronics*, 56(5): 1674–1689, 2009. doi: 10.1109/TIE.2008.2011251.

[51] M. Liserre, F. Blaabjerg, and S. Hansen. Design and control of an lcl-filter-based three-phase active rectifier. *IEEE Transactions on Industry Applications*, 41(5): 1281–1291, 2005. doi: 10.1109/TIA.2005.853373.

[52] Oleg Vodyakho and Chris C. Mi. Three-level inverter-based shunt active power filter in three-phase three-wire and four-wire systems. *IEEE Transactions on Power Electronics*, 24(5):1350–1363, 2009. doi: 10.1109/TPEL.2009.2016663.

[53] Yap Hoon, Mohd Amran Mohd Radzi, Mohd Khair Hassan, and Nashiren Farzilah Mailah. Operation of three-level inverter-based shunt active power filter under nonideal grid voltage conditions with dual fundamental component extraction. *IEEE Transactions on Power Electronics*, 33(9):7558–7570, 2018. doi: 10.1109/TPEL.2017.2766268.

[54] H. Akagi and A. Nabae. The p-q theory in three-phase systems under non-sinusoidal conditions. *European Transactions on Electrical Power*, 3(1):27–31, 1993. doi: https://doi.org/10.1002/etep.4450030106. URL https://onlinelibrary.wiley.com/doi/abs/10.1002/etep.4450030106.

[55] Gregory Arthur de Almeida Carlos, Cursino Brandão Jacobina, Euzeli Cipriano dos Santos, Edgard Luiz Lopes Fabrício, and Nady Rocha. Shunt active power filter with open-end winding transformer and series-connected converters. *IEEE Transactions on Industry Applications*, 51(4):3273–3283, 2015. doi: 10.1109/TIA.2015.2394318.

[56] Alireza Fereidouni, Mohammad A. S. Masoum, and Keyue M. Smedley. Supervisory nearly constant frequency hysteresis current control for active power filter applications in stationary reference frame. *IEEE Power and Energy Technology Systems Journal*, 3(1):1–12, 2016. doi: 10.1109/JPETS.2015.2501423.

[57] Quoc-Nam Trinh and Hong-Hee Lee. An advanced current control strategy for three-phase shunt active power filters. *IEEE Transactions on Industrial Electronics*, 60(12):5400–5410, 2013. doi: 10.1109/TIE.2012.2229677.

[58] Salem Rahmani, Nassar Mendalek, and Kamal Al-Haddad. Experimental design of a nonlinear control technique for three-phase shunt active power filter. *IEEE Transactions on Industrial Electronics*, 57(10):3364–3375, 2010. doi: 10.1109/TIE.2009.2038945.

[59] Xiaohua Nie and Jijun Liu. Current reference control for shunt active power filters under unbalanced and distorted supply voltage conditions. *IEEE Access*, 7:177048–177055, 2019. doi: 10.1109/ACCESS.2019.2957946.

[60] Alok Kumar Mishra, Soumya Ranjan Das, Prakash K. Ray, Ranjan Kumar Mallick, Asit Mohanty, and Dillip K. Mishra. Pso-gwo optimized fractional order pid based hybrid shunt active power filter for power quality improvements. *IEEE Access*, 8: 74497–74512, 2020. doi: 10.1109/ACCESS.2020.2988611.

[61] Hao Chen, Huawu Liu, Yan Xing, and Haibing Hu. Enhanced dft-based controller for selective harmonic compensation in active power filters. *IEEE Transactions on Power Electronics*, 34(8):8017–8030, 2019. doi: 10.1109/TPEL.2018.2877848.

[62] P. Mahesh Reddy, K. Manjunath, K. Ramachandra Sekhar, and Baibhav Kumar Gupta. Nonlinear load time-constant based filter inductance design for pv-driven grid-connected saf/pfc in ev charging infrastructure. In *IECON 2023- 49th Annual Conference of the IEEE Industrial Electronics Society*, pages 1–6, 2023. doi: 10.1109/IECON51785.2023.10312368.

[63] Rida Musa, Ab. Hamadi, A. Ndtoungou, S. Rahmani, and K. Al-Haddad. Optimal design of inductor and dc bus voltage for shunt active filter. In *IECON 2017 - 43rd Annual Conference of the IEEE Industrial Electronics Society*, pages 6482–6487, 2017. doi: 10.1109/IECON.2017.8217129.

[64] A.M. Al-Zamil and D.A. Torrey. A passive series, active shunt filter for high power applications. *IEEE Transactions on Power Electronics*, 16(1):101–109, 2001. doi: 10.1109/63.903994.

[65] M. Liserre, R. Teodorescu, and F. Blaabjerg. Multiple harmonics control for three-phase grid converter systems with the use of pi-res current controller in a rotating frame. *IEEE Transactions on Power Electronics*, 21(3):836–841, 2006. doi: 10.1109/TPEL.2006.875566.

[66] R.I. Bojoi, G. Griva, V. Bostan, M. Guerriero, F. Farina, and F. Profumo. Current control strategy for power conditioners using sinusoidal signal integrators in synchronous reference frame. *IEEE Transactions on Power Electronics*, 20(6): 1402–1412, 2005. doi: 10.1109/TPEL.2005.857558.

[67] Diarmaid John Hogan, Francisco J. Gonzalez-Espin, John G. Hayes, Gordon Lightbody, and Raymond Foley. An adaptive digital-control scheme for improved active power filtering under distorted grid conditions. *IEEE Transactions on Industrial Electronics*, 65(2):988–999, 2018. doi: 10.1109/TIE.2017.2726992.

[68] Mallikarjuna Golla, S. Thangavel, Sishaj Pulikottil Simon, and Narayana Prasad Padhy. A novel control scheme using uapf in an integrated pv grid-tied system. *IEEE*

Transactions on Power Delivery, 38(1):133–145, 2023. doi: 10.1109/TPWRD.2022.3180681.

[69] Mallikarjuna Golla, S. Thangavel, Sishaj Pulikottil Simon, and Narayana Prasad Padhy. An enhancement of power quality with efficient active power transfer capability in a pv–bss-fed uapf for microgrid realization. *IEEE Systems Journal*, 17(1):1614–1625, 2023. doi: 10.1109/JSYST.2022.3179182.

[70] Ramon Guzman, Luis Garcia de Vicuña, Javier Morales, Miguel Castilla, and Jaume Miret. Model-based control for a three-phase shunt active power filter. *IEEE Transactions on Industrial Electronics*, 63(7):3998–4007, 2016. doi: 10.1109/TIE.2016.2540580.

[71] Tengteng Wang and Juntao Fei. Adaptive neural control of active power filter using fuzzy sliding mode controller. *IEEE Access*, 4:6816–6822, 2016. doi: 10.1109/ACCESS.2016.2591978.

[72] Shixi Hou, Juntao Fei, Yundi Chu, and Chen Chen. Experimental investigation of adaptive fuzzy global sliding mode control of single-phase shunt active power filters. *IEEE Access*, 7:64442–64449, 2019. doi: 10.1109/ACCESS.2019.2917020.

[73] Javier Morales, Luis Garcia de Vicuña, Ramon Guzman, Miguel Castilla, and Jaume Miret. Modeling and sliding mode control for three-phase active power filters using the vector operation technique. *IEEE Transactions on Industrial Electronics*, 65(9):6828–6838, 2018. doi: 10.1109/TIE.2018.2795528.

[74] Weidong Jiang, Xingxing Ding, Youyuan Ni, Jinping Wang, Lei Wang, and Weicheng Ma. An improved deadbeat control for a three-phase three-line active power filter with current-tracking error compensation. *IEEE Transactions on Power Electronics*, 33(3):2061–2072, 2018. doi: 10.1109/TPEL.2017.2693325.

[75] Yang Han, Lin Xu, Muhammad Mansoor Khan, Chen Chen, Gang Yao, and Li-Dan Zhou. Robust deadbeat control scheme for a hybrid apf with resetting filter and adaline-based harmonic estimation algorithm. *IEEE Transactions on Industrial Electronics*, 58(9):3893–3904, 2011. doi: 10.1109/TIE.2010.2093475.

[76] Mohammad Pichan, Mohsen Seyyedhosseini, and Hossein Hafezi. A new deadbeat-based direct power control of shunt active power filter with digital implementation delay compensation. *IEEE Access*, 10:72866–72878, 2022. doi: 10.1109/ACCESS.2022.3188685.

[77] Lili Zhou, Zhen Zhou, Jia Qi, and Wei Han. Hybrid prediction-based deadbeat control for a high-performance shunt active power filter. *IEEE Access*, 11:11118–11131, 2023. doi: 10.1109/ACCESS.2023.3241300.

[78] Rakhee Panigrahi and Bidyadhar Subudhi. Performance enhancement of shunt active power filter using a kalman filter-based H_∞ control strategy. *IEEE*

Transactions on Power Electronics, 32(4):2622–2630, 2017. doi: 10.1109/TPEL.2016.2572142.

[79] Yuguo Li, Hao Yi, Fang Zhuo, and Xin Jiang. Analysis and stabilization of apf systems considering dynamic of nonlinear loads. *IEEE Transactions on Power Electronics*, 39(1):409–423, 2024.

[80] Lei Yang, Lihang Zhao, Xinqi Chen, Zhebo Zhang, Heng Nian, Jianyong Zhao, Rongfeng Deng, and Liang Yan. Robust active damping control for lcl-type shunt active power filters. *IEEE Access*, 10:39456–39470, 2022. doi: 10.1109/ACCESS.2022.3166598.

[81] Ning-Yi Dai and Man-Chung Wong. Design considerations of coupling inductance for active power filters. In *2011 6th IEEE Conference on Industrial Electronics and Applications*, pages 1370–1375, 2011. doi: 10.1109/ICIEA.2011.5975801.

[82] Weimin Wu, Yuan Liu, Yuanbin He, Henry Shu-Hung Chung, Marco Liserre, and Frede Blaabjerg. Damping methods for resonances caused by lcl-filter-based current-controlled grid-tied power inverters: An overview. *IEEE Transactions on Industrial Electronics*, 64(9):7402–7413, 2017. doi: 10.1109/TIE.2017.2714143.

[83] Narsa Reddy Tummuru, Mahesh K. Mishra, and S. Srinivas. An improved current controller for grid connected voltage source converter in microgrid applications. *IEEE Transactions on Sustainable Energy*, 6(2):595–605, 2015.

[84] Swagat Kumar Panda and Bidyadhar Subudhi. A review on robust and adaptive control schemes for microgrid. *Journal of Modern Power Systems and Clean Energy*, 11(4):1027–1040, 2023.

[85] Mauricio Cespedes and Jian Sun. Adaptive control of grid-connected inverters based on online grid impedance measurements. *IEEE Transactions on Sustainable Energy*, 5(2):516–523, 2014.

[86] Baibhav Kumar Gupta and K. Ramachandra Sekhar. A current controller gain characterization of weak grid coupled solar inverter through impedance interaction modeling. *IEEE Transactions on Industrial Electronics*, 70(3):2520–2530, 2023. doi: 10.1109/TIE.2022.3170633.

[87] Jian Sun. Impedance-based stability criterion for grid-connected inverters. *IEEE Transactions on Power Electronics*, 26(11):3075–3078, 2011. doi: 10.1109/TPEL.2011.2136439.

[88] Jingyang Fang, Xiaoqiang Li, Hongchang Li, and Yi Tang. Stability improvement for three-phase grid-connected converters through impedance reshaping in quadrature-axis. *IEEE Transactions on Power Electronics*, 33(10):8365–8375, 2018. doi: 10.1109/TPEL.2017.2777972.

[89] Bo Wen, Dong Dong, Dushan Boroyevich, Rolando Burgos, Paolo Mattavelli, and Zhiyu Shen. Impedance-based analysis of grid-synchronization stability for three-phase paralleled converters. *IEEE Transactions on Power Electronics*, 31(1): 26–38, 2016. doi: 10.1109/TPEL.2015.2419712.

[90] Xueguang Zhang, Danni Xia, Zhichao Fu, Gaolin Wang, and Dianguo Xu. An improved feedforward control method considering pll dynamics to improve weak grid stability of grid-connected inverters. *IEEE Transactions on Industry Applications*, 54(5):5143–5151, 2018. doi: 10.1109/TIA.2018.2811718.

[91] Dongsheng Yang, Xiongfei Wang, Fangcheng Liu, Kai Xin, Yunfeng Liu, and Frede Blaabjerg. Adaptive reactive power control of pv power plants for improved power transfer capability under ultra-weak grid conditions. *IEEE Transactions on Smart Grid*, 10(2):1269–1279, 2019. doi: 10.1109/TSG.2017.2762332.

[92] Kamil Antoniewicz, Marek Jasinski, Marian P. Kazmierkowski, and Mariusz Malinowski. Model predictive control for three-level four-leg flying capacitor converter operating as shunt active power filter. *IEEE Transactions on Industrial Electronics*, 63(8):5255–5262, 2016.

[93] Gitanjali Pandove and Mukhtiar Singh. Robust repetitive control design for a three-phase four-wire shunt active power filter. *IEEE Transactions on Industrial Informatics*, 15(5):2810–2818, 2019.

[94] Mohamad Alaa Eddin Alali, Yuri B. Shtessel, and Jean-Pierre Barbot. Grid-connected shunt active lcl control via continuous sliding modes. *IEEE/ASME Transactions on Mechatronics*, 24(2):729–740, 2019.

[95] Osman Kukrer, Hasan Komurcugil, Ramon Guzman, and Luis Garcia de Vicuna. A new control strategy for three-phase shunt active power filters based on fir prediction. *IEEE Transactions on Industrial Electronics*, 68(9):7702–7713, 2021.

[96] Gregory A. de Almeida Carlos, Cursino B. Jacobina, and Euzeli C. dos Santos. Alternative breed of three-phase four-wire shunt compensators based on a cascaded transformer with single dc-link. In *2017 IEEE Applied Power Electronics Conference and Exposition (APEC)*, pages 3321–3328, 2017.

[97] Bhukya Nageswar Rao, Yellasiri Suresh, Anup Kumar Panda, Banavath Shiva Naik, and Venkataramanaiah Jammala. Development of cascaded multilevel inverter based active power filter with reduced transformers. *CPSS Transactions on Power Electronics and Applications*, 5(2):147–157, 2020.

[98] Muneer V and Avik Bhattacharya. Peak power demand management by using smc-controlled three-level chb-based three-wire and four-wire sapf. *IEEE Transactions on Industrial Informatics*, 17(8):5270–5281, 2021.

[99] L.A. Moran, L. Fernandez, J.W. Dixon, and R. Wallace. A simple and low-cost control strategy for active power filters connected in cascade. *IEEE Transactions on Industrial Electronics*, 44(5):621–629, 1997.

[100] Lucian Asiminoaei, Eddy Aeloiza, Prasad N. Enjeti, and Frede Blaabjerg. Shunt active-power-filter topology based on parallel interleaved inverters. *IEEE Transactions on Industrial Electronics*, 55(3):1175–1189, 2008.

[101] Tushar G. Vaidya and Kishore Chatterjee. A decentralized control scheme for multimodular shunt active harmonic filters. *IEEE Transactions on Industrial Electronics*, 69(2):1081–1090, 2022.

[102] Han Li, Weimin Wu, Min Huang, Henry Shu-hung Chung, Marco Liserre, and Frede Blaabjerg. Design of pwm-smc controller using linearized model for grid-connected inverter with lcl filter. *IEEE Transactions on Power Electronics*, 35(12):12773–12786, 2020.

[103] Hua Chen and Xiangyang Xing. Circulating current analysis and suppression for module grid-connected inverters under unbalanced conditions. *IEEE Access*, 6: 69120–69129, 2018.

[104] Aitor Laka, Jon Andoni Barrena, Javier Chivite-Zabalza, Miguel Angel Rodríguez Vidal, and Gorka Calvo. Novel zero-sequence blocking transformer (zsbt) using three single-phase transformers. *IEEE Transactions on Energy Conversion*, 28(1): 234–242, 2013.

[105] Toni Itkonen, Julius Luukko, Arto Sankala, Tommi Laakkonen, and Riku PÖllÄnen. Modeling and analysis of the dead-time effects in parallel pwm two-level three-phase voltage-source inverters. *IEEE Transactions on Power Electronics*, 24(11): 2446–2455, 2009.

[106] Jeyraj Selvaraj and Nasrudin A. Rahim. Multilevel inverter for grid-connected pv system employing digital pi controller. *IEEE Transactions on Industrial Electronics*, 56(1):149–158, 2009.

[107] Shivam Kumar Yadav, Nidhi Mishra, Bhim Singh, Sanjeevikumar Padmanaban, and Frede Blaabjerg. Scott-tied magnetically linked solar multilevel converter in varying environmental conditions. *IEEE Journal of Emerging and Selected Topics in Industrial Electronics*, 3(3):559–571, 2022.

[108] Shivam Kumar Yadav, Nidhi Mishra, and Bhim Singh. Multilevel converter with nearest level control for integrating solar photovoltaic system. *IEEE Transactions on Industry Applications*, 58(4):5117–5126, 2022.

[109] Tianzhi Fang, Xianyun Zhang, Chun Huang, Wei He, Le Shen, and Xinbo Ruan. Control scheme to achieve multiple objectives and superior reliability

for input-series-output-parallel lcl-type grid-connected inverter system. *IEEE Transactions on Industrial Electronics*, 67(1):214–224, 2020.

[110] Alian Chen, Zicheng Zhang, Xiangyang Xing, Ke Li, Chunshui Du, and Chenghui Zhang. Modeling and suppression of circulating currents for multi-paralleled three-level t-type inverters. *IEEE Transactions on Industry Applications*, 55(4): 3978–3988, 2019.

[111] Ramkrishan Maheshwari, Ghanshyamsinh Gohil, Lorand Bede, and Stig Munk-Nielsen. Analysis and modelling of circulating current in two parallel-connected inverters. *IET Power Electronics*, 8(7):1273–1283, 2015.

[112] Baibhav Kumar Gupta, K. Ramachandra Sekhar, and Aashish Kumar. A novel multigain single-stage grid-connected inverter with asynchronous switching for intra-inverter circulating current elimination. *IEEE Transactions on Power Electronics*, 37(12):15641–15653, 2022.

[113] Yong-Jung Kim and Hyosung Kim. Optimal design of lcl filter in grid-connected inverters. *IET Power Electronics*, 12(7):1774–1782, 2019.

[114] Mohammad-Sadegh Karbasforooshan and Mohammad Monfared. Adaptive self-tuned current controller design for an lcl-filtered lc-tuned single-phase shunt hybrid active power filter. *IEEE Transactions on Power Delivery*, 37(4):2747–2756, 2022.

[115] Qian Liu, Li Peng, Yong Kang, Shiying Tang, Deliang Wu, and Yu Qi. A novel design and optimization method of an *lcl* filter for a shunt active power filter. *IEEE Transactions on Industrial Electronics*, 61(8):4000–4010, 2014.

[116] Hannah Ritchie and Pablo Rosado. Energy mix. *Our World in Data*, 2020. https://ourworldindata.org/energy-mix.

[117] Hannah Ritchie, Max Roser, and Pablo Rosado. Renewable energy. *Our World in Data*, 2020. https://ourworldindata.org/renewable-energy.

[118] G.J. Silva, A. Datta, and S.P. Bhattacharyya. New results on the synthesis of pid controllers. *IEEE Transactions on Automatic Control*, 47(2):241–252, 2002. doi: 10.1109/9.983352.

[119] Johann W. Kolar and Thomas Friedli. The essence of three-phase pfc rectifier systems—part i. *IEEE Transactions on Power Electronics*, 28(1):176–198, 2013. doi: 10.1109/TPEL.2012.2197867.